UC Berkeley
UC Berkeley Electronic Theses and Dissertations

Title
Molecular and Materials Investigations of Mn4O4 and Co4O4 Cubanes in Pursuit of Artificial Photosynthesis

Permalink
https://escholarship.org/uc/item/7br302g6

Author
Van Allsburg, Kurt Michael

Publication Date
2016

Peer reviewed|Thesis/dissertation

eScholarship.org Powered by the California Digital Library
University of California

Molecular and Materials Investigations of Mn_4O_4 and Co_4O_4 Cubanes in Pursuit of Artificial Photosynthesis

By

Kurt Michael Van Allsburg

A dissertation submitted in partial satisfaction of the

requirements for the degree of

Doctor of Philosophy

in

Chemistry

in the

Graduate Division

of the

University of California, Berkeley

Committee in charge:

Professor T. Don Tilley, Chair
Professor Kenneth N. Raymond
Professor Matthew B. Francis
Professor Michael F. Crommie

Spring 2016

Abstract

Molecular and Materials Investigations of Mn_4O_4 and Co_4O_4 Cubanes in Pursuit of Artificial Photosynthesis

By

Kurt Michael Van Allsburg

Doctor of Philosophy in Chemistry
University of California, Berkeley
Professor T. Don Tilley, Chair

Chapter 1:

$Mn_4O_4[O_2P(O\textit{t}Bu)_2]_6$ (**1**), an Mn_4O_4 "cubane" complex combining the structural inspiration of the Photosystem II Oxygen-Evolving Complex with thermolytic precursor ligands, was synthesized and fully characterized. Core oxygen atoms within complex **1** are transferred upon reaction with an oxygen-atom acceptor (PEt_3), to give the butterfly complex $Mn_4O_2[O_2P(O\textit{t}Bu)_2]_6(OPEt_3)_2$. The cubane structure is restored by reaction of the latter complex with the O-atom donor PhIO. Complex **1** was investigated as a precursor to inorganic Mn metaphosphate/pyrophosphate materials, which were studied by X-ray absorption spectroscopy to determine the fate of the Mn_4O_4 unit. Under the conditions employed, thermolyses of **1** result in reduction of the manganese to Mn^{II} species. Finally, the related butterfly complex $Mn_4O_2[O_2P(pin)]_6(bpy)_2$ (pin = pinacolate) is described.

Chapter 2:

The three tetranuclear manganese complexes described in the previous chapter, while not effective in producing inorganic Mn_4O_4-containing materials, exhibit magnetic properties highly relevant to understanding the Photosystem II Oxygen-Evolving Complex (PSII OEC). Previous efforts to understand features of the PSII OEC using manganese model complexes are described, including the need for more information on subtle electronic structure-function relationships. Magnetic susceptibility, electronic paramagnetic resonance (EPR) spectra, and simulations thereof are reported for the three complexes and related to the PSII OEC. In particular, subtle geometric differences between the two butterfly complexes and the magnitude of accompanying spectroscopic changes are related to current proposals on the structure and EPR signals of the PSII OEC's S_2 state.

Chapter 3:

In pursuit of improved stability, facile electrochemical characterization, and artificial photosynthesis device integration for Mn_4O_4 and Co_4O_4 cubane complexes with known or postulated water oxidation activity, efforts to immobilize these complexes on conductive substrates are described. The substrates employed include covalently functionalized glassy carbon, transparent conducting oxides, functionalized carbon nanotubes, and functionalized, conductive polymers prepared by electropolymerization. While anchoring of Mn_4O_4 or Co_4O_4 produced modest success under a few conditions, these efforts were largely

unsuccessful. Detailed analysis of the possible causes for decomposition or incomplete anchoring of cubane is provided in hopes that it might guide future studies of covalently anchored molecular complexes on electrodes.

Chapter 4:

A set of coordination polymers or metal-organic frameworks (MOFs) that builds on the lessons of the previous chapters and exploits the advantages of Co_4O_4 cubanes is described. The Co_4O_4 polymers have favorable properties including stability in basic water and high porosity. The presence of intact Co_4O_4 units was confirmed by XAS, EPR, and other methods. The extended structure of the polymers was elucidated by diffuse X-ray scattering with pair distribution function analysis. The polymers are electrocatalysts for water oxidation and exhibit molecular-level tunability, demonstrating a powerful method for design of new catalysts for artificial photosynthesis.

For my grandparents, Paul, Joyce, Earl, and Audrey

Table of Contents

Acknowledgements

My graduate studies benefited immensely from the people I have encountered since starting at Berkeley. I will name some, but this list is surely incomplete.

First, I am grateful to T. Don Tilley for the pleasure of working with an advisor who values curiosity and the open exchange of ideas above all, even after his many years of success. I will cherish my memories of the Tilley Group, especially the inquisitive spirit that Don cultivates. I am also grateful to Rosemary Tilley, whose knowledge and kindness averted many a panic throughout my years in school. Kevin Ahn helped me start my research and provided many useful suggestions. Lastly, my friendship with Andy Nguyen has lended excitement and sanity to our six years in the group, and especially to our three years working closely together. I hope we have inspired lasting interest in cubanes, camping, and Fun.

In the Department of Chemistry at Berkeley, I thank Kathy Durkin and Tony Iavarone, whose interest and advice enlivened the first two years of my degree that I spent working in Latimer Hall. Teaching Chemistry 208: Structure Analysis by Single-Crystal X-ray Diffraction with the inimitable Ken Raymond was tremendously fun. I am indebted to the department's fantastic administrators who seem capable of resolving any institutional hiccup as if by magic, especially Aileen Harris and Lynn Keithlin. I am grateful to Ashleigh Ward, perhaps above all because innumerable opportunities for the most exquisite of jokes about our often-absurd modern lives would have been wasted had we not met. Jordan Axelson has been a thoughtful, steadfast friend and was my near-constant companion during the heady early years of graduate school.

In the Joint Center for Artificial Photosynthesis (JCAP) at Lawrence Berkeley Lab, I had the pleasure of working with an excellent group of inorganic chemists, led by Don and Cliff Kubiak and including Michael Nippe, David Zee, Wenjun Liu, and David Garfield, who pursued exciting science despite not-infrequent opposition. I am especially grateful to Chris Letko, whose inspiring work ethic, generosity, insight, and attitude made him a great friend and advisor. I am also thankful to our excellent administrative staff in JCAP, including Theresa Short, Erica Hall, Kristin Estis, and Kellie Constantine for their diligence.

I will not try to name each of the friends with whom I have spent the last six years, except to say: they are unforgettable; they have changed my views of the world and what is possible; their kindness, cleverness, and grace amazes me.

The bedrock of my life has been my family, whose love and affection have followed me everywhere. The best times in my childhood were spent with my cousins, aunts, uncles, grandparents, brothers, and parents. Amazingly, the same is true today, through the deep friendships we've maintained even as our lives change. This has been the most significant experience in my life, a constant wellspring of generosity and vision. In the work reported herein and all I pursue now that it is done, I hope to honor the compassion, thoughtfulness, wit, spirit, and passion that my family has shared with me.

Chapter 1

Oxygen-Atom Transfer Chemistry and Thermolytic Properties of a Di-*tert*-Butylphosphate-Ligated Mn_4O_4 Cubane[1]

1.1 Introduction

Multinuclear transition metal complexes with bridging oxo ligands are of great interest for their ability to mediate multi-step oxidations. A particularly promising catalytic application of this redox chemistry is in artificial photosynthesis, which requires the oxidation of water by a four-electron process. Water oxidation catalysts as markedly different as the Photosystem II Oxygen-Evolving Complex (OEC),[2] the inorganic "cobalt-phosphate" electrocatalyst,[3,4] and the ruthenium blue dimer[5] all contain metal-oxo active sites.

The oxidation chemistry mediated by metal-oxo clusters, as in the example of water-splitting, may sometimes[6-11] (but not always)[12,13] involve oxygen-atom transfers of the oxo ligands. Additionally, O-atom transfer processes may be required for certain catalytic reactions, for example in olefin epoxidation[14] and C–H hydroxylation.[11,15-17] Therefore, metal-oxo complexes that readily donate an oxygen atom, and are regenerated by reaction with a simple oxidant (e.g. dioxygen, hydrogen peroxide, or organic peroxides), are of considerable interest.[18]

The metal-oxo "cubane" cluster $Mn_4(\mu_3\text{-}O)_4[O_2PPh_2]_6$ reported by Dismukes and co-workers[19,20] is closely related to the natural OEC in structure, with alternating manganese and oxygen atoms arranged in a cube of approximate T_d symmetry. Reactivity of its core oxo ligands to generate dioxygen (on irradiation)[21] and water (on treatment with a H• donor)[22] comprises a partially realized water oxidation cycle. In light of previous work on the improvements made possible by immobilization of Mn-oxo clusters,[23-25] complexes containing the $Mn_4(\mu_3\text{-}O)_4$ cubane unit (hereafter Mn_4O_4) are promising candidates[26,27] for molecular precursor chemistry designed to incorporate the Mn_4O_4 structure into a stable, inorganic network.

Thermolytic molecular precursors (TMPs) provide routes to inorganic materials of controlled structure.[28-45] In one application of such precursors, a catalytic site of interest is introduced onto a support material (e.g., onto an oxide surface).[46-50] For thermolytic molecular precursor chemistry with Mn_4O_4, an appropriate precursor should possess ligands that render the precursor complex soluble (for processing) and labile (for the low-temperature elimination of organic components). These criteria are associated with complexes of the di-*tert*-butylphosphate ligand $O_2P(O\textit{t}Bu)_2$.[28,30,31,36,38-42]

Complexes of $O_2P(O\textit{t}Bu)_2$ with Zn,[28] Al,[31] Co,[38,39,41] Cu,[40] Cd,[40] and Mo[36] dissolve in organic solvents and convert upon heating to metal phosphate materials by clean elimination of isobutene and water. In addition, several di-*tert*-butylphosphate complexes of manganese have been reported. Sathiyendiran and Murugavel described $[Mn(O_2P(O\textit{t}Bu)_2)_2]_n$, a coordination polymer, and $Mn_4(\mu_4\text{-}O)(O_2P(O\textit{t}Bu)_2)_6$, an oxo-bridged manganese tetramer.[40] These complexes undergo thermal elimination of isobutene below 200 °C, and further heating to 450 °C produces $Mn(PO_3)_2$, $Mn(PO_3)_3$, and $Mn_2P_2O_7$.

A related ligand of potential utility in precursor chemistry, the cyclic pinacol phosphate $O_2PO_2C_2Me_4$ ($O_2P(pin)$), has yet to be explored in thermolytic routes to phosphate materials. This ligand might be expected to provide low-temperature eliminations

of 2,3-dimethylbutadiene to yield the phosphate material after appropriate processing. To our knowledge, this ligand has not previously been employed in transition-metal chemistry.

Herein, the synthesis, properties, and reactivity of a new molecular precursor cubane, $Mn_4O_4[O_2P(O\mathit{t}Bu)_2]_6$ (**1**) are described. Attempted isolation of a cubane complex containing the $O_2P(pin)$ ligand instead gave a "butterfly" complex, $Mn_4O_2[O_2P(pin)]_6(bpy)_2$ (**2**). An O-atom transfer from complex **1** to triethylphosphine produced a second butterfly structure, $Mn_4O_2[O_2P(O\mathit{t}Bu)_2]_6(OPEt_3)_2$ (**3**). Interestingly, the cubane structure **1** is regenerated by the addition of PhIO (an O-atom donor) to complex **3**. Finally, thermolyses of complex **1** under several conditions were found to invariably give inorganic phosphate materials with substantial reduction to Mn^{II}.

1.2 Results and Discussion

*1.2.1 Synthesis and properties of the Mn_4O_4 cubane complex **1***

The manganese-oxo complex $Mn_4O_4[O_2P(O\mathit{t}Bu)_2]_6$ (**1**) was prepared using a procedure analogous to that reported for $Mn_4O_4[O_2PPh_2]_6$.[19] Two equivalents of the mixed-valence dimanganese complex $[(bpy)_2Mn(\mu_2\text{-}O)_2Mn(bpy)_2](ClO_4)_3$[51] reacted in acetonitrile with $NBu_4[O_2P(O\mathit{t}Bu)_2]$[52] (eq 1). Since the ^1H NMR signals for ligands of both the Mn_2O_2 precursor and the Mn_4O_4 product are paramagnetically broadened, reaction progress was monitored by integration of the signals for diamagnetic species in solution. When the expected quantity of 2,2'-bipyridine (bpy) was observed (as indicated by the bpy/NBu_4 ratio), the reaction was considered complete (about 24 h). Evaporation of solvent produced a red solid, which readily dissolved in organic solvents but was difficult to separate from bpy. The bpy was carefully removed from the product by sublimation under high vacuum at 70 °C. Analytically pure red crystals of complex **1** were then grown in 74% yield by cooling a concentrated hexane solution to –30 °C.

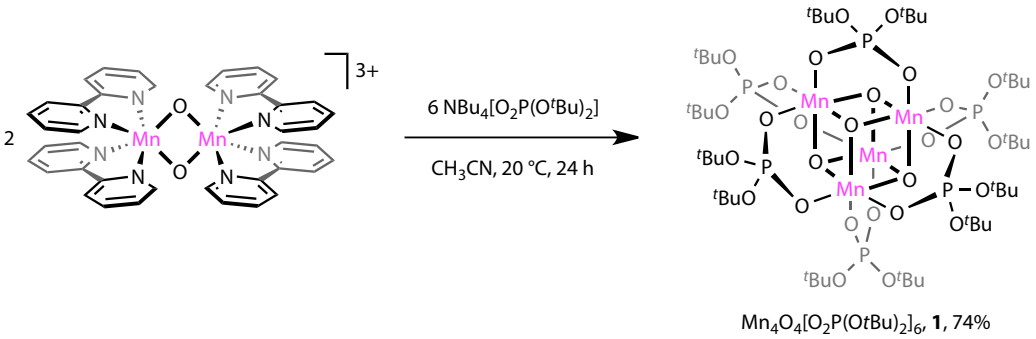

(1)

The ^1H NMR spectrum of compound **1** in $[D_2]$dichloromethane contains a single, broad peak with a half-height width of 190 Hz at 20 °C. No ^{13}C or ^{31}P NMR signals were observed over the temperature range of 238–303 K. High resolution, positive-mode

electrospray ionization time-of-flight mass spectrometry (ESI-TOF-MS) revealed a weak peak corresponding to oxidized complex $\mathbf{1}^{+}$ (m/z = 1538.31).

The structure of complex **1**, as determined by single crystal X-ray diffraction at 100 K, is shown in Figure 1. Two independent molecules in the asymmetric unit possess similar structures, containing an Mn_4O_4 core with each Mn_2O_2 face of the cube bridged by a $O_2P(O\textit{t}Bu)_2$ ligand (Figure 1a). Both molecules exhibit Mn–O_{oxo} bond length alternations that reflect the presence of two Mn^{III} and two Mn^{IV} centers. Relatively short and uniform Mn–O_{oxo} bond lengths are associated with the Mn^{IV} centers (av 1.88±0.04 Å, Figure 1b), whereas the Mn^{III} sites exhibit a wide range of distances (from 1.850(4) to 2.236(3) Å) that are longer on average (av 2.01±0.15 Å) and consistent with an expected Jahn-Teller distortion for d^4. Furthermore, the O_{oxo}–Mn–O_{oxo} angles for the Mn^{III} sites (av 80±2°) deviate more dramatically from an idealized cubic geometry than do the angles for the Mn^{IV} sites (av 85±2°). This trend is illustrated by the depiction of a particular Mn_2O_2 face in Figure 1c.

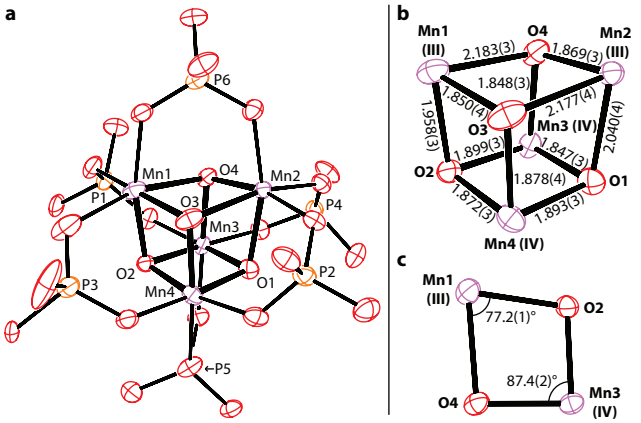

Figure 1. The structure of $Mn_4O_4[O_2P(O\textit{t}Bu)_2]_6$ (**1**). For the first of the two molecules in the asymmetric unit: (a) Thermal ellipsoids at 50% probability. Carbon and hydrogen atoms omitted for clarity. (b) Detailed structure of the Mn_4O_4 core, including M–O_{oxo} distances (esd's) in Å. (c) The Mn_2O_2 face containing Mn1 and Mn3, including angles (esd's) in degrees.

The clear distinction of Mn^{III} and Mn^{IV} sites in the structure of cluster **1** contrasts with what has been reported previously for the structure $Mn_4O_4[O_2PPh_2]_6$, which appears to possess equivalent Mn centers.[19] This difference might be attributed to the temperatures for data collection (100 K for **1**; 298 K for $Mn_4O_4[O_2PPh_2]_6$); however, a later determination of the structure of $Mn_4O_4[O_2PPh_2]_6$ at 150 K also revealed roughly equivalent Mn–O bond distances in the cube.[53] Interestingly, the structure determined for $Mn_4O_4[O_2P(p\text{-}OMe\text{-}C_6H_4)_2]_6$ at 120 K contains Mn^{III} and Mn^{IV} sites that are well resolved.[54] The equivalent sites in the structure of $Mn_4O_4[O_2PPh_2]_6$ might result either from positional disorder in the crystal structure or from electron exchange. However, a lack of sharp electronic absorption

peaks in the 200–1500 nm range that could easily be identified as intervalence charge transfer bands, for all of the aforementioned complexes, precludes further assignment.

Compound **1** displays electrochemical oxidation and reduction events in organic solution at approximately the same potentials as does $Mn_4O_4[O_2PPh_2]_6$, but, in contrast to the phosphinate complex, no reversible waves suggesting a stable ion ($\mathbf{1}^+$ or $\mathbf{1}^-$) were observed.

Variable-temperature SQUID magnetic susceptibility data collected on complex **1** revealed a μ_{eff} of 7.3 Bohr magnetons (BM) at 300 K, which is lower than the value predicted by the spin-only formula (8.8 BM for uncoupled centers) but consistent with the value reported for $Mn_4O_4[O_2PPh_2]_6$ (7.6 BM).[53] This observation indicates extensive magnetic coupling within the cubane (see Chapter 2 for details).

In contrast to $Mn_4O_4[O_2PPh_2]_6$, $Mn_4O_4[O_2P(O\textit{t}Bu)_2]_6$ (**1**) is highly soluble in a variety of organic solvents, including pentane, toluene, diethyl ether, THF, acetonitrile, and dichloromethane. This property makes complex **1** amenable to applications involving solution processing. However, exposure of complex **1** to air resulted in slow decomposition through an apparent reaction with atmospheric moisture. It was, therefore, handled and stored under dry conditions. The moisture sensitivity of complex **1** differs from the properties of the Mn^{II}-$O_2P(O\textit{t}Bu)_2$ polymer $[Mn(O_2P(O\textit{t}Bu)_2)_2]_n$.[40]

1.2.2 Synthesis and properties of the Mn_4O_2 butterfly complex 2

Reaction of $[Mn_2O_2(bpy)_4](ClO_4)_3$ with six equivalents of the tetrabutylammonium salt of pinacol phosphate ($NBu_4[O_2P(pin)]$), under conditions identical to those used to prepare complex **1**, did not produce an Mn_4O_4 cubane. Instead, a red solid that precipitated from the brown acetonitrile reaction mixture was subsequently characterized as the butterfly compound $Mn_4O_2[O_2P(pin)]_6(bpy)_2$ (**2**, by X-ray crystallography, *vide infra*). This complex was obtained in 40% yield; however, the synthetic procedure was found to be sensitive to an impurity in the $NBu_4[O_2P(pin)]$ reagent. Since rigorously purified $NBu_4[O_2P(pin)]$ failed to give complex **2** (no solid precipitated from the acetonitrile reaction mixture, and removal of solvent followed by extraction with hexane, toluene, diethyl ether, and dichloromethane did not provide **2**), it seemed that the original batch of $NBu_4[O_2P(pin)]$ may have contained an O-atom-acceptor species as an impurity. Support for this hypothesis was obtained by addition of two equivalents of PPh_3 (as an O-atom acceptor)[11] to the reaction mixture. In this optimized synthesis (eq 2), complex **2** was obtained as a red solid in 67% yield.

The ^1H NMR spectrum of compound **2** in $[D_2]$dichloromethane contains a single, broad peak with a half-height width of 360 Hz at 20 °C. No ^{13}C or ^{31}P NMR signals were observed at any temperature. ESI-TOF-MS revealed a weak peak corresponding to oxidized complex $\mathbf{2}^+$ (m/z = 1639.17).

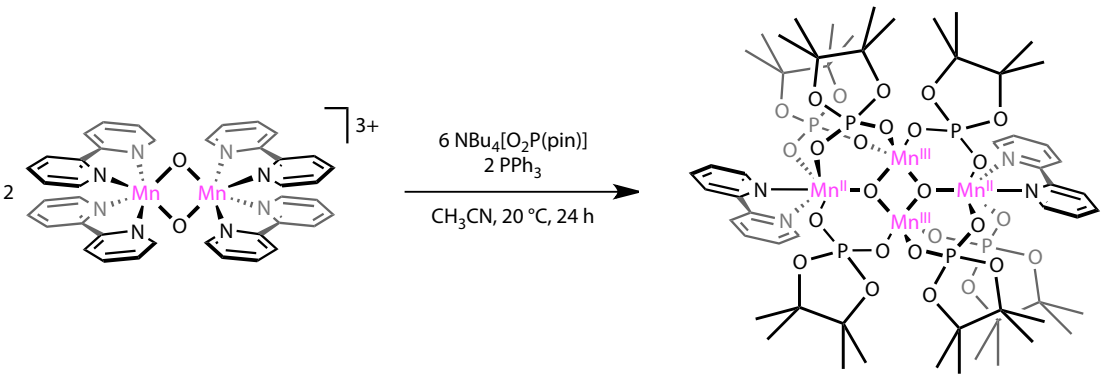

(2)

The structure of complex **2**, as revealed by X-ray crystallography at 100 K, contains an Mn_2O_2 diamond core flanked by two outer Mn centers (Figure 2). Both inner Mn centers are coordinated by two oxo and three –OPO(pin) oxygen donors and exhibit a distorted square pyramidal geometry, with O_{apical}–Mn–O_{basal} angles ranging from 90.1(1)° to 111.4(1)°. The outer Mn centers, each ligated by one oxo ligand, three phosphate oxygen atoms, and one bipyridine, are in a pseudo-octahedral coordination environment. Comparison of Mn–O bond lengths in the structure allows assignment of discrete Mn^{II} and Mn^{III} centers. Shorter Mn–O_{oxo} (av 1.80±0.05 Å) and Mn–$O_{phosphate}$ (av 1.98±0.11 Å) distances observed for the inner Mn sites are consistent with Mn^{III}, while longer Mn–O_{oxo} (av 2.01±0.03 Å) and Mn–$O_{phosphate}$ (av 2.15±0.02) distances for the outer sites indicate Mn^{II}.

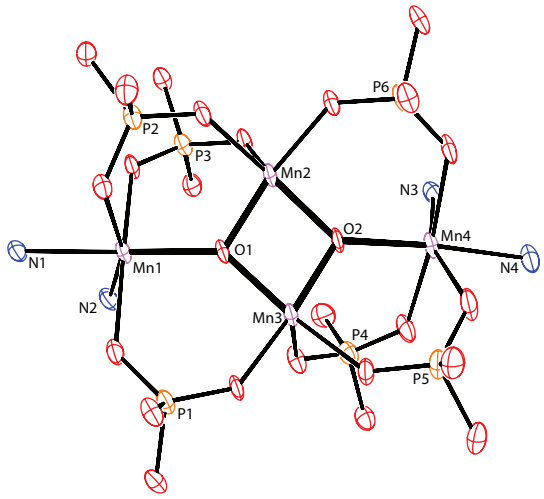

Figure 2. Thermal ellipsoids at 50% probability of the structure of $Mn_4O_2[O_2P(pin)]_6(bpy)_2$ (**2**). Carbon and hydrogen atoms were omitted for clarity.

A previously reported complex, $Mn_4O_2[O_2CCH_3]_6(bpy)_2$, is a structural analogue of complex **2** with similar connectivity and the same arrangement of Mn^{II} and Mn^{III} sites.[55] The

complexes differ in that the carboxylate cluster has an imposed center of inversion, while the phosphate cluster **2** has approximate two-fold rotation symmetry.

*1.2.3 O-atom transfer from cubane **1** to triethylphosphine*

It was of interest to investigate cubane **1** as a possible source of O atoms in oxidation chemistry. Thus, an attempt was made to observe O-atom transfer from **1** to triethylphosphine with formation of $OPEt_3$. Complex **1** reacted upon addition of excess triethylphosphine to generate the butterfly complex $Mn_4O_2[O_2P(O\textit{t}Bu)_2]_6(OPEt_3)_2$ (**3**, eq 3). After removal of solvent and unreacted phosphine, red-violet crystals of complex **3** grew from hexane solution in 77% yield. As in the parent cubane **1**, only broadened signals were observed by ^1H NMR spectroscopy and no ^{13}C or ^{31}P NMR signals were observed. A broad, unresolved ^1H NMR peak observed in $[D_2]$dichloromethane at 20 °C had a half-height width of 640 Hz. As determined by X-ray crystallography (*vide infra*), two oxo ligands were removed from **1** to form the butterfly complex **3**, shown in eq 3. Note that this process differs from that observed by Agapie and co-workers, in which an Mn_4O_4 cubane reacted with trimethylphosphine *via* transfer of one oxygen atom, to produce an Mn_4O_3 partial cubane and $OPMe_3$.[56]

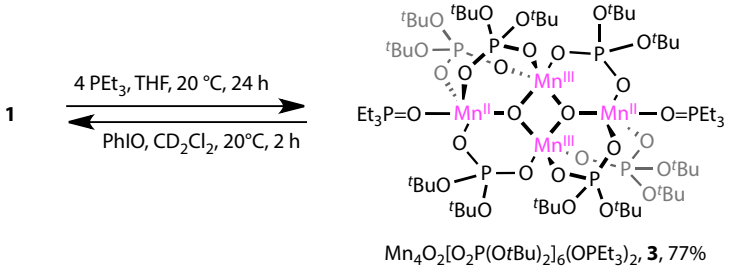

(3)

Product **3** crystallized in space group *P* -1 with inversion symmetry imposed on the cluster and $Z = 1$ (Figure 3). The arrangement of an inner $Mn^{III}_2O_2$ diamond, two outer Mn^{II} sites, and six bridging phosphate ligands observed for complex **2** is preserved in complex **3**. The complexes differ in the replacement of bpy with $OPEt_3$ as the terminal ligand, which results in all four metal centers of complex **3** being five-coordinate. Using the τ bond-angle parameter proposed by Addison *et al.*,[57] the inner Mn sites of complex **3** were found to have a geometry intermediate between square pyramidal and trigonal bipyramidal ($\tau = 0.55$). These inner centers are associated with Mn^{III} on the basis of their shorter $Mn–O_{oxo}$ (1.840(3), 1.860(2) Å) and $Mn–O_{phosphate}$ (av 2.03±0.06 Å) distances. The outer Mn sites possess a trigonal bipyramidal geometry and longer $Mn–O_{oxo}$ (2.179(2) Å) and $Mn–O_{phosphate}$ (av 2.06±0.01 Å) distances, indicating Mn^{II}. A previously described complex, $Mn_4O_2[O_2CCPh_3]_6(OEt_2)_2$, is a structural analogue of **3**.[58]

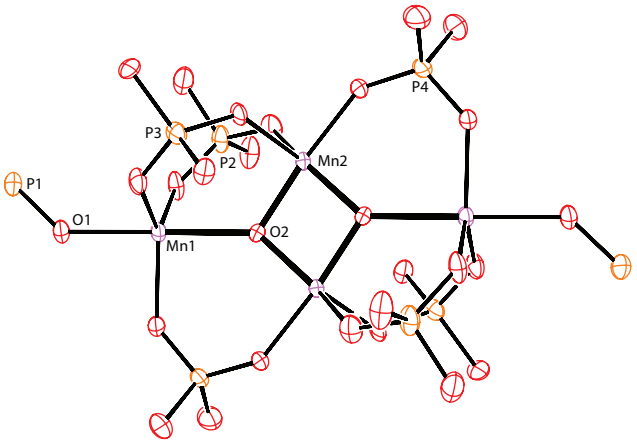

Figure 3. Thermal ellipsoids at 50% probability of the structure of $Mn_4O_2[O_2P(O\textit{t}Bu)_2]_6(OPEt_3)_2$ (**3**). Carbon and hydrogen atoms were omitted for clarity.

Interestingly, the complete Mn_4O_4 cubane structure of complex **1** was restored by the stoichiometric reaction of complex **3** with iodosobenzene, an O-atom donor. In $[D_2]$dichloromethane solution, the reaction was monitored by ^1H NMR spectroscopy, using ferrocene as an internal standard. This reaction occurred over about 2 h, as indicated by the integration values for signals of **3**, **1**, and PhI (a byproduct), with a single apparent Mn product (**1**) and a final conversion of 55–65%. The identity of the product **1** was confirmed by ESI-TOF-MS. Note that the interconversion of **1** and **3** is related to the "double-pivot" mechanism previously proposed for water oxidation in the Photosystem II OEC,[59,60] although this mechanism is inconsistent with current structural models.[61-63]

*1.2.4 Thermolysis of complex **1** to manganese phosphate materials*

The potential use of $Mn_4O_4[O_2P(O\textit{t}Bu)_2]_6$ (**1**) as a thermolytic precursor to manganese phosphate materials was examined. Thermogravimetric analysis (TGA) of complex **1** revealed a slow thermolytic process at 100 °C. Heating at a constant rate of 5 °C/min under flowing N_2 resulted in a sharp mass loss of 44% from 130–150 °C (Figure 4), consistent with elimination of isobutene. A gradual process, assigned as elimination of water through cross-linking of phosphate groups, continued from this temperature up to approximately 500 °C. The volatile thermolysis products at 200 °C were confirmed to be isobutene (10.3 equivalents) and water (1.0 equivalents) by vacuum transfer into a cooled NMR tube containing toluene-d_8 and ferrocene as an internal standard.

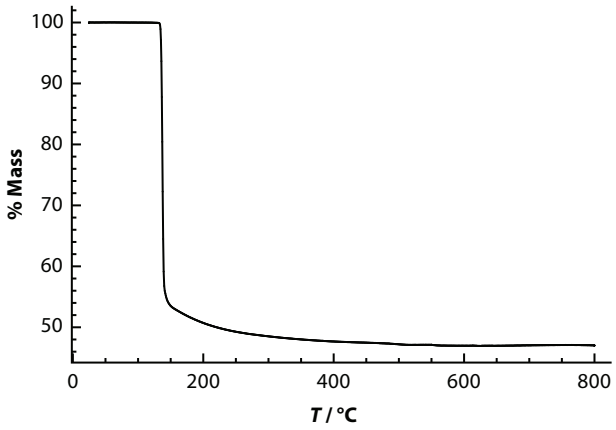

Figure 4. Thermogravimetric analysis (TGA) trace of complex **1** on heating at 5 °C/min to 800 °C under flowing N_2.

Bulk crystallization appears to occur between 550 °C and 800 °C, as samples heated to the former temperature during TGA did not exhibit any peaks in their powder XRD spectra. Samples heated to 800 °C, by contrast, displayed XRD peaks consistent with a manganese metaphosphate-pyrophosphate mixture (Figure 5): $2Mn(PO_3)_2$-$Mn_2P_2O_7$ ($Mn_4P_6O_{19}$).[64,65] This ratio of phosphates agrees with the stoichiometry of Mn and P in complex **1** and with the final ceramic yield at 800 °C: 46.1% expected, 47.0% observed.

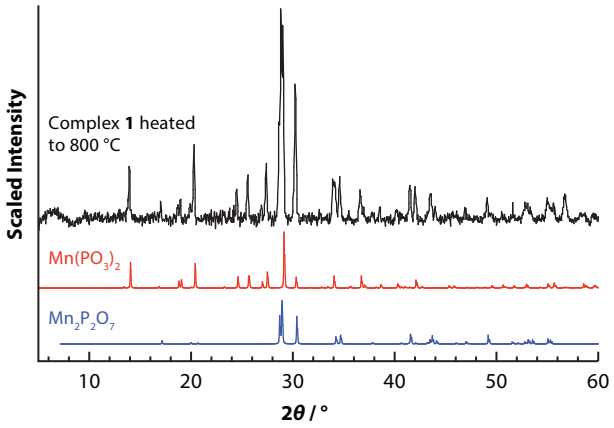

Figure 5. Powder XRD patterns: Compound **1** heated to 800 °C during TGA (black, background removed by fitting), manganese metaphosphate (red, PDF Card 04-010-8577),[64] and manganese pyrophosphate (blue, PDF Card 00-035-1497).[65]

The solution-phase transformation of cubane **1** to an inorganic substance was investigated by heating a red solution of the complex in toluene at 160 °C for 30 min. A brown gel formed, from which solvent was removed by decantation and application of

vacuum. The resulting brown solid did not display peaks by powder XRD after preparation, and no XRD peaks were observed after heating the gel for 5 h at 500 °C under flowing O_2. A sample calcined for 5 h at 800 °C under O_2 displayed an XRD pattern similar to that in Figure 5, indicating a mixture of Mn metaphosphate and pyrophosphate.[64,65]

Solution-phase co-thermolyses of compound **1** with other oxide precursors were investigated, as a potential means for isolation of $Mn_4O_4(PO_4)_6$ units within an oxide matrix. For this purpose, the thermolytic precursors $[Al(O\textit{i}Pr)_2O_2P(O\textit{t}Bu)_2]_4$ (to aluminophosphate)[31] and $Zr[OSi(O\textit{t}Bu)_3]_4$ (to zirconia-silica)[29,66] were used, given their low-temperature, clean transformations to inorganic materials. In a typical preparation, compound **1** with the added precursor (in a 1:10 mass ratio) were heated in toluene to 160 °C for 30 min. The resultant gels crystallized on heating to 800 °C under flowing O_2, but no evidence of any mixed-metal phase was observed. The powder XRD patterns reflect the presence of a combination of the expected materials from single-component thermolyses. This finding indicates that distinct crystalline phases of Mn-metaphosphate and -pyrophosphate, and the accompanying $AlPO_4$ or ZrO_2•$4SiO_2$, have formed.[29,31]

The thermolytic properties of complex **2**, as investigated by TGA, indicate that a clean low-temperature transformation to a purely inorganic phosphate material does not occur, presumably due to the presence of the bipyridine ligands.

*1.2.5 X-ray absorption spectroscopy of materials derived from precursor **1***

The fate of the Mn_4O_4 cubane unit in the aforementioned phosphate materials is of interest in the context of general strategies for metal-oxo cluster immobilization. Useful protocols will deliver the core structure of interest, intact, into a robust supporting material. It is therefore critical to develop reliable methods for identification of intact cubanes in molecular and extended materials.

Since both $Mn_4O_4[O_2P(O\textit{t}Bu)_2]_6$ (**1**) and $Mn_4O_4[O_2PPh_2]_6$ contain the Mn_4O_4 cube that these studies seek to deliver, intact, into new inorganic materials, any spectroscopic feature appearing in both might serve as a characteristic signature for the desired Mn_4O_4 unit. Routine magnetic (NMR, EPR), vibrational (infrared, Raman, confocal resonance Raman), and electronic (ultraviolet/visible, X-ray photoelectron) spectroscopies revealed no clear identifying feature shared by the two complexes, so Mn X-ray absorption spectroscopy (XAS) was employed.

Mn XAS on $Mn_4O_4[O_2P(O\textit{t}Bu)_2]_6$ (**1**) and $Mn_4O_4[O_2PPh_2]_6$ revealed several identifying features that collectively signify the presence of an Mn_4O_4 cube. First, the Mn K-edge energy, associated with formal Mn oxidation state, is consistent between the two cubane complexes (Figure 6a). Taken as the zero crossing of the second derivative X-ray absorption near edge structure (XANES) spectrum, the edge energies of 6550.15 eV for complex **1** and 6550.58 eV for $Mn_4O_4[O_2PPh_2]_6$ fall in the same energy range as that reported previously for a manganese(3.5) cubane.[67] Second, information on Mn coordination environment from extended X-ray absorption fine structure (EXAFS) spectroscopy (Figure 6b) is consistent between the two complexes. Furthermore, a crystal structure-based fit to the Fourier

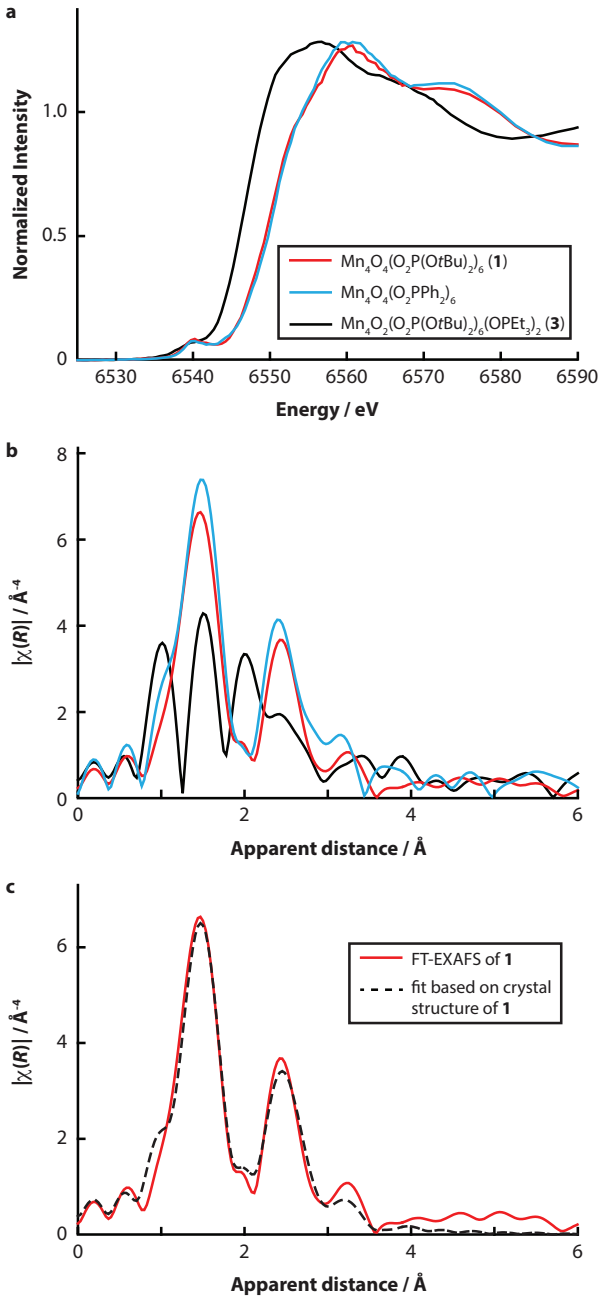

Figure 6. Mn K-edge absorption spectra of complex **1** (red), $Mn_4O_4[O_2PPh_2]_6$ (blue), and complex **3** as an Mn_4 non-cubane reference compound (black): (a) XANES (b) FT-EXAFS (c) FT-EXAFS curve-fit results for complex **1** only.

transform EXAFS spectrum of **1** produced good agreement (Figure 6c). Finally, for comparison, the XAS signature of the butterfly complex **3** is included in Figure 6a,b. Its edge energy (6546.89 eV) and FT-EXAFS spectrum differ markedly from those of $Mn_4O_4[O_2P(O\textit{t}Bu)_2]_6$ (**1**) and $Mn_4O_4[O_2PPh_2]_6$.

The application of XAS to the materials produced by thermolyses indicates that in all cases the Mn_4O_4 cubane unit is transformed. This result is exemplified by data collected for two thermolysis products that provided good EXAFS signals: the dried gel produced from solution-phase thermolysis of complex **1**, and the dried gel obtained from co-thermolysis of 1:10 complex **1** and $Zr[OSi(O\textit{t}Bu)_3]_4$. For both materials, a sharp XANES peak and edge energy shift (to 6546.70–6546.93 eV) reveal reduction of Mn centers from the precursor oxidation state of $Mn^{3.5}$ to Mn^{II} (Figure 7a). Furthermore, a sharp FT-EXAFS peak associated with Mn–Mn and Mn–P scattering in complex **1**, between 2 and 3 Å in apparent distance, is not evident in the two thermolytic products (Figure 7b). The loss of this peak is consistent with breakup of the Mn_4O_4 units into Mn sites with varying coordination environments and (on average) long Mn–Mn distances. Taken together, these results suggest decomposition of the Mn_4O_4 cluster in **1** to isolated Mn^{II} sites.

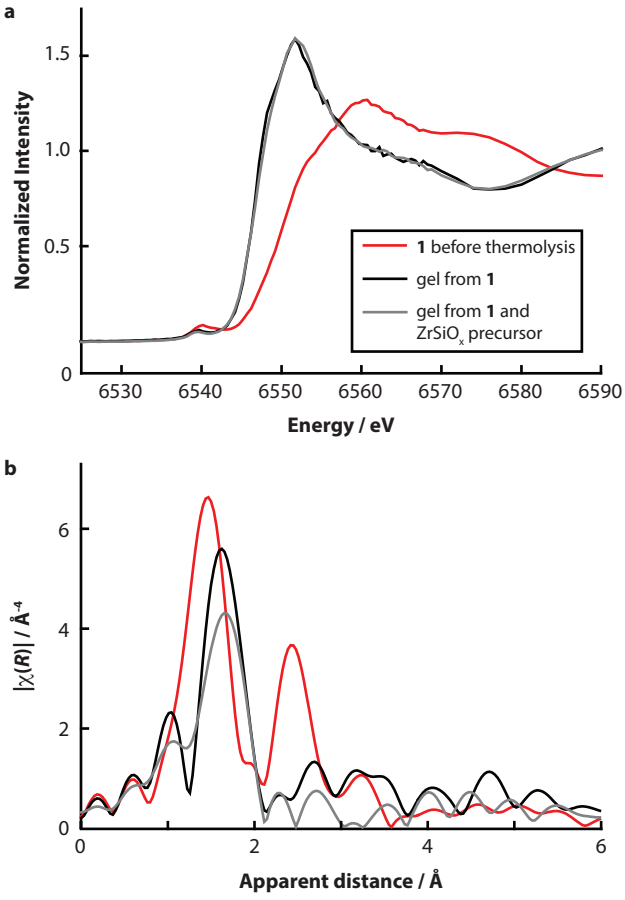

Figure 7. Mn K-edge absorption spectra of complex **1** (red), a gel produced by solution-phase thermolysis of **1** (black), and a gel produced by solution-phase co-thermolysis of 1:10 complex **1** and $Zr[OSi(O\textit{t}Bu)_3]_4$ (grey): (a) XANES (b) FT-EXAFS.

In light of XAS evidence for thermolytic reduction of the $Mn^{III/IV}$ sites in $Mn_4O_4[O_2P(O\textit{t}Bu)_2]_6$ (**1**) to isolated Mn^{II}, the possible evolution of dioxygen from the complex's core oxo ligands was considered.[21,68] To investigate this possibility, mass spectral analysis of volatile thermolysis products was employed. Under an atmosphere of argon (150 torr), a sample of complex **1** was heated to 170±10 °C for one hour. The flask was then connected to a vacuum system designed for controlled delivery of headspace gas to a quadrupole mass spectrometer. While up to two equivalents of dioxygen might be expected from complex **1**'s four oxo ligands, only 0.36(2) equivalents were observed.

*1.2.6 Electrochemical water oxidation activity of complex **1** and thermolytic materials*

The ultimate aim of this work is the preparation of efficient water oxidation catalysts from Mn_4O_4 cubane molecular precursors. Unfortunately, none of the precursors or inorganic materials described herein are significant catalysts for water oxidation under the conditions employed. Electrode-adsorbate assemblies were prepared by spin-coating, drop-casting, immersion in a precursor solution during thermolysis, attempted ligand exchange (electrostatic anchoring) with surface –OH groups, and organic linker ($-PO_3$-terminated) strategies (more details are provided in Chapter 3). Cyclic voltammetry and electrolysis were performed in 1 M KOH solution. In all cases, overpotentials (relative to the thermodynamic potential for water oxidation) exceeded one volt for electrochemical water oxidation at a current density of 10 mA cm^{-2}.

1.3 Conclusions

The solubility properties of complex **1** are quite conducive to physical characterization and reactivity studies. Most significantly, this work demonstrates a structural change of the Mn_4O_4 cubane core upon transfer of two oxygen atoms to triethylphosphine. Reactivity of the resulting butterfly **3** with an oxygen-atom donor to regenerate the original cubane structure supports the possibility of oxidation catalysis by complexes of this type. The properties of **1** also indicate that it has potential as a precursor to materials containing the inorganic $Mn_4O_4(PO_4)_6$ unit. However, under the few conditions examined so far, the thermolytic process that converts **1** to an inorganic material is accompanied by reduction of the manganese centers and a structural change that degrades the cubane unit. Future efforts will focus on precursor transformations (and related molecular precursors) that preserve the oxidation state and structure of the inorganic Mn_4O_4 core while delivering it to a surface or thin film. In this regard, the identification of XANES and EXAFS features for molecular manganese cubanes has greatly enabled the pursuit of inorganic materials containing discrete M_4O_4 cubane units, as demonstrated in Chapters 3 and 4.

1.4 Acknowledgements

J. M. Zadrozny and J. R. Long (magnetic susceptibility), A. T. Iavarone (ESI-TOF-MS), M. S. Ziegler (single-crystal XRD), and W. Kim and H. Frei (MS detection of O_2) are gratefully acknowledged for their contributions in characterizing the compounds herein. This material is based upon work performed by the Joint Center for Artificial Photosynthesis, a DOE Energy Innovation Hub, supported through the Office of Science of the U.S. Department of Energy under Award Number DE-SC0004993. K.M.V. acknowledges support from a National Science Foundation Graduate Research Fellowship under Grant No. DGE-1106400. Single-crystal X-ray structure determination was supported by NIH Shared Instrumentation Grant S10-RR027172. The Advanced Light Source is supported by the Director, Office of Science, Office of Basic Energy Sciences, of the U.S. Department of Energy under Contract No. DE-AC02-05CH11231.

1.5 Experimental Details

General procedures. Unless otherwise noted, compounds were synthesized and manipulated under air-free conditions, using either a Vacuum Atmospheres drybox or standard Schlenk technique under a dry nitrogen atmosphere. Dry solvents were obtained using a commercial solvent purification system from JC Meyer Solvent Systems.

NMR spectra were recorded on a Bruker Avance III 500 MHz spectrometer. All spectra were referenced to residual internal solvent signals. TGA was performed using a Thermal Analysis Q50 TGA unit. Powder XRD data were collected using a Rigaku SmartLab diffractometer.

The mixed-valence dimanganese complex $[(bpy)_2Mn(\mu_2\text{-}O)_2Mn(bpy)_2](ClO_4)_3$[51] and the phosphate ligands $NBu_4[O_2P(O\textit{t}Bu)_2]$[52] and $NBu_4[O_2P(pin)]$[69] were synthesized as described previously.

$Mn_4O_4[O_2P(O\textit{t}Bu)_2]_6$ (1). A procedure similar to that described in ref. 19 was used. The dimanganese complex $[(bpy)_2Mn(\mu_2\text{-}O)_2Mn(bpy)_2](ClO_4)_3$ (1.32 g, 1.24 mmol), $NBu_4[O_2P(O\textit{t}Bu)_2]$ (1.68 g, 3.72 mmol), and acetonitrile (75 mL) were stirred at 20 °C for 24 h. During this time, the mixture's appearance changed from a green-brown suspension to a deep red solution, and the ^{1}H NMR ratio of free 2,2'-bipyridine Ar-*H* to tetrabutylammonium –C*H*$_2$– reached 1:3, indicating reaction completion. Removal of acetonitrile *in vacuo*, extraction with hexane, filtration, and removal of hexane *in vacuo* produced a red solid, which was heated to 70 °C for 1 h under high vacuum (~10^{-3} torr) to remove 2,2'-bipyridine by sublimation. The dark red residue was dissolved in minimal hexane and cooled to –30 °C, producing red crystals of complex **1** (0.70 g) in 74% yield. Crystals suitable for single crystal XRD were grown by slow cooling of a pentane solution. ^{1}H NMR (CD_2Cl_2, 500 MHz, 293 K): δ 1.61 (s, broad). Attempts to observe ^{13}C or ^{31}P NMR signals for this complex were unsuccessful. IR (attenuated total reflectance, diamond, cm^{-1}): 2976 m, 2932 w, 2907 vw sh, 2875 w sh, 1474 w, 1459 w sh, 1393 m, 1369 m, 1248 m, 1176 m, 1124 m, 1103 w, 988 vs, 917 w, 833 m, 815 w, 725 m, 711 m sh, 692 w sh, 637 m, 602 m,

578 w, 526 s, 477 s, 417 m. Anal. Calcd. for $C_{48}H_{108}Mn_4O_{28}P_6$: C, 37.5; H, 7.07. Found: C, 37.5; H, 7.03.

$Mn_4O_2[O_2P(pin)]_6(bpy)_2$•0.5$CH_2Cl_2$ (2•0.5CH_2Cl_2). The dimanganese complex $[(bpy)_2Mn(\mu_2\text{-}O)_2Mn(bpy)_2](ClO_4)_3$ (0.30 g, 0.28 mmol), $NBu_4[O_2P(pin)]$ (0.36 g, 0.84 mmol), and PPh_3 (0.074 g, 0.28 mmol) were dissolved in acetonitrile (30 mL). The dark green mixture was stirred for 24 h at room temperature. A red crystalline solid was collected by filtration and washed with acetonitrile (10 mL), diethyl ether (20 mL), toluene (40 mL), and hexane (20 mL). The product was extracted into dichloromethane solution, which was evaporated to produce a red-violet solid (**2•0.5CH_2Cl_2**, 0.16 g) in 67% yield. Crystals suitable for single crystal XRD were grown by vapor diffusion of diethyl ether into a dichloromethane solution. ^{1}H NMR (CD_2Cl_2, 500 MHz, 293 K): δ 2.08 (s, broad). Attempts to observe ^{13}C or ^{31}P NMR signals for this complex were unsuccessful. IR (attenuated total reflectance, diamond, cm^{-1}): 2981 m, 2936 w, 1645 w, 1596 m, 1577 w, 1477 m, 1440 m, 1392 m, 1372 m, 1319 w, 1214 s, 1165 w sh, 1148 m, 1121 w, 1083 vs, 1061 s sh, 1009 m, 967 s, 923 s, 866 s, 817 s, 766 s, 739 m, 725 s, 694 w, 646 s, 595 s, 583 w sh, 555 s, 526 w sh, 526 s, 448 s, 420 vw sh. Anal. Calcd. for $C_{56}H_{88}N_4Mn_4O_{26}P_6$•0.5$CH_2Cl_2$: C, 40.4; H, 5.33; N, 3.33. Found: C, 40.2; H, 5.19; N, 3.39.

$Mn_4O_2[O_2P(O\mathit{t}Bu)_2]_6(OPEt_3)_2$ (3). The Mn_4O_4 cubane **1** (0.26 g, 0.17 mmol) was dissolved in tetrahydrofuran (50 mL) and triethylphosphine (0.10 mL, 0.68 mmol) was added. No color change was initially observed, but the red reaction mixture gradually became more violet in color as it was stirred at room temperature over 24 h. The solvent and unreacted phosphine were removed *in vacuo*, leaving the product as a red-violet solid in apparent quantitative yield, but with silicone grease as a contaminant. The solid was dissolved in minimal hot hexane and the solution was cooled to –80 °C, producing red-violet crystals of complex **3** (0.23 g) in 77% yield. Crystals suitable for single crystal XRD were grown by slow cooling of a hexane solution. ^{1}H NMR (CD_2Cl_2, 500 MHz, 293 K): δ 2.12 (m, broad). Attempts to observe ^{13}C or ^{31}P NMR signals for this complex were unsuccessful. IR (attenuated total reflectance, diamond, cm^{-1}): 2974 s, 2931 m, 2881 w, 1476 m, 1458 m, 1417 w, 1391 m, 1365 s, 1296 w, 1206 s, 1136 s, 1070 vs, 1036 s, 1010 w sh, 984 vs, 916 s, 831 s, 779 s, 716 s, 684 m, 648 s, 614 w sh, 594 m, 547 s, 509 m, 491 w, 474 s, 447 w. Anal. Calcd. for $C_{60}H_{138}Mn_4O_{28}P_8$: C, 40.6; H, 7.84. Found: C, 40.9; H, 7.52.

X-ray crystallographic structure determination. X-ray diffraction analysis was performed on a single crystal coated in Paratone-N oil, mounted on a Kaptan loop, and transferred to a Bruker Quazar four-circle diffractometer. The crystal was cooled to 100(2) K by a stream of nitrogen gas. Data were collected using *phi* and *omega* scans with a Bruker APEX-II CCD and monochromated Mo-K_α radiation (λ = 0.71073 Å). The data were integrated and corrected for Lorentz effects and polarization using Bruker APEX2 software and were corrected for absorption using SADABS (**1** and **2**) or TWINABS (**3**). Space group assignment was done by examination of systematic absences and E-statistics. The structure was solved using charge-flipping methods (SUPERFLIP, **1**)[70,71] or direct methods (SHELXS-2014, **2** and **3**)[72] and all non-hydrogen atoms were refined anisotropically using full-matrix least-squares (SHELXL-2014).[72] Hydrogen atoms were placed in ideal positions

and refined isotropically using a riding model. Because of extensive solvent disorder, SQUEEZE was used to exclude solvent electron density from the structures of **1** and **2**. Details of results for the three complexes may be found in Table 1. CCDC-1033572 (**1**), CCDC-1033571 (**2**), and CCDC-1033570 (**3**) contain the supplementary crystallographic data for this chapter. These data can be obtained free of charge from The Cambridge Crystallographic Data Centre via www.ccdc.cam.ac.uk/data%5Frequest/cif.

Table 1. Crystallographic Data for Compounds **1**-**3**.

compound	**1**	**2**	**3**•2C_6H_{12}
empirical formula	$C_{48}H_{108}Mn_4O_{28}P_6$	$C_{56}H_{88}Mn_4N_4O_{26}P_6$	$C_{72}H_{162}Mn_4O_{28}P_8$
formula weight	1538.92	1638.88	1943.53
crystal system	monoclinic	monoclinic	triclinic
space group	*C* 2	*P* $2_1/n$	*P* -1
a [Å]	35.1371(9)	14.726(3)	14.0978(8)
b [Å]	19.7817(5)	14.437(2)	14.1023(8)
c [Å]	25.0466(9)	41.650(7)	14.2236(8)
α [°]	90	90	84.144(2)
β [°]	96.7620(10)	91.877(9)	89.469(3)
γ [°]	90	90	62.213(2)
V [Å^3]	17978.3(9)	8850(2)	2486.3(2)
Z	8	4	1
ρ_{calcd} [g cm^{-3}]	1.137	1.230	1.298
μ [mm^{-1}]	0.715	0.731	0.692
transmission max/min	0.259 / 0.214	0.745 / 0.683	0.745 / 0.606
crystal size [mm^3]	0.12 × 0.08 × 0.05	0.15 × 0.09 × 0.05	0.10 × 0.09 × 0.03
θ range [°]	1.167 to 25.393	1.493 to 27.268	1.441 to 25.390
rflns collected	80887	64668	8224
rflns obsd ($I_0 > 2\sigma(I_0)$)	27942	12008	6887
parameters/restraints	1690 / 74	889 / 0	578 / 60
R_1 ($I_0 > 2\sigma(I_0)$)	0.0398	0.0486	0.0435
wR_2 (all data)	0.1055	0.1206	0.1074
GOF	1.052	1.048	1.059
largest residuals [e A^{-3}]	+ 0.595 / – 0.498	+ 0.825 / – 0.533	+ 0.484 / – 0.467

Observation of volatile thermolysis products – NMR spectroscopy. Complex **1** (0.0276 g) inside a Schlenk flask and an NMR tube containing toluene-d_8 and ferrocene (0.0225 g) were connected to opposite ends of a vacuum transfer apparatus. After the system was completely evacuated, it was isolated and the NMR tube was cooled with liquid nitrogen while the flask was immersed in an oil bath at 200±10 °C for 30 min. The volatile products were quantified by integrating their ^{1}H NMR signals against that of the ferrocene standard, after sealing the NMR tube and warming it to room temperature. To ensure accurate integrations, a long recycle delay (d1) of 180 s was used following crude measurements that

estimated ferrocene's relaxation time (T1) in toluene-d_8 as 41 s. For thermolysis of **1**, the products were isobutene (10.3 equivalents) and water (1.0 equivalents).

Observation of dioxygen from thermolysis – mass spectrometry. Complex **1** was placed (0.112 g, 72.8 μmol) in a round-bottomed flask connected to a 2.5-mL Teflon-stoppered sampling volume. The flask was thoroughly evacuated, charged with 150 torr argon, and isolated. It was heated to 170±10 ˚C for 1 hour, then opened to the sampling volume, which had previously been evacuated. The sampling volume was then opened to an evacuated line connected to a quadrupole mass spectrometer. Calibration measurements using this vacuum system and pure sources of Ar and O_2 were used to convert the observed ion current for m/z = 32 (~9.5×10^{-12} A), relative to the background signal (<2×10^{-12} A), into an observed value in mol of O_2: 26(2) μmol, which corresponds to 0.36(2) equiv O_2 evolved from complex **1**.

Solution-phase thermolysis of compound 1. In a typical preparation, cubane **1** (100 mg) or a mixture of cubane **1** (10 mg) and $Zr[OSi(O\textit{t}Bu)_3]_4$ or $[Al(O\textit{i}Pr)_2O_2P(O\textit{t}Bu)_2]_4$ (100 mg) was dissolved in anhydrous toluene (3 mL). In a sealed vessel, the mixture was heated to 160 ˚C for 20–30 min, during which time the dark red solution changed to a light brown gel. Removal of solvent *in vacuo* produced a light brown solid. Calcination was performed in a temperature-controlled tube furnace under flowing O_2.

X-ray absorption spectroscopy. X-ray absorption spectra were taken at the Advanced Light Source (ALS) on Beamline 10.3.2. The radiation was monochromatized by a Si (111) double-crystal monochromator. The intensity of the incident X-ray (I_0) was monitored by an N_2-filled ionization chamber in front of the sample. The energy was calibrated using a glitch in I_0 relative to the absorption edge of an Mn foil. All data were collected at room temperature using a quick XAS scan mode, and the data collection was carried out under the threshold of X-ray radiation damage, by monitoring with the XANES edge shift. Data reduction was performed using custom software (Matthew Markus, BL 10.3.2, ALS). Pre-edge and post-edge contributions were subtracted from the XAS spectra, and the result was normalized with respect to the edge jump.

1.6 References

(1) This chapter is based upon work that was published previously: Van Allsburg, K. M.; Anzenberg, E.; Drisdell, W. S.; Yano, J.; Tilley, T. D. *Chem. Eur. J.* **2015**, *21*, 4646–4654. It is included here with permission of all authors.

(2) Umena, Y.; Kawakami, K.; Shen, J.-R.; Kamiya, N. *Nature* **2011**, *473*, 55–60.

(3) Kanan, M. W.; Yano, J.; Surendranath, Y.; Dincă, M.; Yachandra, V. K.; Nocera, D. G. *J. Am. Chem. Soc.* **2010**, *132*, 13692–13701.

(4) Risch, M.; Khare, V.; Zaharieva, I.; Gerencser, L.; Chernev, P.; Dau, H. *J. Am. Chem. Soc.* **2009**, *131*, 6936–6937.

(5) Gersten, S. W.; Samuels, G. J.; Meyer, T. J. *J. Am. Chem. Soc.* **1982**, *104*, 4029–4030.

(6) McEvoy, J.; Brudvig, G. W. *Chem. Rev.* **2006**, *106*, 4455–4483.

(7) Barber, J.; Murray, J. W. *Phil. Trans. R. Soc. B* **2008**, *363*, 1129–1138; discussion 1137–1138.
(8) Brudvig, G. W. *Phil. Trans. R. Soc. B* **2008**, *363*, 1211–1219.
(9) Meelich, K.; Zaleski, C. M.; Pecoraro, V. L. *Phil. Trans. R. Soc. B* **2008**, *363*, 1271–1281.
(10) Siegbahn, P. *Acc. Chem. Res.* **2009**, *42*, 1871–1880.
(11) Holm, R. H. *Chem. Rev.* **1987**, *87*, 1401–1449.
(12) Liu, F.; Concepcion, J. J.; Jurss, J. W.; Cardolaccia, T.; Templeton, J. L.; Meyer, T. J. *Inorg. Chem.* **2008**, *47*, 1727–1752.
(13) Hurst, J. K.; Cape, J. L.; Clark, A. E.; Das, S.; Qin, C. *Inorg. Chem.* **2008**, *47*, 1753–1764.
(14) Lane, B. S.; Burgess, K. *Chem. Rev.* **2003**, *103*, 2457–2474.
(15) Shul'pin, G. B. *J. Molec. Catal. A: Chem.* **2002**, *189*, 39–66.
(16) Roduner, E.; Kaim, W.; Sarkar, B.; Urlacher, V. B.; Pleiss, J.; Gläser, R.; Einicke, W. D.; Sprenger, G. A.; Beifuß, U.; Klemm, E.; Liebner, C.; Hieronymus, H.; Hsu, S. F.; Plietker, B.; Laschat, S. *ChemCatChem* **2013**, *5*, 82–112.
(17) Tang, P.; Zhu, Q.; Wu, Z.; Ma, D. *Energy Environ. Sci.* **2014**, *7*, 2580–2591.
(18) Drago, R. S. *Coord. Chem. Rev.* **1992**, *117*, 185–213.
(19) Ruettinger, W.; Campana, C.; Dismukes, G. *J. Am. Chem. Soc.* **1997**, *119*, 6670–6671.
(20) Carrell, T.; Cohen, S.; Dismukes, G. *J. Molec. Catal. A: Chem.* **2002**, *187*, 3–15.
(21) Ruettinger, W.; Yagi, M.; Wolf, K.; Bernasek, S.; Dismukes, G. *J. Am. Chem. Soc.* **2000**, *122*, 10353–10357.
(22) Ruettinger, W.; Dismukes, G. *Inorg. Chem.* **2000**, *39*, 1021–1027.
(23) Yagi, M.; Narita, K. *J. Am. Chem. Soc.* **2004**, *126*, 8084–8085.
(24) Narita, K.; Kuwabara, T.; Sone, K.; Shimizu, K.-I.; Yagi, M. *J. Phys. Chem. B* **2006**, *110*, 23107–23114.
(25) Rumberger, E. M. W.; Ahn, H. S.; Bell, A. T.; Tilley, T. D. *Dalton Trans.* **2013**, *42*, 12238–12247.
(26) Gardner, G. P.; Go, Y. B.; Robinson, D. M.; Smith, P. F.; Hadermann, J.; Abakumov, A.; Greenblatt, M.; Dismukes, G. C. *Angew. Chem. Int. Ed.* **2012**, *51*, 1616–1619.
(27) Smith, P. F.; Kaplan, C.; Sheats, J. E.; Robinson, D. M.; McCool, N. S.; Mezle, N.; Dismukes, G. C. *Inorg. Chem.* **2014**, *53*, 2113–2121.
(28) Lugmair, C. G.; Tilley, T. D.; Rheingold, A. L. *Chem. Mater.* **1997**, *9*, 339–348.
(29) Terry, K. W.; Lugmair, C. G.; Tilley, T. D. *J. Am. Chem. Soc.* **1997**, *119*, 9745–9756.
(30) Lugmair, C. G.; Tilley, T. D. *Inorg. Chem.* **1998**, *37*, 6304–6307.
(31) Lugmair, C. G.; Tilley, T. D.; Rheingold, A. L. *Chem. Mater.* **1999**, *11*, 1615–1620.
(32) Kriesel, J. W.; Sander, M. S.; Tilley, T. D. *Adv. Mater.* **2001**, *13*, 331–335.
(33) Kriesel, J. W.; Sander, M. S.; Tilley, T. D. *Chem. Mater.* **2001**, *13*, 3554–3563.
(34) Fujdala, K. L.; Tilley, T. D. *J. Catal.* **2003**, *218*, 123–134.

(35) Fujdala, K. L.; Oliver, A. G.; Hollander, F. J.; Tilley, T. D. *Inorg. Chem.* **2003**, *42*, 1140–1150.
(36) Fujdala, K. L.; Tilley, T. D. *Chem. Mater.* **2004**, *16*, 1035–1047.
(37) Fujdala, K. L.; Brutchey, R. L.; Tilley, T. D. In *Topics in Organometallic Chemistry*; Copéret, C., Chaudret, B., Eds.; Springer-Verlag: Berlin/Heidelberg, 2005; Vol. 16, pp 69–115.
(38) Ahn, H. S.; Tilley, T. D. *Adv. Funct. Mater.* **2012**, *23*, 227–233.
(39) Murugavel, R.; Sathiyendiran, M.; Walawalkar, M. G. *Inorg. Chem.* **2001**, *40*, 427–434.
(40) Sathiyendiran, M.; Murugavel, R. *Inorg. Chem.* **2002**, *41*, 6404–6411.
(41) Pothiraja, R.; Sathiyendiran, M.; Butcher, R. J.; Murugavel, R. *Inorg. Chem.* **2004**, *43*, 7585–7587.
(42) Murugavel, R.; Choudhury, A.; Walawalkar, M. G.; Pothiraja, R.; Rao, C. N. R. *Chem. Rev.* **2008**, *108*, 3549–3655.
(43) Murugavel, R.; Kuppuswamy, S.; Gogoi, N.; Boomishankar, R.; Steiner, A. *Chem. Eur. J.* **2010**, *16*, 994–1009.
(44) Meyer, F.; Hempelmann, R.; Mathur, S.; Veith, M. *J. Mater. Chem.* **1999**, *9*, 1755–1763.
(45) Kumara Swamy, K. C.; Veith, M.; Huch, V.; Mathur, S. *Inorg. Chem.* **2003**, *42*, 5837–5843.
(46) Coles, M. P.; Lugmair, C. G.; Terry, K. W.; Tilley, T. D. *Chem. Mater.* **2000**, *12*, 122–131.
(47) Brutchey, R. L.; Mork, B. V.; Sirbuly, D. J.; Yang, P.; Tilley, T. D. *J. Molec. Catal. A: Chem.* **2005**, *238*, 1–12.
(48) Brutchey, R. L.; Ruddy, D. A.; Andersen, L. K.; Tilley, T. D. *Langmuir* **2005**, *21*, 9576–9583.
(49) Ruddy, D. A.; Tilley, T. D. *Chem. Commun.* **2007**, 3350–3352.
(50) Raboin, L.; Yano, J.; Tilley, T. D. *J. Catal.* **2012**, *285*, 168–176.
(51) Cooper, S. R.; Calvin, M. *J. Am. Chem. Soc.* **1977**, *99*, 6623–6630.
(52) Zwierzak, A.; Kluba, M. *Tetrahedron* **1971**, *27*, 3163–3170.
(53) Chakov, N. E.; Abboud, K. A.; Zakharov, L. N.; Rheingold, A. L.; Hendrickson, D. N.; Christou, G. *Polyhedron* **2003**, *22*, 1759–1763.
(54) Wu, J.-Z.; Sellitto, E.; Yap, G. P. A.; Sheats, J.; Dismukes, G. C. *Inorg. Chem.* **2004**, *43*, 5795–5797.
(55) Vincent, J. B.; Christmas, C.; Chang, H. R.; Li, Q. *J. Am. Chem. Soc.* **1989**, *111*, 2086–2097.
(56) Kanady, J. S.; Mendoza-Cortes, J. L.; Tsui, E. Y.; Nielsen, R. J.; Goddard, W. A., III; Agapie, T. *J. Am. Chem. Soc.* **2013**, *135*, 1073–1082.
(57) Addison, A. W.; Rao, T. N.; Reedijk, J.; van Rijn, J.; Verschoor, G. C. *J. Chem. Soc., Dalton Trans.* **1984**, 1349–1356.
(58) Kulawiec, R. J.; Crabtree, R. H.; Brudvig, G. W. *Inorg. Chem.* **1988**, *27*, 1309–1311.
(59) Vincent, J. B.; Christou, G. *Inorg. Chim. Acta* **1987**, *136*, L41–L43.

(60) Christou, G.; Vincent, J. B. *Biochim. Biophys. Acta* **1987**, *895*, 259–274.
(61) Yachandra, V. K.; Sauer, K.; Klein, M. P. *Chem. Rev.* **1996**, *96*, 2927–2950.
(62) Mukhopadhyay, S.; Mandal, S. K.; Bhaduri, S.; Armstrong, W. H. *Chem. Rev.* **2004**, *104*, 3981–4026.
(63) Dau, H.; Limberg, C.; Reier, T.; Risch, M.; Roggan, S.; Strasser, P. *ChemCatChem* **2010**, *2*, 724–761.
(64) Glaum, R.; Thauern, H.; Schmidt, A.; Gerk, M. *Z. Anorg. Allg. Chem.* **2002**, *628*, 2800–2808.
(65) Stefanidis, T.; Nord, A. G. *Acta Crystallogr., Sect. C: Cryst. Struct. Commun.* **1984**, *40*, 1995–1999.
(66) Terry, K. W.; Tilley, T. D. *Chem. Mater.* **1991**, *3*, 1001–1003.
(67) Kanady, J. S.; Tran, R.; Stull, J. A.; Lu, L.; Stich, T. A.; Day, M. W.; Yano, J.; Britt, R. D.; Agapie, T. *Chem. Sci.* **2013**, *4*, 3986–3996.
(68) Manev, V.; Ilchev, N.; Nassalevska, A. *J. Power Sources* **1989**, *25*, 167–175.
(69) Modro, T.; Sokolowski, J. *Zesz. Nauk. Wyzsz. Szk. Pedagog. Gdansku: Mat., Fiz., Chem.* **1965**, *5*, 77–80.
(70) Oszlányi, G.; Sütő, A. *Acta Crystallogr., Sect. A: Found. Crystallogr.* **2004**, *60*, 134–141.
(71) Palatinus, L.; Chapuis, G. *J. Appl. Crystallogr.* **2007**, *40*, 786–790.
(72) Sheldrick, G. M. *Acta Crystallogr., Sect. A: Found. Crystallogr.* **2007**, *64*, 112–122.

Chapter 2

Insights on the Electronic Structure of the Oxygen-Evolving Complex of Photosystem II Through Spectroscopic Studies of Tetranuclear Manganese-Oxo Clusters[1]

2.1 Introduction

The oxidation of water to dioxygen is one of the most energetically demanding reactions in nature. This reaction is elegantly performed by the photosystem II (PSII) reaction center. PSII is a multi-subunit protein complex in the thylakoid membranes and contains the oxygen-evolving complex (OEC), nature's water oxidation catalyst. Recent X-ray crystal structures[2,3] of PSII have revealed the structure of the OEC, including its Mn_4CaO_x active site (Figure 1). In the active site, three manganese ions, a calcium ion, and four oxide ions are arranged in a distorted cube. A fourth "dangler" manganese ion is linked to the distorted cube through an additional μ-oxo bridge.

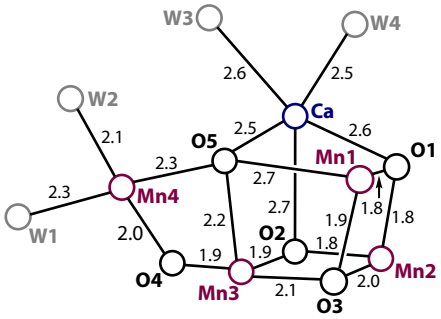

Figure 1. The structure of the Mn_4CaO_x cluster in the oxygen-evolving complex of photosystem II, as observed in the 1.95 Å resolution X-ray crystal structure. Water ligands are shown as W1, W2, etc. Adapted from Shen and co-workers.[3]

The OEC has been studied intensively for over 30 years,[4-14] with one key motivation being the potential relevance of design principles observed in PSII to systems for artificial photosynthesis, in which sunlight is used to convert abundant materials (water and carbon dioxide) to fuel. A key advance in understanding of the OEC was the identification of the S-state or Kok cycle,[15] wherein the OEC was observed to cycle through five distinct oxidation states. These states are labeled S_n, where n represents the relative oxidation state of the overall cluster, beginning with S_0 (Figure 2). The states were identified by observing that illumination of PSII with a series of short flashes of visible light produces oxygen periodically, with a maximum on every fourth flash. This is consistent with the four electrons that must be removed from two water molecules to produce dioxygen, and thus indicates that each flash, on average, advances the OEC one step through the S-state cycle ($S_0 \rightarrow S_1$, $S_1 \rightarrow S_2$, $S_2 \rightarrow S_3$, $S_3 \rightarrow S_4$). These experiments also demonstrated that the dark-stable state is S_1.[15] The Mn oxidation states corresponding to individual S states were later identified, allowing broad consensus on an assignment of S_2 as $Mn(III)Mn(IV)_3$.[16] Note that some authors support an alternate assignment of S_2 as $Mn(III)_3Mn(IV)$, which is also consistent with a number of experiments.[11,17,18]

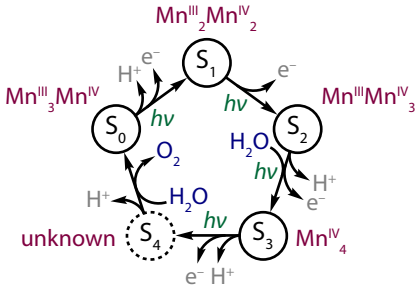

Figure 2. The Kok S-state cycle of the OEC of PSII, depicting the oxidation states of the S_0–S_3 intermediates in the water oxidation reaction.

Investigations of the OEC of PSII have produced key hypotheses that help to explain its high activity (up to 100–400 turnovers per second).[19] These include cooperative action of the manganese centers in storing redox equivalents and aligning oxygen intermediates, including their spins;[9,10,20-22] flexibility of the oxo-bridged Mn_4CaO_x cluster including open and closed geometries;[23,24] mobility of water and oxo ligands;[25,26] controlled activation of substrate water molecules; proton-coupled electron transfer from the complex;[27,28] and the presence of a redox-inactive, electropositive metal ion, Ca^{2+}, without which the complex does not function.[18,29,30] In these hypotheses, the electronic structure of the OEC is often integral to the proposal yet significantly ambiguous in light of experimental evidence. Model complexes for the OEC have therefore been pursued, in order to complement and extend direct studies of PSII.

The striking properties and singular success of the OEC have inspired extensive efforts to construct molecular model complexes. A number of excellent reviews of these efforts have been published,[31-43] of which some[33,37-42] specifically emphasize functional models of the OEC, i.e. water oxidation catalysts. Since the electronic structure of the OEC is of prime importance in understanding and reproducing its function, magnetic studies of model complexes that provide insight to interpretation of the OEC's characteristics are particularly useful. Such results have been reported for mononuclear,[44] dinuclear,[45-61] trinuclear,[62,63] and tetranuclear[64-68] manganese clusters. These studies have revealed that small changes in Mn coordination geometry, bridging ligand properties, and spatial arrangement of interacting paramagnetic centers can drastically alter the magnetic and spectroscopic properties of model complexes. This is one reason that model complexes having structures very similar to that of the OEC of PSII are particularly valuable; they may be used deduce subtle structure-function relationships in the quest to understand and mimic PSII.

Because of the evidence that the OEC's Mn centers act cooperatively to store redox equivalents, align spins, and support reactive intermediates, molecular models with four manganese sites and/or those that closely reproduce the Mn_3CaO_x structure are of special importance. In 1997, Dismukes and co-workers reported $Mn_4O_4(O_2PPh_2)_6$, an $Mn_4(\mu_3\text{-}O)_4$ "cubane" complex in which Mn and oxo centers alternate at the corners of a cube. The core oxo ligands of this complex generate dioxygen upon irradiation[69] and water upon treatment

with an H-atom donor,[70] which together comprise a partially realized water oxidation cycle. This complex and its derivatives were studied thoroughly[19,71] and were the model that led to the discovery of complexes **1**-**3** in Chapter 1. Photochemical water oxidation catalysis by another Mn_4O_4 cubane complex, $(n\text{Bu}_4\text{N})_3[Mn_4V_4O_{17}(OAc)_3]\cdot 3H_2O$, was recently reported, although decomposition was observed under some of the relevant conditions.[68] Since the first report of a Mn_4O_4 cubane complex by Dismukes, a number of clusters have appeared that contain both Mn and Ca in arrangements increasingly similar to that of the OEC.[63,67,72] Perhaps the richest set of studies performed in this area are those by Agapie and co-workers using the deprotonated 1,3,5-tris(2-di(2'-pyridyl)hydroxymethylphenyl)benzene ligand, which was used to prepare Mn_3MO_x clusters, where M = Mn, Ca, Sr, Sc, Zn, or Y.[66,72-75] Among these studies, a magnetostructural characterization[66] of a set of tetranuclear Mn clusters is particularly relevant to the PSII OEC. These complexes range in oxidation state from $Mn(II)_3Mn(III)$ to $Mn(III)_2Mn(IV)_2$ and exhibit varied susceptibility and electron paramagnetic resonance (EPR) properties. These results offer numerous comparisons for the work described in this chapter.

Chapter 1 described three tetranuclear manganese clusters studied in pursuit of inorganic materials containing discrete Mn_4O_4 units. In the current study, we report structural and spectroscopic properties of these clusters that are highly relevant to magnetic investigations of the OEC S-state intermediates. The first complex, $Mn_4O_4[O_2P(O\text{t}\text{Bu})_2]_6$ (**1**), combines an $Mn_4(\mu_3\text{-}O)_4$ core like that synthesized by Dismukes and co-workers[76,77] with the thermolytically labile ligand $O_2P(O\text{t}\text{Bu})_2$.[78-86] The second complex was generated serendipitously in an attempt to produce a cubane complex similar to **1** ligated by cyclic pinacol phosphate $O_2PO_2C_2Me_4$ ($O_2P(pin)$). This complex, $Mn_4O_2[O_2P(pin)]_6(bpy)_2$ (**2**), does not possess an $Mn_4(\mu_3\text{-}O)_4$ core but instead has an $Mn(\mu_3\text{-}O)Mn_2(\mu_3\text{-}O)Mn$ butterfly structure. The third complex, $Mn_4O_2[O_2P(O\text{t}\text{Bu})_2]_6(OPEt_3)_2$ (**3**), was generated by reversible reaction of complex **1** with an oxygen-atom acceptor, triethylphosphine, and also possesses an $Mn(\mu_3\text{-}O)Mn_2(\mu_3\text{-}O)Mn$ butterfly structure. The interconversion of complexes **1** and **3**, including spectroscopic comparison of the two, is relevant to current proposals[25,26] for structural rearrangement in the PSII OEC during operation. Our previous study (Chapter 1) revealed no EPR signals for complex **1** in preliminary investigations, which was thought to be consistent with the absence of observable transitions for $Mn_4O_4(O_2PPh_2)_6$,[76] However, herein we report that at low temperature and sufficient sensitivity, complexes **1**-**3** exhibit both perpendicular-mode and parallel-mode signals that correspond to half-integer and integer spin states of the complexes, respectively.

The information available on Mn_4O_x clusters and the PSII OEC from molecular models remains far from complete. Indeed, recent reports highlight the nuanced relationship between remaining questions about the OEC's activity and its experimental magnetic observables.[25,87] In this study, we describe the bulk magnetism and EPR spectra of complexes **1**-**3** in detail, with the goal of illuminating electronic structure-function relationships relevant to the OEC and the broader goal of artificial photosynthesis.

2.2 Results and Discussion

2.2.1 X-ray crystal structures

The structures of complexes **1**-**3** (Figure 3), as determined by X-ray crystallography at 100 K (see Chapter 1), offer initial insight to the analysis of their electronic and magnetic properties. $Mn_4O_4[O_2P(O\textit{t}Bu)_2]_6$ (**1**) contains four manganese centers bridged by four μ_3-O ligands in a cube of approximate T_d symmetry, similar to that previously reported for $Mn_4O_4[O_2PPh_2]_6$.[76] In both $Mn_4O_4[O_2PPh_2]_6$ and complex **1**, each of the six Mn_2O_2 faces of the cube is coordinated by a bridging ligand – diphenylphosphinate in the former case and di-*tert*-butylphosphate in the latter. Note that two independent molecules of **1** that crystallized in the asymmetric unit possess similar structures. The average bond distances described in the text include both molecules. Complex **1** exhibits crystallographically distinct Mn(III) and Mn(IV) sites. The Mn(III) sites are identified by a wider distribution of Mn–O_{oxo} bond distances with an average of 2.01 ± 0.15 Å, while the Mn(IV) sites have shorter and more uniform Mn–O_{oxo} distances (av 1.88 ± 0.04 Å). These Mn–O_{oxo} distances are similar to those observed in the 1.9 Å resolution crystal structure of the Photosystem II OEC (1.8–2.7 Å).[3] The Mn···Mn distances are consistent with the oxidation state assignments determined by Mn–O_{oxo} distance inspection. The Mn(III)···Mn(III) distances are the longest (av 3.04 ± 0.03 Å), and the Mn(IV)···Mn(IV) pairs the shortest (av 2.84 ± 0.04 Å). The Mn(III)···Mn(IV) pairs are somewhat bifurcated, with each cube containing two short distances (av 2.83 ± 0.02 Å) and two long distances (av 2.97 ± 0.03 Å), for an overall Mn(III)···Mn(IV) average of 2.90 ± 0.08 Å. Like the Mn–O distances, the Mn···Mn distances of complex **1** are similar to those in the cubane core of the OEC, which are in the range 2.7–3.2 Å.[3]

Butterfly complexes $Mn_4(\mu_3\text{-}O)_2[O_2P(pin)]_6(bpy)_2$ (**2**) and $Mn_4(\mu_3\text{-}O)_2[O_2P(O\textit{t}Bu)_2]_6(OPEt_3)_2$ (**3**) have similar $Mn(\mu_3\text{-}O)Mn_2(\mu_3\text{-}O)Mn$ cores (Figure 3). In each, an inner Mn_2O_2 diamond is flanked by two outer Mn centers. Two μ_3-O ligands bridge the inner and outer Mn centers. Six phosphate ligands bridge the Mn_{inner}-Mn_{outer} pairs in an alternating 2-1-2-1 pattern that produces approximate C_2 symmetry in complex **2** and crystallographically imposed C_i symmetry in complex **3**. While sharing similar core structures, complexes **2** and **3** differ in their terminal ligands, coordination numbers and geometries, and Mn···Mn distances.

In complex **2,** the inner Mn centers are five-coordinate with distorted square pyramidal geometries (O_{apical}-Mn-O_{basal} angles ranging from 90.1(1)° to 111.4(1)°), and the outer two Mn centers are six-coordinate with terminal 2,2'-bipyridine ligands and pseudo-octahedral geometry. Oxidation state assignments were made on the basis of Mn–O bond distances. Shorter Mn–O_{oxo} (av 1.80 ± 0.05 Å) and Mn–$O_{phosphate}$ (av 1.98 ± 0.11 Å) distances for the inner sites indicate Mn(III), whereas longer Mn–O_{oxo} (av 2.01 ± 0.03 Å) and Mn–$O_{phosphate}$ (av 2.15 ± 0.02 Å) distances for the outer sites are consistent with Mn(II). The end-to-end Mn(II)···Mn(II) pair is separated by 6.154(1) Å and the inner Mn(III)···Mn(III) pair by 2.7770(9) Å. Two short Mn(II)···Mn(III) pairs (3.2762(8) Å, 3.3081(8) Å) and two long

Mn(II)···Mn(III) pairs (3.5586(8) Å, 3.6122(9) Å) are observed, with an overall average of 3.44 ± 0.17 Å. The Mn–O and Mn···Mn distances (except the Mn(II)···Mn(II) distance) observed for complex **2** are in the same range as those in the OEC (1.8–2.7 Å for Mn–O and 2.7–5.2 Å for Mn···Mn).[3]

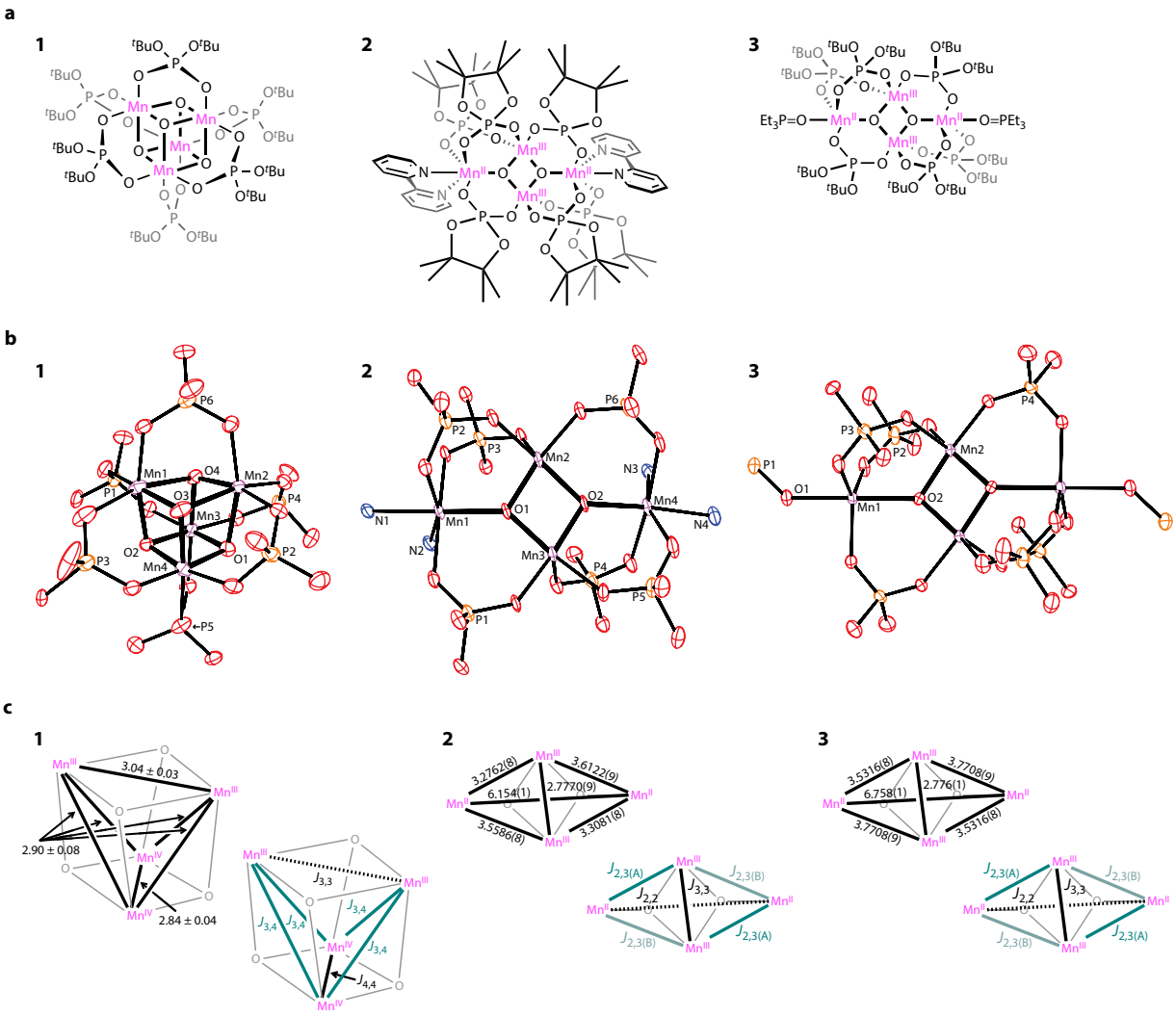

Figure 3. Structures of complexes **1**-**3**: (a) Structural drawings. (b) Crystal structures with thermal ellipsoids set at 50%. Carbon and hydrogen atoms are omitted for clarity. For complex **1**, two independent molecules in the asymmetric unit have similar structures; one is shown. Distances described in the text and in part c include both molecules. (c) Mn···Mn distances (Å) with esd's and proposed coupling schemes for the paramagnetic centers.

Complex **3**, which has terminal $OPEt_3$ ligands in place of the bipyridines in complex **2**, has five-coordinate outer Mn(II) centers in a trigonal bipyramidal ligand field. The inner five-coordinate Mn(III) sites have a geometry that is intermediate between square pyramidal

and trigonal bipyramidal (see Chapter 1). As with complex **2**, shorter Mn–O_{oxo} (av 1.85 ± 0.01 Å) and Mn–$O_{phosphate}$ (av 2.03 ± 0.06 Å) distances identify the inner Mn(III) sites, while the outer Mn(II) sites exhibit longer Mn–O_{oxo} (2.179(2) Å) and Mn–$O_{phosphate}$ (av 2.06 ± 0.01 Å) distances. While the arrangement of Mn centers in complexes **2** and **3** is quite similar, Mn···Mn distances in complex **3** are longer in general, most noticeably between the outer Mn(II) centers (distance 6.758(1) Å). The Mn(III)···Mn(III) distance, however, is nearly identical in the two complexes (2.776(1) Å for complex **3**). The Mn(II)···Mn(III) contacts again fall into short (3.5316(8) Å) and long (3.7708(9) Å) groups.

2.2.2 Magnetic susceptibility

Magnetic susceptibility measurements were performed on powdered crystalline samples of complexes **1**-**3** using a superconducting quantum interference device (SQUID) magnetometer. As the temperature is decreased over the 2–300 K range, the observed $\chi_M T$ value for each complex decreases, yielding values substantially lower than those predicted by the spin-only formula (Figure 4). These observations are consistent with prevailing antiferromagnetic couplings between the Mn ions in complexes **1**-**3**. For complex **1**, which has an $Mn(III)_2Mn(IV)_2$ core, the spin-only formula predicts χT = 9.75 cm^3 K mol^{-1} for uncoupled Mn centers or χT = 28.0 cm^3 K mol^{-1} for ferromagnetically coupled centers (S_T = 7). Complex **1** experimentally exhibits much lower values of χT = 0.23 cm^3 K mol^{-1} at 10 K and 6.7 cm^3 K mol^{-1} at 300 K, with a nearly linear dependence of χT on T between these temperatures. For complexes **2** and **3**, both $Mn(II)_2Mn(III)_2$ butterfly structures, the formula predicts χT = 14.75 cm^3 K mol^{-1} (uncoupled) or χT = 45.0 cm^3 K mol^{-1} (ferromagnetically coupled, S_T = 9). Experimentally, complex **2** exhibits χT = 4.5 cm^3 K mol^{-1} at 10 K and 15.3 cm^3 K mol^{-1} at 300 K, and complex **3** χT = 2.9 cm^3 K mol^{-1} at 10 K and 9.4 cm^3 K mol^{-1} at 300 K. Both of these complexes exhibit linear regions in χT vs. T: approximately 50–300 K for complex **2** and 100–300 K, with a smaller slope, for complex **3**. At lower temperatures, the susceptibilities for both complexes drop sharply, approaching values in the χT = 0–1 cm^3 K mol^{-1} range. The greater susceptibility for **2** than **3** observed at all temperatures is somewhat surprising under an assumption of antiferromagnetic couplings; the shorter Mn···Mn distances observed for **2** vs. **3** would suggest stronger antiferromagnetic coupling in **2** and a correspondingly lower susceptibility. The more nuanced treatment allowed by numerical fitting of the susceptibility results (*vide infra*) provides a possible explanation for this apparent contradiction.

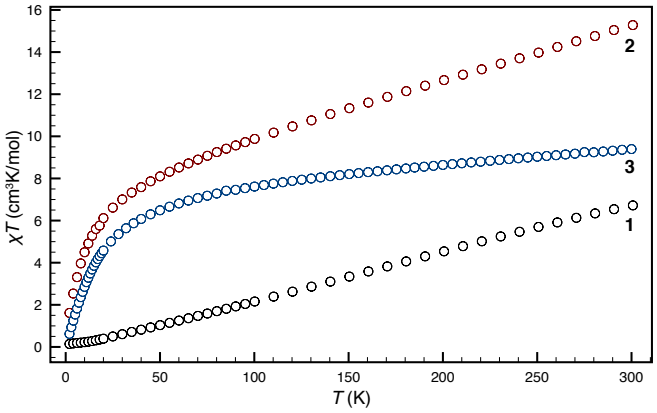

Figure 4. Molar magnetic susceptibility (χT vs. T) data for complexes **1**-**3**, collected at H = 1000 Oe.

The magnetic susceptibilities observed for the three complexes are similar to those reported by Agapie, Britt, and co-workers for similar Mn tetramers. The nearly linear dependence of χT on T for complex **1** is similar to that of complex **6** in their 2013 paper, with which it shares an $Mn(III)_2Mn(IV)_2$ assignment.[66] Complex **1** has slightly higher χT at 300 K and somewhat lower χT in the low-temperature limit, compared to the reference complex. Complexes **2** and **3** exhibit χT vs. T behavior similar to that of Agapie's complex **4**. All three complexes have $Mn(II)_2Mn(III)_2$ structures, but it is important to note that the geometry of the Agapie complex is quite different, with a single μ_4-oxo bridging all four centers (a second μ_2-oxo bridges an Mn(II)···Mn(III) pair) and much closer contact between the Mn(II) sites.[66] While the same pattern of a linear region in χT above T ~ 50–100 K and a sharp drop in χT at lower temperatures is observed, the slope and curvature of the observed traces reveal subtle differences that were investigated by development of an exchange coupling model.

Detailed analysis of exchange-coupling models for complexes **1**-**3** was performed by fitting the experimental susceptibility data with an isotropic spin Hamiltonian (eq 1). Magnetic coupling schemes (Figure 3c) were developed by inspection of the Mn···Mn distances described above. For complex **1**, a three-constant scheme includes $J_{3,3}$ for the Mn(III)···Mn(III) pair, $J_{3,4}$ for all four Mn(III)···Mn(IV) pairs, and $J_{4,4}$ for the Mn(IV)···Mn(IV) pair. Similarly, a three-constant coupling scheme for butterfly complexes **2** and **3** includes $J_{2,2}$ for the Mn(II)···Mn(II) pair, $J_{2,3}$ for all four Mn(II)···Mn(III) pairs, and $J_{3,3}$ for the Mn(III)···Mn(III) pair. Since the Mn(II)···Mn(II) and Mn(II)···Mn(III) distances are longer in complex **3** than in **2**, the $J_{2,2}$ and $J_{2,3}$ values might be expected to be smaller in magnitude. The nearly identical Mn(III)···Mn(III) distances in complexes **2** and **3** suggest that $J_{3,3}$ would be similar for the two. Further details on the fitting procedure are provided in the experimental section.

$$\widehat{H} = -2\sum_{ij} J_{ij}\,\widehat{\boldsymbol{S}}_i\widehat{\boldsymbol{S}}_j \qquad (1)$$

The results of fitting exchange coupling constants to the experimental data are displayed in Table 2. The three-parameter fits for complexes **1** and **3** reveal primarily antiferromagnetic (negative) exchange couplings between the manganese ions. For complex **1**, the Mn(III)Mn(III) and Mn(IV)-Mn(IV) couplings were stronger than the Mn(III)-Mn(IV) couplings, though all were antiferromagnetic (negative). For this complex and the others, spin frustration, where satisfaction of all antiferromagnetic couplings is impossible and smaller exchange couplings will be "frustrated", is relevant. Complex **3** exhibits a strong antiferromagnetic coupling between its Mn(II) sites and relatively weak Mn(II)-Mn(III) and Mn(III)-Mn(III) couplings. Complex **2** presented less clear results; particularly the optimized $J_{2,2}$ value of 315 cm^{-1}, which is unlikely to be physical. Analysis of this result showed that the outer Mn(II) centers do appear to couple ferromagnetically, but that the quality of the fit does not depend strongly on the magnitude of the coupling; the residual, R (see experimental section), changes by ~ 1% if J_{22} = 50 cm^{-1} is used (R = 3.99 x 10^{-3}) instead of the optimized value, J_{22} = 315 cm^{-1} (R = 3.95 x 10^{-3}). This observation does help to explain the higher observed susceptibility for complex **2** vs. complex **3**, which has shorter Mn···Mn distances and would be expected to have couplings of larger magnitude, particularly those involving the outer Mn(II) sites. In fact, $J_{2,3}$ is stronger in magnitude, but ferromagnetic, in **2** than in **3**, providing an explanation for **2**'s greater susceptibility. Each of the fits contains larger exchange coupling constants than those reported for the analogous complexes studied by Agapie and Britt.[66] The optimized parameters in Table 2 also differ from those in the Agapie paper in their fit quality. Residuals in Table 2 are near 4 x 10^{-3}, approximately 100 times the values they report. A possible explanation for the discrepancy is that the Agapie fits allowed g to vary, while those in Table 2 did not. However, including g in fitting for complexes **1** and **2** did not dramatically improve experimental agreement, but did produce g values that were at odds with those observed by EPR spectroscopy (*vide infra*). Allowing g to vary for complex **3** *did* improve fit quality, resulting in the optimized parameters $J_{2,2}$ = -53.1 cm^{-1}, $J_{2,3}$ = 7.60 cm^{-1}, $J_{3,3}$ = 1.11 cm^{-1}, g = 2.06, and R = 3.04 x 10^{-5}. More detailed fitting efforts are currently being undertaken to explain these results.

Table 1. Fitting results for complexes **1**-**3**.

Complex:	**1** (n = 3, m = 4)	**2** (n = 2, m = 3)	**3** (n = 2, m = 3)
$J_{n,n}$ (cm^{-1})	-24.5	315	-38.3
$J_{n,m}$ (cm^{-1})	-10.6	-4.81	7.00
$J_{m,m}$ (cm^{-1})	-46.7	-9.24	-1.03
R (x 10^{-3})	4.0	4.0	0.13

2.2.3 Electron paramagnetic resonance

Continuous-wave (*cw*) EPR studies were performed on complexes **1**-**3** at X band frequencies (ν ~ 9.64 GHz for perpendicular mode and 9.40 GHz for parallel mode) using a dual-mode resonance cavity. Complexes **1** and **3** were studied in frozen toluene solutions; complex **2** was frozen in tetrahydrofuran solution. In all cases, peaks appearing at 10 K

decreased in intensity and no new peaks were observed with increasing temperature. Unless otherwise stated, the field positions of the peaks and other characteristics refer to the spectra acquired at 10 K.

The tetramanganese cubane complex **1** displays a broad multiline signal in its perpendicular-mode EPR spectra (Figure 5a), centered at g = 2, spanning the field range of 2500–4200 G. Over 35 lines are observed, with a strong central feature in the range 2900–3800 G, surrounded by two weaker side features at g = 1.7 and 2.5. These outer features have effective hyperfine couplings of 40–48 G, while the spacings are narrower in the strong central peaks at 20–35 G. The central signal contains a sharp set of lines that could be assigned as a separate Mn(II) six-line signal, apparently from an impurity. However, the persistence of these sharp peaks in a reproducible intensity ratio to other peaks, throughout multiple independently prepared samples, suggests the signals are endogenous. Overall, complex **1**'s perpendicular-mode signal, spanning over 1000 G with a large number of hyperfine features, is consistent with the four Mn centers in close contact observed in its crystal structure. The magnetic susceptibility value for **1** at 10 K (χT = 0.23 cm^3 K mol^{-1}) best agrees with an S = 0 state, assuming an integer spin. The results of numerical susceptibility fitting for **1** agree, indicating an S = 0 ground state with the lowest-lying excited state, an S = 1 state, lying at E_{rel} = 49.0 cm^{-1}. An S = 2 state is not reached until E_{rel} = 121 cm^{-1} above the ground state. Note: these energies do not consider zero-field splitting and assume an isotropic g-factor of 2.0. The observed g = 2 EPR signal is therefore expected to result from the S = 1 state and low zero-field splitting, with electron-nuclear couplings to four ^{55}Mn (I = $^5/_2$) centers. The multiline spectrum observed for this complex is similar to the g = 2 signals of the S_0 and S_2 states of the OEC of PSII, which have Mn oxidation states of $Mn(III)_3Mn(IV)$ and $Mn(III)Mn(IV)_3$, respectively.[88] A singly oxidized form of complex **1** would share an $Mn(III)Mn(IV)_3$ assignment with the S_2 state of the OEC and thus yield a half-integer spin signal. If present, the $\mathbf{1}^+$ species might be unstable, as complex **1** was previously found to lack any reversible oxidation wave by cyclic voltammetry (see Chapter 1).

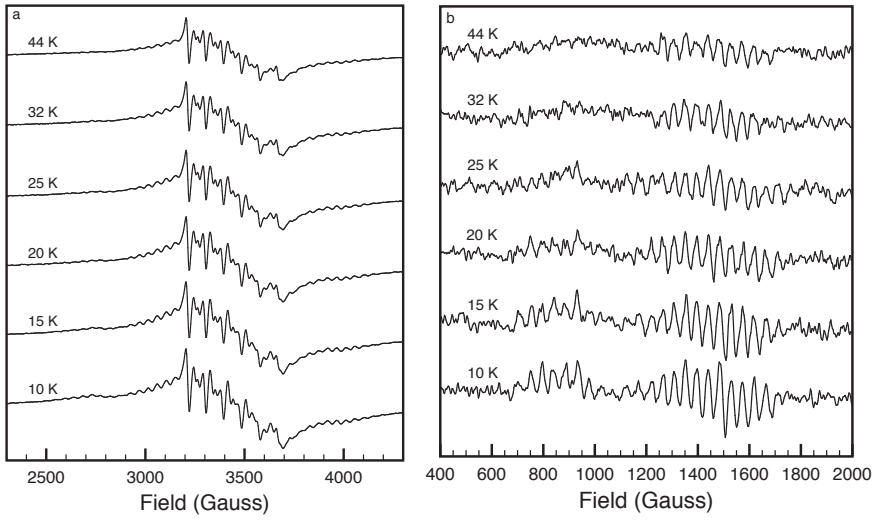

Figure 5. Perpendicular-mode (a) and parallel-mode (b) EPR spectra of complex **1** at T = 10–44 K. Experimental parameters: microwave frequency = 9.64 GHz (perpendicular), 9.40 GHz (parallel); power = 2.4 mW (perpendicular), 7.5 mW (parallel); modulation amplitude = 4 G; modulation frequency = 100 kHz.

Parallel-mode spectroscopy on complex **1** (Figure 5b) reveals two signals at low field – a fifteen-line signal at g = 4.6 and a nine-line signal at g = 7.5. These features may be part of a single 24-line signal centered at g = 5.4, but the greater decline in intensity with increasing T for the lower-field signal vs. the higher-field signal suggests they are independent. The effective hyperfine splittings are on the order of 40–50 G throughout both signals. As described above, the magnetic susceptibility data suggests an S = 0 ground state for complex **1**, implying that the parallel-mode EPR signals in Figure 5b represent population of low-lying integer spin excited states having electron-nuclear hyperfine interactions with multiple ^{55}Mn (I = $^5/_2$) centers. Indeed, the lowest-lying excited state for complex **1** predicted by the outcome of susceptibility fits, an S = 1 state at E_{rel} = 49.0 cm^{-1}, should be amply populated to allow detection. The Boltzmann factor at 10 K for an energy spacing of 49.0 cm^{-1} is $N_{S=1}/N_{S=0}$ = 8.65 x 10^{-4}, which predicts a total number of excited-state spins $N_{S=1}$ ~ 5 x 10^{-13} (assuming a 100 μL, 1 mM sample) that is several orders of magnitude greater than the approximate detection limit, N_{min} ~ 10^{10}–10^{11} spins, of a typical X-band spectrometer with microwave power = 7.5 mW.[89] As with the perpendicular-mode signal, this spectrum exhibits features similar to those of the OEC. The parallel-mode spectrum of **1** resembles the OEC's S_1 state, which shares an $Mn(III)_2Mn(IV)_2$ assignment with **1**.[88] Both species have multiline features at low field. However, while the S_1 state's signal is centered at g = 12 and spans a 500–600 G range, complex **1** exhibits features spanning 1200–1300 G centered at g = 4.6 and 7.5. A simulated spectrum having S = 1, D = 0.33–0.67 cm^{-1}, and E/D = 0.2 reproduces the location of the parallel-mode feature(s) in Figure 5b. Higher spin states did not give immediate agreement. Previously published simulations of the PSII S_1 state were inconclusive as to the spin state, with reasonable agreement obtained for S ranging from 1 to

4.[88,90] Finally, a weak signal (not shown) appearing at g = 2 in the spectrum likely results from leakage of perpendicular-mode signals.

Complexes **2** and **3**, while sharing a similar Mn_4O_2 butterfly core structure, exhibit remarkably different EPR spectra. The perpendicular-mode spectra of Complex **2** reveal a strong peak at g = 1.95 with Curie behavior (I ~ 1/T) and a weak peak at g ~ 9.5 (Figure 6a). The susceptibility observed for this complex rises steeply over the 2–20 K temperature range. Susceptibility fitting predicts an S = 1 ground state and reveals that this steep rise is likely due to rapid population of low-lying excited states, which include S = 2 states at negligible energy above the ground state, an S = 3 state at E_{rel} = 2.28 cm^{-1}, an S = 4 state at E_{rel} = 23.0 cm^{-1}, and an S = 5 state at E_{rel} = 62.3 cm^{-1}. The EPR peak at g = 1.95 may result from any or all of these states, with good agreement obtained for simulations with small zero-field splitting (*e.g.* D < 0.05 cm^{-1} for S = 1 and D < 0.02 cm^{-1} for S = 5).

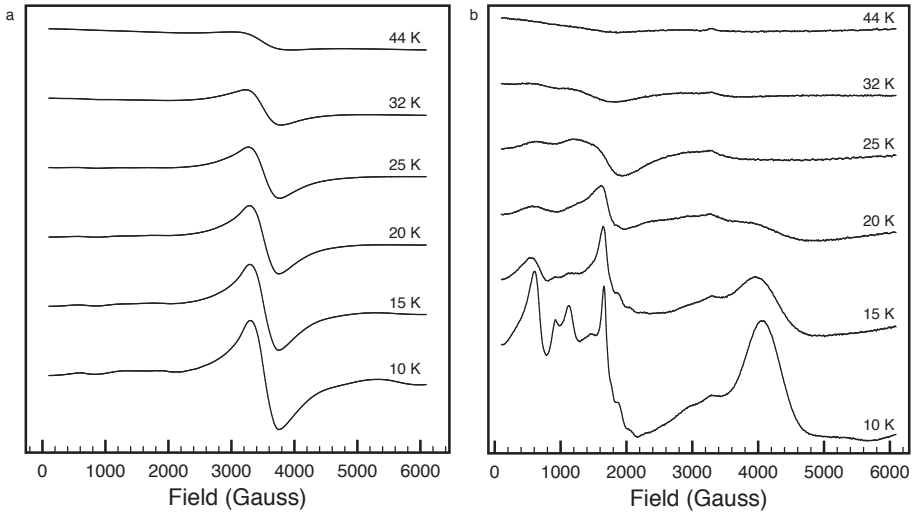

Figure 6. Perpendicular-mode (a) and parallel-mode (b) EPR spectra of complex **2** at T = 10–44 K. Experimental parameters: microwave frequency = 9.64 GHz (perpendicular), 9.39 GHz (parallel); power = 2.4 mW (perpendicular), 7.5 mW (parallel); modulation amplitude = 4 G; modulation frequency = 100 kHz.

In parallel mode, complex **2** exhibits a peak at g = 1.53 and at least six peaks ranging from g = 3.5–9.8 (Figure 6b). These peaks decline rapidly in intensity as temperature is increased beyond 10 K. A weak peak near g = 2 appears to result from leakage from perpendicular mode. No hyperfine splitting was observed in the spectra for complex **2**. These results suggest an integer spin system with large S for the ground or low-lying excited states, consistent with the susceptibility results for this complex described above. The parallel-mode spectra could arise from an S = 3, 4, or 5 system with zero-field splitting parameters D ~ 0.035–0.045 cm^{-1} and E/D ~ 0.1.

Complex **3** displays broad peaks with unresolved hyperfine couplings, centered at g = 1.64, 2.15, 2.9, 3.8, 5.3, and 12.2, in its perpendicular-mode spectrum at 10 K (Figure 7a).

With increasing temperature, all of these peaks decrease in intensity, revealing a feature at g = 2.01 whose intensity is much less temperature-dependent. Simulations with peaks spanning the same range as the perpendicular-mode spectra of complex **3** can be generated from spin systems with $S = {}^{3}/_{2}$–$^{9}/_{2}$. This complex exhibits larger zero-field splitting than complex **2**, considering the intensity of low-field peaks.

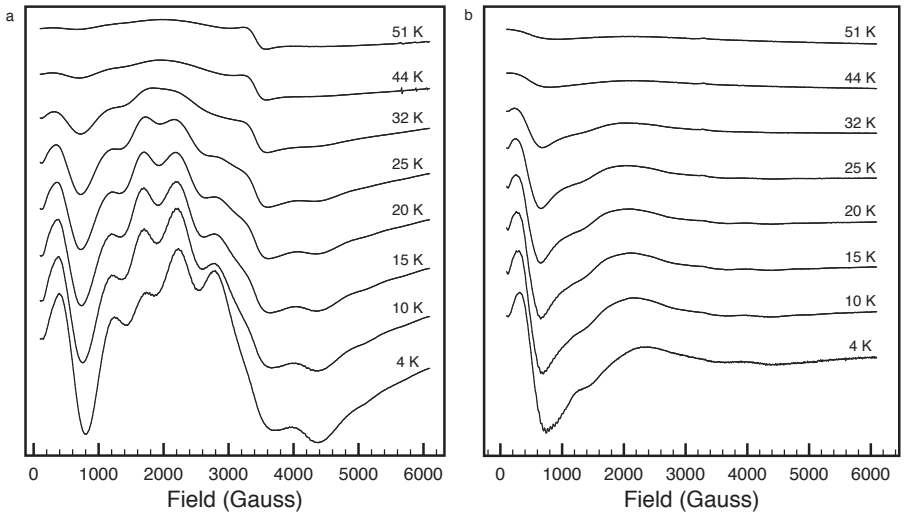

Figure 7. Perpendicular-mode (a) and parallel-mode (b) EPR spectra of complex **3** at T = 4–51 K. Experimental parameters: microwave frequency = 9.64 GHz (perpendicular), 9.40 GHz (parallel); power = 7.5 mW; modulation amplitude = 4 G; modulation frequency = 100 kHz.

In parallel mode, complex **3** displays a strong transition centered at g = 14.1, with partially resolved hyperfine features having 40–48 G separation at 4 K (Figure 7b). A second signal centered at g = 5.4 is much weaker. Reasonable agreement with the observed g = 14.1 signal is obtained for a simulated spectrum with S = 5 and D ~ 0.3 cm^{-1}, approximately ten times the zero-field splitting value observed for complex **2** but still smaller than values reported for the PSII OEC (D = 0.805 for S_1 and 0.455 for S_2).[88,91]

2.2.4 Relevance of complexes 2 and 3 to the OEC S_2 state EPR signals

One of the most interesting problems in studies of the electronic structure of the PSII OEC concerns the multiple perpendicular-mode EPR signals observed for the S_2 state. These signals have been studied for over 35 years.[92-95] They include a multiline signal at g = 2 with at least 18 hyperfine lines and a broad signal at g = 4.1 without visible hyperfine couplings at X-band. These signals have been assigned as resulting from an S = ½ state[96] and the middle Kramer's doublet of an $S = {}^{5}/_{2}$ state (D = 0.455 cm^{-1} and E/D = 0.25),[91,97] respectively. The conditions leading to the appearance of one, the other, or both of the S_2 signals are complex and include temperature variation, infrared illumination, treatment with

alcohols or ammonia, removal or substitution with Sr^{2+} of the Ca^{2+} ion, and ambient concentration of 'activating' (Cl^-, Br^-, I^-, NO_3^-) or 'deactivating' (F^-, N_3^-) ions.[96]

In order to explain the multiple spin states observed for the OEC's S_2 state and their relationship to these factors, several conflicting theories have been proposed. The first is an isostructural, single spin-system model, in which the structure of the OEC remains largely unchanged during a high-to-low spin transition from the $S = {}^5/_2$ state and $g = 4.1$ signal to the $S = ½$ state and multiline $g = 2$ signal (and *vice versa*).[91,97,98] In this model, the two states are hypothesized to have similar energies due to spin frustration, in which complete antiferromagnetic coupling within paramagnetic clusters is not possible.[96] However, the environmental influence of the preparation conditions mentioned above would perturb the energies of the $S = ½$ and ${}^5/_2$ states, favoring observation of one or the other EPR signal. An Mn_2 model complex exhibiting a temperature-dependent interconversion of $g = 2$ and low-field signals was also used to support this model.[99] Note that a single spin *state* model, in which the $g = 2$ signal would arise from the inner Kramer's doublet of the same $S = {}^5/_2$ state whose middle doublet generates the $g = 4.1$ signal,[91] can be excluded based on the observed independence of the two signals' intensities. The second model for the S_2 state's behavior involves structural rearrangement, in which different, interconverting spin systems give rise to the observed EPR signals.[100] The present version of this model was developed from density functional theory (DFT) calculations using the 1.9 Å crystal structure of Photosystem II as a starting point.[101] The key feature of the model is that one of the oxo ligands (O5 using the labeling scheme of Shen and co-workers)[2,3] within the Mn_3CaO_4 cubane core of the OEC migrates toward the dangler Mn center (Figure 8). As it does so, the assignment of the Mn(III) site within the overall Mn(III)$Mn(IV)_3$ S_2 state changes from Mn4, the dangler site, to Mn1, inside the cube. The first of these structures is called 'closed' and the second 'open'. The model predicts that the $S = {}^5/_2$ state and $g = 4.1$ signal arise from the closed structure, while the $S = {}^1/_2$ state and $g = 2$ signal arise from the open structure.[101] This model was further developed to explain the dependence of the signals on preparation conditions by hypothesizing the effects of hydrogen bonding to the dangler water ligands and displacement of O5 by NH_3.[102]

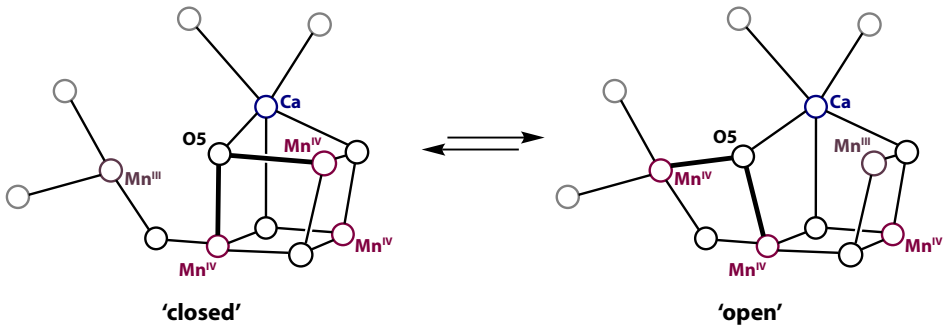

Figure 8. Proposed structural model for the S_2 state of the Photosystem II OEC, in which movement of an oxygen atom between 'closed' and 'open' positions changes the location of the Mn(III) site and induces spectroscopic changes.[101] Manganese contacts to O5 (labeled using the scheme of Shen and co-workers; see Figure 1)[2,3] have been bolded for emphasis.

Comparing the geometric and electronic features of complexes **2** and **3** is relevant to discussion of models for the OEC S_2 state. Both complexes have a $Mn(\mu_3\text{-}O)Mn_2(\mu_3\text{-}O)Mn$ core bridged by six phosphate ligands and capped by two terminal ligands (Figure 3). Within the core, the structural parameters are quite similar (*cf.* the Mn(III)···Mn(III) distances, which differ by 0.001(1) Å) and the main difference is the elongation of the Mn(II)···Mn(II) distance across the complex (*vide supra*). Despite their structural similarities, complexes **2** and **3** exhibit different magnetic susceptibility behavior and strikingly dissimilar perpendicular- and parallel-mode EPR spectra. While the oxidation states of complexes **2** and **3** ($Mn(II)_2Mn(III)_3$) are not represented on the Kok S-cycle, the nuanced electronic effects they exhibit are relevant to other tetranuclear Mn clusters, especially those with varying Mn···Mn distances like the OEC. The results observed for complexes **2** and **3**, which have equivalent Mn valence arrangements and bridging ligands, suggest that the significant structural rearrangement in the second proposal above may not be required to explain the S_2 state EPR signals. Instead, the results suggest small changes to a single S_2 structure could be the source of its two spin states and their associated signals, perhaps through some of the same mechanisms proposed previously for the rearrangement model.[102]

2.3 Conclusions

The tetranuclear complexes **1**-**3** exhibit structural, magnetic, and spectroscopic features highly relevant to those of Photosystem II, while spanning multiple oxidation states reminiscent of the PSII S-cycle. The number of oxo-bridged tetranuclear Mn clusters remains small, but growing, relative to that of dinuclear clusters, making characterization of Mn_4 structures particularly valuable to PSII investigations. Like the OEC of PSII, each of the complexes exhibits a magnetic susceptibility that is substantially lower than that predicted by the spin-only formula. EPR spectroscopy reveals a parallel-mode signal for complex **1** that is very similar to that observed for the S_1 state of the OEC. Complexes **2** and **3**, despite having different oxidation states than those generally accepted to be present in the S-cycle of Photosystem II, are relevant to investigations of PSII EPR spectra, particularly the origin of the $g = 2$ and $g = 4.1$ signals of the S_2 state. Complexes **2** and **3** exhibit dramatic differences in their EPR spectra even though their X-ray crystal structures are quite similar. These results support the conclusion that a single spin system produces the two S_2 EPR signals without requiring rearrangement of bridging ligands or valence states. These investigations highlight the subtle relationship of geometric and electronic structure, in which small changes in environment often dramatically change experimental outcomes.

2.4 Acknowledgements

Lucy Darago and Joe Zadrozny are gratefully acknowledged for performing magnetic susceptibility experiments reported herein. This material is based upon work performed by the Joint Center for Artificial Photosynthesis, a DOE Energy Innovation Hub, supported

through the Office of Science of the U.S. Department of Energy under Award Number DE-SC0004993.

2.5 Experimental Details

General procedures. Complexes **1**-**3** were synthesized as described in Chapter 1. They were handled and stored under an inert atmosphere.

Magnetic susceptibility measurements. Magnetic susceptibility measurements were performed on ground polycrystalline samples in polycarbonate gelcaps and restrained in molten eicosane. Data were collected with a Quantum Design SQUID magnetometer at temperatures from 2 to 300 K and a 1000 Oe magnetic field.

Magnetic susceptibility fits. All susceptibility fitting was performed using the 'curry' function of EasySpin 5.0.20.[103] Note: EasySpin defines the exchange Hamiltonian as $H = +J(S_1 \bullet S_2)$, while the definition used in the text to describe results is $H = -2J(S_1 \bullet S_2)$; values were multiplied or divided by –2, where appropriate, to account for this discrepancy. The *g*-values for all four Mn centers in each complex were held equal. These values were drawn from EPR observations ($g = 2$ for complex **1**, $g = 1.95$ for complexes **2** and **3**) and not varied during susceptibility fitting. A three-parameter coupling scheme (J_{33}, J_{34}, and J_{44} for complex **1**; J_{22}, J_{23}, and J_{33} for complexes **2** and **3**) was used initially. First, a grid-based search of the parameter space in 5 cm^{-1} increments was performed. Results were ranked according to *R*, (which is defined in equation 2. A cutoff in *R* corresponding roughly to ten times the lowest value of *R* obtained in the grid space was used to select top values (roughly 5% of the total number of grid points) for statistical analysis. The average values and standard deviations of *J* for these grid points were taken as the first estimate of the true values of *J*. When necessary, finer grid points (e.g. 1 cm^{-1}) were used near low-*R* points to check for closely-spaced minima. Second, randomized (Monte Carlo) sampling of a reduced parameter space bounded by the grid-derived average and standard deviation values for *J* was used to test for convergence on the true values of *J*. Thirty 1000-point random sampling runs were performed, and the best values determined in each of these thirty runs used for statistical analysis. The values and standard deviations for *J* and *R* resulting from the Monte Carlo samples were used to determine convergence. Finally, the values from Monte Carlo sampling were optimized using a Nelder-Mead downhill simplex algorithm until the change in error on successive iterations was less than 1×10^{-6} times the total error.

$$R = \sum\left[(\chi_M T)_{exp} - (\chi_M T)_{calc}\right]^2 / \sum (\chi_M T)_{exp}{}^2 \qquad (2)$$

EPR Spectroscopy. X-band EPR spectroscopy was carried out using a Bruker Instruments (Billerica, MA) Elexsys EPR spectrometer equipped with a dual mode cavity. Temperature was controlled with an Oxford Instruments liquid helium cryostat. Samples were prepared at 1 mM concentrations in frozen solutions.

2.6 References

(1) This chapter is based upon a manuscript that is being prepared for future publication: Van Allsburg, K. M.; Lakshmi, K. V.; Tilley, T. D., *in preparation*. It is included here with the permission of all authors.

(2) Umena, Y.; Kawakami, K.; Shen, J.-R.; Kamiya, N. *Nature* **2011**, *473*, 55–60.

(3) Suga, M.; Akita, F.; Hirata, K.; Ueno, G.; Murakami, H.; Nakajima, Y.; Shimizu, T.; Yamashita, K.; Yamamoto, M.; Ago, H.; Shen, J.-R. *Nature* **2015**, *517*, 99–103.

(4) Debus, R. J. *Biochim. Biophys. Acta* **1992**, *1102*, 269–352.

(5) McEvoy, J.; Brudvig, G. W. *Chem. Rev.* **2006**, *106*, 4455–4483.

(6) Barber, J.; Murray, J. W. *Phil. Trans. R. Soc. B* **2008**, *363*, 1129–1138; discussion 1137–1138.

(7) Brudvig, G. W. *Phil. Trans. R. Soc. B* **2008**, *363*, 1211–1219.

(8) Sproviero, E. M.; Gascon, J. A.; McEvoy, J. P.; Brudvig, G. W.; Batista, V. S. *Coord. Chem. Rev.* **2008**, *252*, 395–415.

(9) Siegbahn, P. E. M. *Acc. Chem. Res.* **2009**, *42*, 1871–1880.

(10) Siegbahn, P. E. M. *J. Photochem. Photobiol., B* **2011**, *104*, 94–99.

(11) Pace, R. J.; Jin, L.; Stranger, R. *Dalton Trans.* **2012**, *41*, 11145–11160.

(12) Najafpour, M. M.; Moghaddam, A. N.; Yang, Y. N.; Aro, E.-M.; Carpentier, R.; Eaton-Rye, J. J.; Lee, C.-H.; Allakhverdiev, S. I. *Photosynth. Res.* **2012**, *114*, 1–13.

(13) Cox, N.; Pantazis, D. A.; Neese, F.; Lubitz, W. *Acc. Chem. Res.* **2013**, *46*, 1588–1596.

(14) Najafpour, M. M.; Ghobadi, M. Z.; Larkum, A. W.; Shen, J.-R.; Allakhverdiev, S. I. *Trends Plant Sci.* **2015**, *20*, 559–568.

(15) Kok, B.; Forbush, B.; McGloin, M. *Photochem. Photobiol.* **1970**, *11*, 457–475.

(16) Yano, J.; Yachandra, V. K. *Photosynth. Res.* **2007**, *92*, 289–303.

(17) Kuzek, D.; Pace, R. J. *Biochim. Biophys. Acta* **2001**, *1503*, 123–137.

(18) Carrell, G.; Tyryshkin, M.; Dismukes, C. *J. Biol. Inorg. Chem.* **2002**, *7*, 2–22.

(19) Dismukes, G. C.; Brimblecombe, R.; Felton, G. A. N.; Pryadun, R. S.; Sheats, J. E.; Spiccia, L.; Swiegers, G. F. *Acc. Chem. Res.* **2009**, *42*, 1935–1943.

(20) Siegbahn, P. E. M. *Chem. Eur. J.* **2006**, *12*, 9217–9227.

(21) Siegbahn, P. E. M. *Chem. Eur. J.* **2008**, *14*, 8290–8302.

(22) Siegbahn, P. E. M. *Biochim. Biophys. Acta* **2013**, *1827* , 1003–1019.

(23) Christou, G.; Vincent, J. B. *Biochim. Biophys. Acta* **1987**, *895*, 259–274.

(24) Vincent, J. B.; Christou, G. *Inorg. Chim. Acta* **1987**, *136*, L41–L43.

(25) Cox, N.; Retegan, M.; Neese, F.; Pantazis, D. A.; Boussac, A.; Lubitz, W. *Science* **2014**, *345*, 804–808.

(26) Capone, M.; Bovi, D.; Narzi, D.; Guidoni, L. *Biochemistry* **2015**, *54*, 6439–6442.

(27) Gagliardi, C. J.; Westlake, B. C.; Kent, C. A.; Paul, J. J.; Papanikolas, J. M.; Meyer, T. J. *Coord. Chem. Rev.* **2010**, *254*, 2459–2471.

(28) Siegbahn, P. E. M.; Blomberg, M. R. A. *Chem. Rev.* **2010**, *110*, 7040–7061.

(29) Dasgupta, J.; van Willigen, R.; Dismukes, G. *Phys. Chem. Chem. Phys.* **2004**, *6*, 4793–4802.
(30) Miqyass, M.; Gorkom, H. J.; Yocum, C. F. *Photosynth. Res.* **2007**, *92*, 275–287.
(31) Wieghardt, K. *Angew. Chem. Int. Ed. Engl.* **1989**, *28*, 1153–1172.
(32) Manchanda, R.; Crabtree, R. H.; Brudvig, G. W. *Coord. Chem. Rev.* **1995**, *144*, 1–38.
(33) Yagi, M.; Kaneko, M. *Chem. Rev.* **2001**, *101*, 21–36.
(34) Wu, A. J.; Penner-Hahn, J. E.; Pecoraro, V. L. *Chem. Rev.* **2004**, *104*, 903–938.
(35) Mukhopadhyay, S.; Mandal, S. K.; Bhaduri, S.; Armstrong, W. H. *Chem. Rev.* **2004**, *104*, 3981–4026.
(36) Pecoraro, V.; Hsieh, W. *Inorg. Chem.* **2008**, *47*, 1765–1778.
(37) Mullins, C. S.; Pecoraro, V. L. *Coord. Chem. Rev.* **2008**, *252*, 416–443.
(38) Cady, C. W.; Crabtree, R. H.; Brudvig, G. W. *Coord. Chem. Rev.* **2008**, *252*, 444–455.
(39) Liu, X.; Wang, F. *Coord. Chem. Rev.* **2012**, *256*, 1115–1136.
(40) Limburg, B.; Bouwman, E.; Bonnet, S. *Coord. Chem. Rev.* **2012**, *256*, 1451–1467.
(41) Singh, A.; Spiccia, L. *Coord. Chem. Rev.* **2013**, *257*, 2607–2622.
(42) Hirahara, M.; Shoji, A.; Yagi, M. *Eur. J. Inorg. Chem.* **2014**, *2014*, 595–606.
(43) Asraf, M. A.; Younus, H. A.; Yusubov, M.; Verpoort, F. *Catal. Sci. Technol.* **2015**, *5*, 4901–4925.
(44) Limburg, J.; Brudvig, G. W.; Crabtree, R. H. *J. Am. Chem. Soc.* **1997**, *119*, 2761–2762.
(45) Caudle, M. T.; Riggs-Gelasco, P.; Gelasco, A. K.; Penner-Hahn, J. E.; Pecoraro, V. L. *Inorg. Chem.* **1996**, *35*, 3577–3584.
(46) Randall, D. W.; Gelasco, A.; Caudle, M. T.; Pecoraro, V. L.; Britt, R. D. *J. Am. Chem. Soc.* **1997**, *119*, 4481–4491.
(47) Gelasco, A.; Bensiek, S.; Pecoraro, V. L. *Inorg. Chem.* **1998**, *37*, 3301–3309.
(48) Limburg, J.; Vrettos, J. S.; Liable-Sands, L. M.; Rheingold, A. L.; Crabtree, R. H.; Brudvig, G. W. *Science* **1999**, *283*, 1524–1527.
(49) Sun, L.; Raymond, M. K.; Magnuson, A.; LeGourriérec, D.; Tamm, M.; Abrahamsson, M.; Huang Kenéz, P.; Mårtensson, J.; Stenhagen, G.; Hammarström, L.; Styring, S.; Åkermark, B. *J. Inorg. Biochem.* **2000**, *78*, 15–22.
(50) Peloquin, J. M.; Campbell, K. A.; Randall, D. W.; Evanchik, M. A.; Pecoraro, V. L.; Armstrong, W. H.; Britt, R. D. *J. Am. Chem. Soc.* **2000**, *122*, 10926–10942.
(51) Limburg, J.; Vrettos, J. S.; Chen, H.; de Paula, J. C.; Crabtree, R. H.; Brudvig, G. W. *J. Am. Chem. Soc.* **2001**, *123*, 423–430.
(52) Randall, D. W.; Sturgeon, B. E.; Ball, J. A.; Lorigan, G. A.; Chan, M. K.; Klein, M. P.; Armstrong, W. H.; Britt, R. D. *J. Am. Chem. Soc.* **2002**, *117*, 11780–11789.
(53) Huang, P.; Magnuson, A.; Lomoth, R.; Abrahamsson, M.; Tamm, M.; Sun, L.; van Rotterdam, B.; Park, J.; Hammarström, L.; Åkermark, B.; Styring, S. *J. Inorg. Biochem.* **2002**, *91*, 159–172.
(54) Lomoth, R.; Huang, P.; Zheng, J.; Sun, L.; Hammarström, L.; Åkermark, B.;

Styring, S. *Eur. J. Inorg. Chem.* **2002**, *2002*, 2965–2974.
(55) Baffert, C.; Collomb, M.-N.; Deronzier, A.; Kjærgaard-Knudsen, S.; Latour, J.-M.; Lund, K. H.; McKenzie, C. J.; Mortensen, M.; Nielsen, L. P.; Thorup, N. *Dalton Trans.* **2003**, 1765–1772.
(56) Shimazaki, Y.; Nagano, T.; Takesue, H.; Ye, B.; Tani, F.; Naruta, Y. *Angew. Chem. Int. Ed.* **2004**, *43*, 98–100.
(57) Anderlund, M. F.; Högblom, J.; Shi, W.; Huang, P.; Eriksson, L.; Weihe, H.; Styring, S.; Åkermark, B.; Lomoth, R.; Magnuson, A. *Eur. J. Inorg. Chem.* **2006**, *2006*, 5033–5047.
(58) Beckmann, K.; Uchtenhagen, H.; Berggren, G.; Anderlund, M. F.; Thapper, A.; Messinger, J.; Styring, S.; Kurz, P. *Energy Environ. Sci.* **2008**, *1*, 668–676.
(59) Najafpour, M. M.; McKee, V. *Catal. Commun.* **2010**, *11*, 1032–1035.
(60) Berggren, G.; Thapper, A.; Huang, P.; Eriksson, L.; Styring, S.; Anderlund, M. F. *Inorg. Chem.* **2011**, *50*, 3425–3430.
(61) Berends, H.-M.; Manke, A.-M.; Näther, C.; Tuczek, F.; Kurz, P. *Dalton Trans.* **2012**, *41*, 6215–6224.
(62) Bhula, R.; Gainsford, G. J.; Weatherburn, D. C. *J. Am. Chem. Soc.* **1988**, *110*, 7550–7552.
(63) Mukherjee, S.; Stull, J. A.; Yano, J.; Stamatatos, T. C.; Pringouri, K.; Stich, T. A.; Abboud, K. A.; Britt, R. D.; Yachandra, V. K.; Christou, G. *Proc. Natl. Acad. Sci. U. S. A.* **2012**, *109*, 2257–2262.
(64) Hsieh, W.-Y.; Campbell, K. A.; Gregor, W.; David Britt, R.; Yoder, D. W.; Penner-Hahn, J. E.; Pecoraro, V. L. *Biochim. Biophys. Acta* **2004**, *1655*, 149–157.
(65) Berggren, G.; Thapper, A.; Huang, P.; Kurz, P.; Eriksson, L.; Styring, S.; Anderlund, M. F. *Dalton Trans.* **2009**, 10044–10054.
(66) Kanady, J. S.; Tran, R.; Stull, J. A.; Lu, L.; Stich, T. A.; Day, M. W.; Yano, J.; Britt, R. D.; Agapie, T. *Chem. Sci.* **2013**, *4*, 3986–3996.
(67) Zhang, C.; Chen, C.; Dong, H.; Shen, J.-R.; Dau, H.; Zhao, J. *Science* **2015**, *348*, 690–693.
(68) Schwarz, B.; Forster, J.; Goetz, M. K.; Yücel, D.; Berger, C.; Jacob, T.; Streb, C. *Angew. Chem. Int. Ed.* **2016**, DOI: 10.1002/anie.201601799.
(69) Ruettinger, W.; Yagi, M.; Wolf, K.; Bernasek, S.; Dismukes, G. *J. Am. Chem. Soc.* **2000**, *122*, 10353–10357.
(70) Ruettinger, W.; Dismukes, G. *Inorg. Chem.* **2000**, *39*, 1021–1027.
(71) Hocking, R. K.; Brimblecombe, R.; Chang, L.-Y.; Singh, A.; Cheah, M. H.; Glover, C.; Casey, W. H.; Spiccia, L. *Nature Chem.* **2011**, *3*, 461–466.
(72) Kanady, J. S.; Tsui, E. Y.; Day, M. W.; Agapie, T. *Science* **2011**, *333*, 733–736.
(73) Kanady, J. S.; Mendoza-Cortes, J. L.; Tsui, E. Y.; Nielsen, R. J.; Goddard, W. A., III; Agapie, T. *J. Am. Chem. Soc.* **2013**, *135*, 1073–1082.
(74) Tsui, E. Y.; Tran, R.; Yano, J.; Agapie, T. *Nature Chem.* **2013**, *5*, 293–299.
(75) Kanady, J. S.; Lin, P.-H.; Carsch, K. M.; Nielsen, R. J.; Takase, M. K.; Goddard, W. A., III; Agapie, T. *J. Am. Chem. Soc.* **2014**, *136*, 14373–14376.

(76) Ruettinger, W.; Campana, C.; Dismukes, G. *J. Am. Chem. Soc.* **1997**, *119*, 6670–6671.
(77) Carrell, T.; Cohen, S.; Dismukes, G. *J. Molec. Catal. A: Chem.* **2002**, *187*, 3–15.
(78) Lugmair, C. G.; Tilley, T. D.; Rheingold, A. L. *Chem. Mater.* **1997**, *9*, 339–348.
(79) Lugmair, C. G.; Tilley, T. D. *Inorg. Chem.* **1998**, *37*, 6304–6307.
(80) Lugmair, C. G.; Tilley, T. D.; Rheingold, A. L. *Chem. Mater.* **1999**, *11*, 1615–1620.
(81) Fujdala, K. L.; Tilley, T. D. *Chem. Mater.* **2004**, *16*, 1035–1047.
(82) Ahn, H. S.; Tilley, T. D. *Adv. Funct. Mater.* **2012**, *23*, 227–233.
(83) Murugavel, R.; Sathiyendiran, M.; Walawalkar, M. G. *Inorg. Chem.* **2001**, *40*, 427–434.
(84) Sathiyendiran, M.; Murugavel, R. *Inorg. Chem.* **2002**, *41*, 6404–6411.
(85) Pothiraja, R.; Sathiyendiran, M.; Butcher, R. J.; Murugavel, R. *Inorg. Chem.* **2004**, *43*, 7585–7587.
(86) Murugavel, R.; Choudhury, A.; Walawalkar, M. G.; Pothiraja, R.; Rao, C. N. R. *Chem. Rev.* **2008**, *108*, 3549–3655.
(87) Krewald, V.; Retegan, M.; Neese, F.; Lubitz, W.; Pantazis, D. A.; Cox, N. *Inorg. Chem.* **2015**, *55*, 488–501.
(88) Peloquin, J. M.; Britt, R. D. *Biochim. Biophys. Acta* **2001**, *1503*, 96–111.
(89) Feher, G. *Bell Syst. Tech. J.* **1957**, *36* (2), 449–484.
(90) Yamauchi, T.; Mino, H.; Matsukawa, T.; Kawamori, A.; Ono, T. *Biochemistry* **1997**, *36*, 7520–7526.
(91) Haddy, A.; Lakshmi, K. V.; Brudvig, G. W.; Frank, H. A. *Biophys. J.* **2004**, *87*, 2885–2896.
(92) Dismukes, G. C.; Siderer, Y. *FEBS Lett.* **1980**, *121*, 78–80.
(93) Dismukes, G. C.; Siderer, Y. *Proc. Natl. Acad. Sci. U. S. A.* **1981**, *78*, 274–278.
(94) Zimmermann, J. L.; Rutherford, A. W. *Biochim. Biophys. Acta* **1984**, *767*, 160–167.
(95) Casey, J. L.; Sauer, K. *Biochim. Biophys. Acta* **1984**, *767*, 21–28.
(96) Haddy, A. *Photosynth. Res.* **2007**, *92*, 357–368.
(97) Haddy, A.; Dunham, W. R.; Sands, R. H.; Aasa, R. *Biochim. Biophys. Acta* **1992**, *1099*, 25–34.
(98) Boussac, A.; Rutherford, A. W. *Biochim. Biophys. Acta* **2000**, *1457*, 145–156.
(99) Larson, E.; Haddy, A.; Kirk, M. L.; Sands, R. H.; Hatfield, W. E.; Pecoraro, V. L. *J. Am. Chem. Soc.* **1992**, *114*, 6263–6265.
(100) Liang, W.; Latimer, M. J.; Dau, H.; Roelofs, T. A.; Yachandra, V. K.; Sauer, K.; Klein, M. P. *Biochemistry* **1994**, *33*, 4923–4932.
(101) Pantazis, D. A.; Ames, W.; Cox, N.; Lubitz, W.; Neese, F. *Angew. Chem. Int. Ed.* **2012**, *51*, 9935–9940.
(102) Pokhrel, R.; Brudvig, G. W. *Phys. Chem. Chem. Phys.* **2014**, *16*, 11812–11821.
(103) Stoll, S.; Schweiger, A. *J. Magn. Reson.* **2006**, *178*, 42–55.

Chapter 3

Efforts to Immobilize Mn_4O_4 and Co_4O_4 Cubanes on Electrically Conductive Substrates

3.1 Introduction

One of the most interesting structure types in catalyst preparation is a molecular catalyst anchored covalently to a suitable surface. This type of assembly can (a) impart stability (by limiting self-reaction), (b) change or improve catalytic activity or selectivity (by changing surface energies, eliminating mechanisms with states that are bi- or termolecular in the molecular catalyst, or by providing ancillary sites for binding of product,[1-7] (c) when a conductive support is used, allow facile electrochemistry, including accurate determination of catalyst TOF and limiting TON, since redox waves of the catalyst may be used as a measure of loading,[8] and (d) facilitate incorporation of catalysts into practical devices for artificial photosynthesis. Thereby, covalent surface-attachment of molecular catalysts is useful not just as a tool for improving catalytic performance, but also as a key source of insight on the entire catalytic system.

Covalent immobilization efforts described in this chapter, which followed directly from the results described in the first chapter, were accompanied (aside from section 3.2 below) by a transition from $Mn(III)_2Mn(IV)_2O_4$ cubanes to $Co(III)_4O_4$ cubanes. This transition was motivated by the informative but unsuccessful thermolytic precursor strategy described in Chapter 1 for $Mn_4O_4[O_2P(O\textit{t}Bu)_2]_6$ (**1**). In particular, the previously described complex $Co_4O_4(py)_4(OAc)_4$ (**2**) is an excellent candidate for immobilization for several reasons. First, it is robust (and even soluble) under aqueous, oxygenated conditions,[9-12] making it a much more promising precursor to heterogenized catalyst systems. Second, its solution-phase water oxidation activity has been reaffirmed[12] after vigorous inquiry,[10-12] while no example of Mn cubane catalysis remains unquestioned.[13] Third, unpublished studies by the Tilley group have established that a wide variety of ligand substitutions can be performed on complex **2** while preserving the Co_4O_4 core, which suggests that immobilization strategies for Co_4O_4 complexes might be both successful and versatile.

A variety of substrates and linker chemistries were considered for immobilization of Mn_4O_4 and Co_4O_4 cubanes. They were selected for their relevance to artificial photosynthesis device and benchmarking conditions, and to the ligand sets of the cubanes being anchored. Substrate/linker systems include electrochemical reduction of a diazonium salt to install phosphonate groups onto glassy carbon, functionalization of transparent conducting oxides with dicarboxylic acids and silanes, covalent modification of multiwalled carbon nanotubes, and electropolymerization of functionalized thiophene and pyrrole compounds.

3.2 Immobilization of Complex 1 on Electrochemically Functionalized Glassy Carbon Electrodes

3.2.1 Introduction

Electrochemical reduction of diazonium salts is a convenient and widely-used method for functionalization of carbon-based electrodes.[14-16] Methods to limit layer growth, promoting the formation of monolayers with excellent electrode contact and amenability to

further functionalization, have been described.[17] A simple one-step method was used to produce phosphonic acid-functionalized glassy carbon electrodes as a potential substrate for covalent immobilization of Mn_4O_4 complex **1**.

3.2.2 Functionalization of glassy carbon

Glassy carbon electrodes were derivatized by sweeping the glassy carbon electrode potential between 0.54 and –0.8 V *vs.* Ag/AgCl in a solution of phosphonic acid-functionalized diazonium salt, generated *in situ* (Scheme 1). The electrodes were then washed and sonicated with deionized water. The presence of the phosphonic acid was verified by phosphorus XPS.

Scheme 1. Functionalization of glassy carbon with phosphonate groups *via* electrochemical reduction of sodium 4-phosphonobenzenediazonium, followed by treatment with complex **1**.

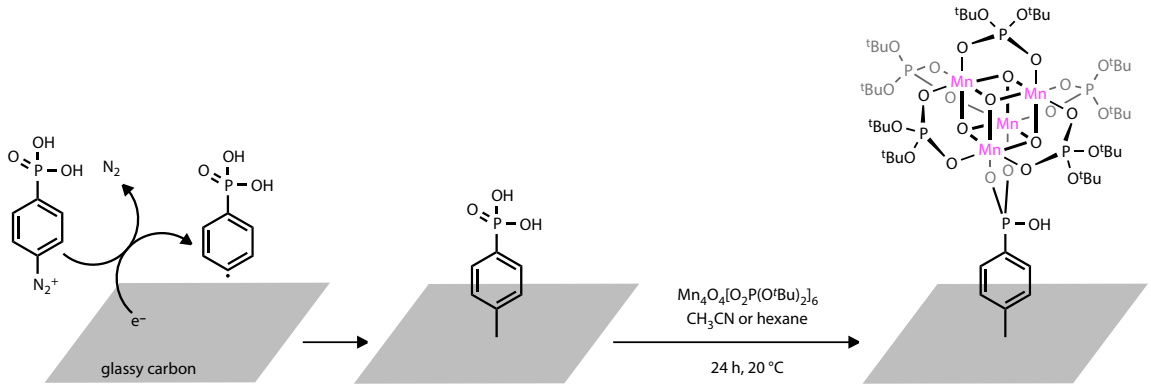

Anchoring of complex **1** was attempted in both hexane and acetonitrile at 20 °C under air- and moisture-free conditions. Loading of Mn on the glassy carbon discs was verified by manganese XPS.

3.2.3 Characterization of functionalized glassy carbon

As in Chapter 1, the most effective method for characterizing the fate of Mn_4O_4 units after attempted immobilization was found to be X-ray absorption spectroscopy (XAS). XAS on the Mn-functionalized glassy carbon (Mn@GC) materials revealed an edge energy that is intermediate between those of the $Mn(III)_2Mn(IV)_2$ complex **1** and the related $Mn(II)_2Mn(III)_2$ butterfly structure $Mn_4O_2[O_2P(O\textit{t}Bu)_2]_6(OPEt_3)_2$ (Figure 1). In fact, the spectra observed for Mn@GC may be reasonably approximated as a linear combination of these two reference compounds. However, the reduction in edge energy and poor resolution at higher energies strongly suggest that the Mn@GC surface structure does not predominantly (or perhaps even partially) contain intact Mn_4O_4 units.

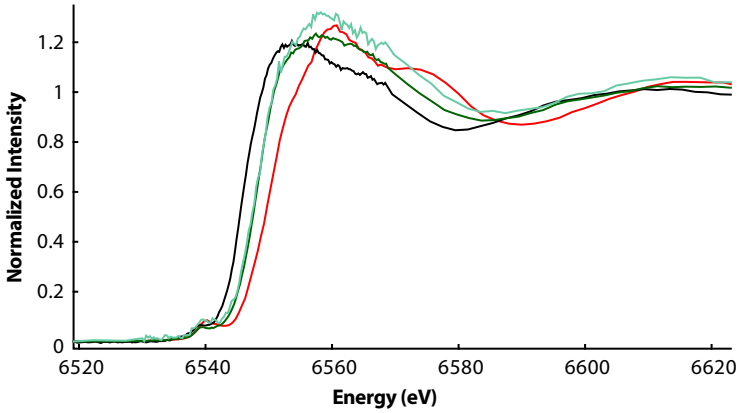

Figure 1. Mn K-edge absorption spectra of complex **1** (red), $Mn_4O_2[O_2P(OtBu)_2]_6(OPEt_3)_2$ (black), and Mn@GC samples prepared using hexane (light green) or acetonitrile (dark green).

3.2.4 Discussion

Immobilization of complex **1** on functionalized glassy carbon did not lead to a structure that could be unambiguously assigned as having intact Mn_4O_4 units. However, it remains reasonable to consider structural models for the surface sites that maintain manganese tetramers (perhaps a mixture of "closed", *i.e.* cubane, and "open", *i.e.* butterfly, sites). Further work with this system, such as oxidation of the surface to reinstall oxo ligands and regenerate a cubane in a manner similar to that described in Chapter 1, might yield interesting and electrochemically accessible structures. However, the inherent limitations of both complex **1**, including water sensitivity, and the glassy carbon support, which requires use of expensive and unwieldy electrode disks, motivated the efforts described in the next section with complex **2** and new substrate/linker chemistries.

3.3 Immobilization of Complex 2 on Transparent Conducting Oxides

3.3.1 Introduction

Transparent conducting oxides (TCO), especially fluorine-doped tin oxide (FTO) and indium-doped tin oxide (ITO), are extensively used in catalyst and light absorber testing because of their favorable properties, including low cost, transparency to the solar spectrum, scalability (electrodes of arbitrary dimensions can be cut easily), and acceptable materials properties (*e.g.* conductivity, roughness, stability).[18,19] They can be purchased or deposited as conformal films on a support material (*e.g.* borosilicate glass or silicon). They are commonly used in the Joint Center for Artificial Photosynthesis, where much of this work was conducted.[20-22] Nanoporous ITO ("*nano*ITO") films generated by sintering of ITO nanocrystals are also known[23,24] and were used in some of the studies here to improve

geometric loading of Co_4O_4. However, prior work on covalent attachment of molecular catalysts to FTO or ITO substrates is somewhat limited. Therefore, much of the work described here investigated the adaptation to TCO of linker chemistries previously used for other substrates.

The linker chemistries used to derivatize TCO substrates include, first, direct ligand exchange of surface –OH sites with ligands on $Co_4O_4(py)_4(OAc)_4$ (**2**) (*i.e.* electrostatic anchoring). Previous examples of this attachment strategy include an Mn_2O_2 dimer immobilized on silica[6] for water oxidation with Ce(IV) and an Ir_2O_2 dimer on *nano*ITO for electrochemical water oxidation.[25] The strategy is very simple – soaking the substrate in a solution of complex **2** will suffice. Second, linkers with multiple –COOH groups could coordinate both surface atoms and complex **2**, by displacing an acetate ligand. Linkers used in this strategy include oxalic acid and citric acid. Citric acid has been used previously to control nanocrystal growth by coordinating metal and metal oxide surfaces[26-28] and to derivatize those surfaces.[29] Third, tailored linkers containing both a silane, for covalent linkage to the TCO surface, and a carboxylic acid or ester, for later coordination to complex **2** (Figure 2), are commercially available. Sodium carboxyethylsilanetriol (CES), an anionic silanol, has been used to prepare COOH-functionalized silica, nanoparticles, and thin films.[30-34] Methods to prepare a self-assembled monolayer (SAM) have been described,[30,34] but not catalyst immobilization. 2-(Carbomethoxy)ethyltrimethoxysilane (CMEMS) was used, after deprotection, to anchor Mn_2O_x dimers on silica[35-38] and prepare "zwitterionic nanoparticles",[39] but SAM formation conditions were not described. (2-Cyanoethyl)triethoxysilane (CTES) was used to prepare COOH-functionalized mesoporous silica (by acid-catalyzed hydrolysis of –CN), which was then used as a substrate for complex **2**.[40,41] Adapting this result to a conductive substrate would expand its significance. CTES was also used to immobilize Rh, Ru, and Co epoxidation catalysts.[42,43] Finally, sodium 3-(trihydroxysilyl)propylmethylphosphonate (THSPMP) has been used to functionalize nanoparticles.[44-46] All of these monomers are available from Gelest Inc.

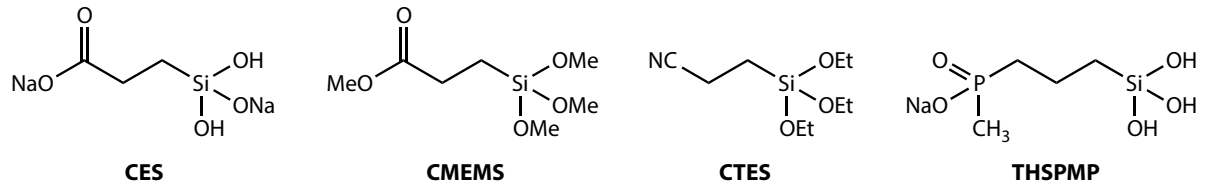

Figure 2. Silane linkers used for TCO functionalization.

A final note for TCO substrates: a typical FTO or ITO piece used in these studies has an area of approximately 2 cm^2. The quantity of contaminant required to form a monolayer film on a substrate of this size is extremely small (on the order of 5 x 10^{14} molecules or 1 x 10^{-11} mol), and chemistry on these surfaces is therefore very susceptible to contaminants. A washing and UV ozone treatment method was developed, based on previous work,[47] to minimize surface contamination and promote desired chemistry. Other cleaning

methods, including oxygen plasma and Me_3OBF_4 treatments,[48] were tested but were found to degrade or contaminate the surface.

3.3.2 Functionalization of TCO

FTO and *nano*ITO substrates were prepared for anchoring by rinsing and sonication with acetone, isopropanol, and deionized water.[47] They were then dried with a nitrogen gun and cleaned to remove carbon contamination by 30 min UV ozone treatment. The length of treatment was chosen to produce a stable (*i.e.* no change with further treatment) and low contact angle for water on each substrate. After cleaning, the substrates were used for the next step within ten minutes. For CMEMS, the substrates were further prepared by drying under active vacuum for 24 h.

Oxalic and citric acid linker layers were prepared by immersing a clean *nano*ITO film in an acetonitrile solution of the linker (proposed reaction shown in equation 1), followed by rinsing and sonication with acetonitrile to remove physisorbed linker.[23,49]

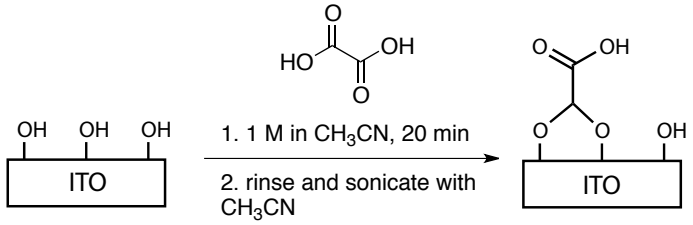

(1)

CES films were prepared by soaking a clean FTO film in an aqueous solution of the linker (equation 2), under conditions described previously as appropriate to yield a monolayer coating.[30,34] Following the published procedure, the film was annealed after rinsing and sonication to achieve covalent linkage of all silanol groups with surface atoms or adjacent silane molecules. This step provides a more stable film.

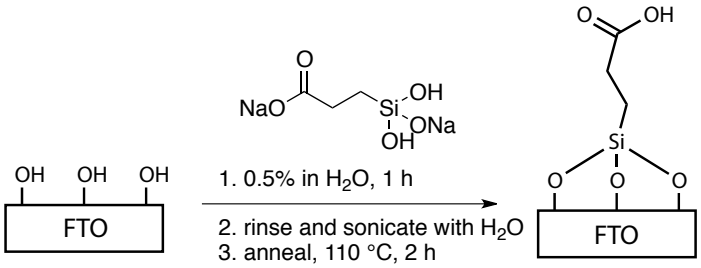

(2)

CMEMS films were prepared by adding a toluene solution of the silane to FTO under air- and water-free conditions at 65 °C (equation 3). Previous work with this ligand had used pyridine as a solvent,[38] but toluene was chosen here to pursue monolayer formation.[47] The FTO slides were then washed and sonicated as in the initial cleaning step.

Some samples were then deprotected in a 1 M HCl solution at reflux, while some were tested without deprotection.

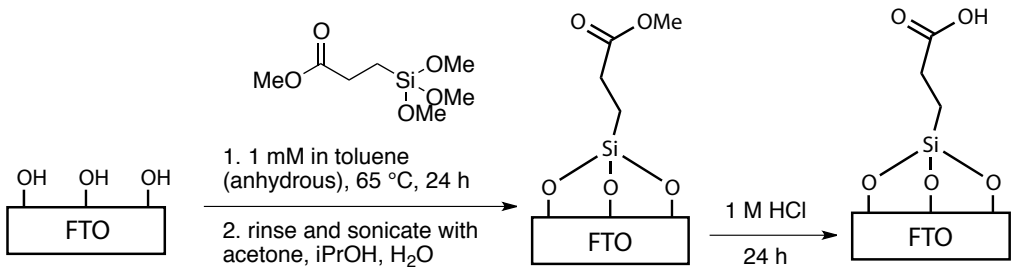

(3)

Complex **2** was prepared and purified with EDTA to remove Co(II) impurities,[11,12] as previously described.[12] Anchoring of complex **2** on the functionalized electrodes was accomplished by soaking the electrode in a dichloromethane solution of the complex for 24 h, followed by rinsing and sonication with dichloromethane to remove physisorbed **2**.

3.3.3 Characterization of functionalized TCO

Diffuse reflectance infrared spectroscopy was used previously by Das and co-workers to support their conclusion that complex **2** or an analogue had been deposited on silica with the Co_4O_4 units intact.[40,41] For the ITO-immobilized films, attenuated total reflection (ATR) measurements, which allow characterization of thin or monolayer films, are more appropriate.[50-54] ATR-IR studies of the films in this section did not reveal any peaks that were easily assigned to complex **2** or a putative Co_4O_4 unit.

Loading of Co on the oxalate-*nano*ITO and citrate-*nano*ITO films was confirmed by XPS. The identity of the anchored Co material was probed with XAS, as in Chapter 1. The Co K-edge energies observed by X-ray absorption near edge structure (XANES) spectroscopy for the immobilized Co species and complex **2** are similar (Figure 3). The coordination environment observed by Fourier-transform extended X-ray absorption fine structure (FT-EXAFS) spectroscopy is also similar in the two samples. These observations tentatively support an assignment of the Co species on oxalate-*nano*ITO as intact Co_4O_4 cubane. However, the poor signal-to-noise observed for the immobilized sample because of low loading and sample geometry (monolayer) precludes drawing a stronger conclusion.

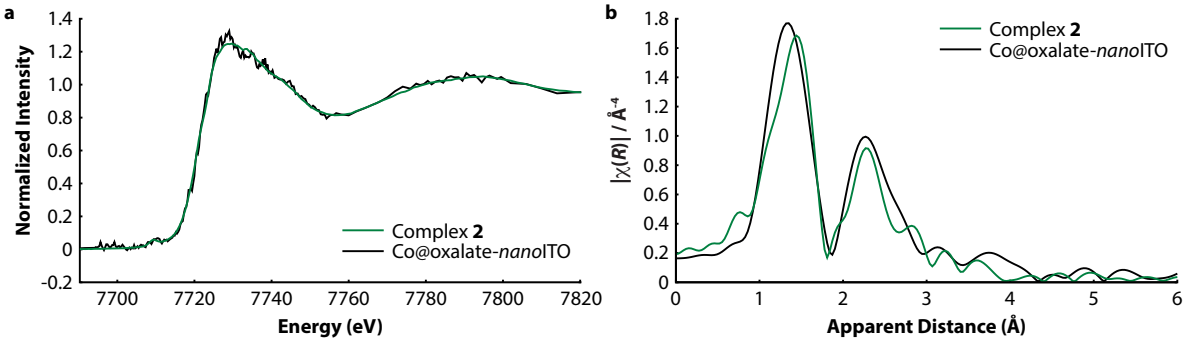

Figure 3. Co K-edge absorption spectra for complex **2** (green) and anchored Co@oxalate-*nano*ITO (black), showing reasonable agreement despite the low signal-to-noise for the latter sample: a) XANES and b) FT-EXAFS.

CES-FTO films were treated with complex **2** under the same conditions as those used for oxalate/citrate-*nano*ITO. XPS confirmed the presence of cobalt. XAS, however, revealed clear decomposition of the majority of Co_4O_4 units during anchoring (Figure 4). A shift in edge energy and a sharper white line in the XANES spectrum are consistent with reduction to Co(II), and a lengthening of Co–O contacts with loss of Co–Co peaks in the FT-EXAFS spectrum reveals disintegration of Co_4O_4 units.

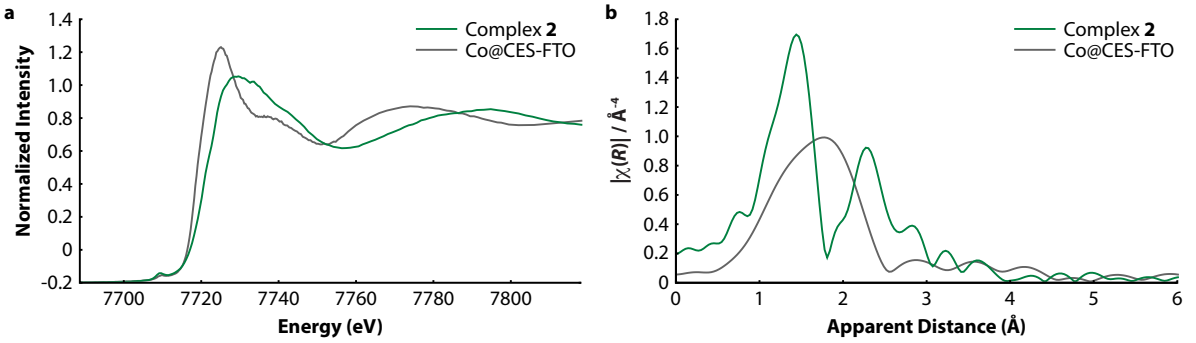

Figure 4. Co K-edge absorption spectra of Co@CES-FTO samples (grey), showing clear decomposition of Co_4O_4 units relative to complex **2** (green): a) XANES and b) FT-EXAFS.

CMEMS-FTO films were tested using a series of control experiments and XPS characterization. Cleaned but otherwise untreated FTO ("bare FTO", samples 1 and 4), FTO treated with CMEMS but not deprotected (samples 2 and 5), and FTO treated with CMEMS and deprotected with HCl (samples 3 and 6) were used. For each of the foregoing, one sample was treated with complex **2** in dichloromethane for 24 h (samples 4-6), and one was soaked in pure dichloromethane for 24 h (samples 1-3). With respect to silicon content, XPS would be expected to show silicon content only for samples 2, 3, 5, and 6, or show substantially higher content than for 1 and 4. In fact, the silicon content observed was nearly

equal across all six samples (Chart 1). This result is difficult to rationalize – the penetration depth of XPS (approximately 10 nm) is too small to observe Si from the glass slide supporting the ~ 1 μm FTO film, and even if impurities in/on the FTO led to background Si signal, the signal would still be expected to increase on anchoring of a silane monolayer. The most likely explanation is that anchoring of CMEMS was largely unsuccessful.

Chart 1. Expected and observed Si content (violet) for Co@CMEMS-FTO and various control samples.

Expected/desired Si content:

	bare FTO	FTO treated with silane	FTO treated with silane, then deprotected with HCl
no Co added	1	2	3
soaked in Co4O4 solution	4	5	6

Found (by XPS):

	bare FTO	FTO treated with silane	FTO treated with silane, then deprotected with HCl
no Co added	1	2	3
soaked in Co4O4 solution	4	5	6

XPS analysis of Co content for the anchored materials also yielded disappointing results. While only the sample with available COOH groups (sample 6) would be expected to strongly bind complex **2**, all of the samples treated with complex **2** (samples 4-6) exhibited similar Co signals (Chart 2). Thus, no benefit to using the CMEMS linker was demonstrated.

Chart 2. Expected and observed Co content (green) for Co@CMEMS-FTO and various control samples.

Expected/desired Co content:

	bare FTO	FTO treated with silane	FTO treated with silane, then deprotected with HCl
no Co added	1	2	3
soaked in Co4O4 solution	4	5	6

Found (by XPS):

	bare FTO	FTO treated with silane	FTO treated with silane, then deprotected with HCl
no Co added	1	2	3
soaked in Co4O4 solution	4	5	6

3.3.4 Electrochemical characterization of anchored Co species

Of the initial anchoring methods tested, only oxalic acid on *nano*ITO was found to be tentatively successful by XPS and XAS experiments. However, before all of those results were available, routine electrochemical characterization *via* the reversible redox wave observed for complex **2** in acetonitrile solution was explored. Initially, electrodes were tested by affixing copper tape to the FTO electrode, but bubbling from the inert gas sparging caused acetonitrile to dissolve a component of the tape, which is, unfortunately, electrochemically active. Attempting the electrochemical characterization inside a glovebox to avoid the need for sparging did not eliminate the problem – acetonitrile vapors were sufficient to degrade the tape, producing a colored contaminant in the electrolyte. This issue is depicted in Figure 5.

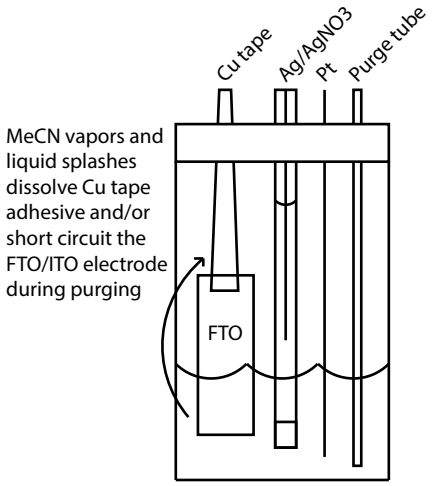

Figure 5. Contamination of electrolyte when copper tape is used to hold TCO samples.

To avoid these problems, a robust electrode assembly procedure was developed. First, a wire was affixed to the top of the FTO electrode with silver epoxy. Then, the wire was inserted into a glass tube. A solvent-resistant epoxy was used to completely coat the silver epoxy, wire, and opening of the glass tube, leaving an impermeable and electrically insulating seal on the wire-electrode junction. This method proved successful in eliminating contamination.

Cyclic voltammetry (CV) on all TCO materials produced disappointing results. The reversible wave previously observed in acetonitrile for complex **2** was not visible, even for samples (*e.g.* Co@oxalate-*nano*ITO) for which XAS indicated intact Co_4O_4 cubane units. Surprisingly, cyclic voltammetry of unbound complex **2** dissolved in acetonitrile produced quite different results at glassy carbon and FTO electrodes (Figure 6). Possible explanations for the discrepancy include: poor surface electron transfer, either intrinsic to the FTO or resulting from a passivating impurity; high sheet resistance for FTO; or a bad electrical junction between the potentiostat and FTO electrode. In an attempt to diagnose the problem, the redox couple of ferrocene in acetonitrile solution was also measured. With an FTO electrode, it exhibited a peak separation of 278 mV at 100 mV/s, significantly higher than the reversible value of 59 mV. This provides some insight but does not explain the result with complex **2**. In any case, the lack of a well-defined redox wave for the anchored complex prevents quantification of the number of electrochemically accessible Co_4O_4 sites in order to compare free and surface-bound catalytic activity,[8] a key objective of these efforts.

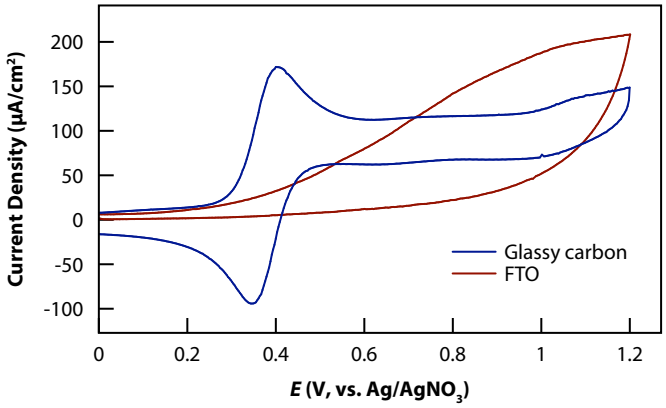

Figure 6. Cyclic voltammetry of 0.5 mM complex **2** dissolved in acetonitrile solution at glassy carbon (blue) and FTO (red) electrodes. Electrolyte: 100 mM NBu_4PF_6; reference electrode: $Ag/AgNO_3$; scan rate: 100 mV/s.

3.3.5 Discussion

Anchoring efforts for complex **2** on TCO substrates demonstrated limited success. The promising XAS spectra for Co@oxalate-*nano*ITO films may indicate potential for covalent immobilization of complex **2** using simple and inexpensive methods. The failure of silane linkers to adequately coat FTO surfaces and/or bind complex **2** better than unmodified FTO raises interesting questions about the surface chemistry. Further discussion of some of these factors is included in the conclusions below. Ultimately, the surprisingly poor electrochemical response observed for dissolved complex **2** and especially for surface-bound species prompted interest in another strategy.

3.4 Immobilization of Complex 2 on Multiwalled Carbon Nanotubes

3.4.1 Introduction

Covalent anchoring of various materials on carbon nanotubes has been demonstrated *via* a number of chemistries,[55] including derivatization of carboxylate defects,[56] diazonium coupling,[57,58] cycloadditions,[59,60] and alkali metal reductions,[61] among others. Significantly, a Ru_4 polyoxometalate complex was immobilized on multiwalled carbon nanotubes (MWCNTs) for use in electrochemical water oxidation.[62] The diazonium coupling method used in that study is straightforward and its mechanism has been studied.[63] Overall, MWCNT immobilization methods show promise for Co_4O_4 cubanes for a few key reasons, including the dramatic improvement in surface area afforded by depositing MWCNTs on an otherwise geometrically flat electrode, the ease of handling powdered MWCNTs *vs.* a glassy carbon disk or similar material, and the amenability of the powdered sample to characterization methods like X-ray absorption spectroscopy (XAS).

3.4.2 Functionalization of MWCNTs

Multiwalled carbon nanotubes were treated with isopentyl nitrite and 4-aminobenzoic acid in water at 80 ˚C for 16 h (equation 4). A previous attempt using sodium nitrite in 0.5 M HCl had produced material that required in excess of 20 washing steps and was ultimately impossible to separate from reaction byproducts. The isopentyl nitrite reaction products can be purified by a significantly shorter washing procedure with methanol and dimethylformamide.

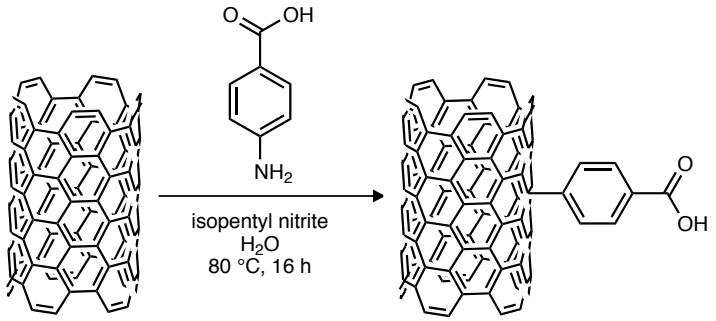

(4)

Functionalized MWCNTs were treated with a solution of complex **2** in methanol at 20 or 60 ˚C. A series of washing and sonication steps to remove physisorbed Co material and displaced ligands was used, which had been developed by subjecting unfunctionalized, pristine MWCNTs to the Co_4O_4 anchoring conditions and minimizing observed Co loading (see below).

3.4.3 Characterization of anchored species

The loading of material on the MWCNTs was investigated using thermogravimetric analysis (TGA).[62] TGA revealed that approximately 4.0 ± 0.4% of the Co@MWCNT material results from the addition of the complex, which corresponds to 50 ± 5 μmol/g assuming the anchored material retains complex **2**'s structure less one acetate ligand.

Raman spectroscopy, used previously to characterize a Ru-based water oxidation catalyst on MWCNTs,[62] was applied to Co@MWCNT samples at 633 nm. The samples did not exhibit bands characteristic of complex **2** at laser power low enough to avoid photodamage (Figure 7a). However, when high laser power was used to deliberately burn the sample, CoO_x peaks were observed that match those for complex **2** when similarly irradiated (Figure 7b). This result confirms that a cobalt-containing species was anchored, but does not provide information on its specific identity. The absence of any of the observed peaks for pristine MWCNTs was also verified at all tested laser powers.

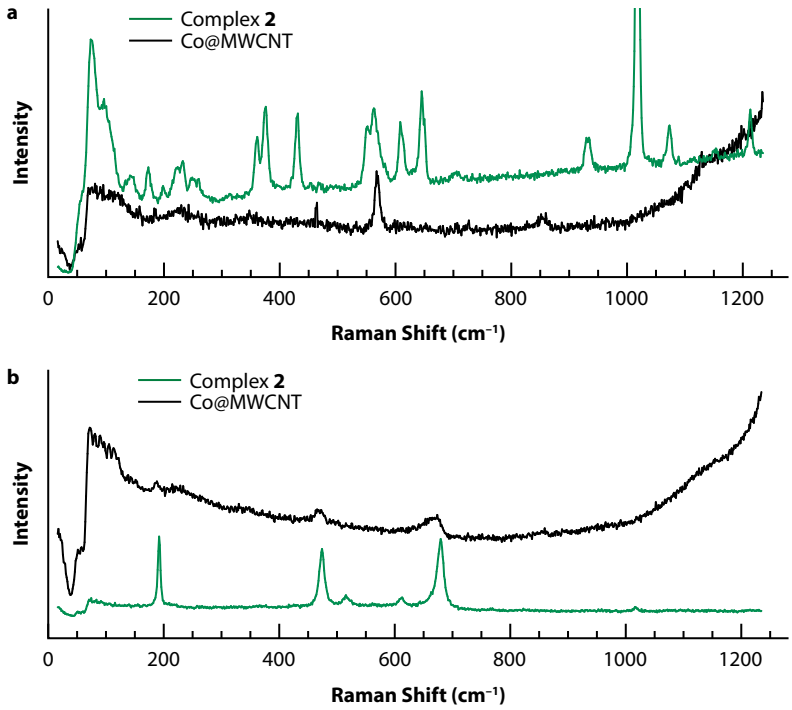

Figure 7. Raman spectra at a) low laser power (0.19 mW), showing the absence of clear peaks preserved from complex **2** (green) in Co@MWCNT samples (black) and b) high laser power (3.70 mW), showing similar CoO_x peaks in samples of complex **2** (green) and Co@MWCNT (black) resulting from photochemical/thermal decomposition.

Using the criteria described in section 3.3.3, XAS of the Co@MWCNT samples overwhelmingly indicates decomposition of the $Co(III)_4O_4$ units into isolated Co(II) centers. Figure 8 shows the XANES and EXAFS data.

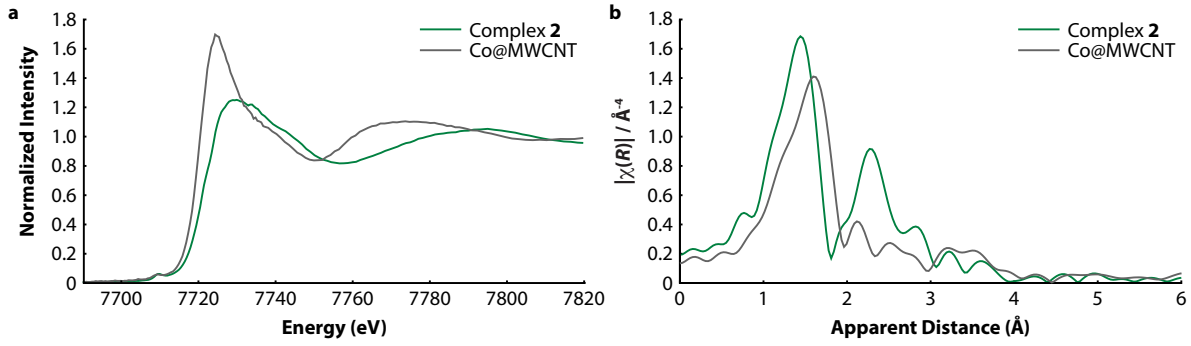

Figure 8. Co K-edge absorption spectra of Co@MWCNT samples (grey), showing clear decomposition of Co_4O_4 units relative to complex **2** (green): a) XANES and b) FT-EXAFS.

3.4.4 Discussion

Intrinsically, MWCNTs are perhaps the most amenable substrate of those described in this chapter, because of their ease of handling, scalability, and amenability to spectroscopy. Unfortunately, the MWCNT functionalization method did not provide intact Co_4O_4 units, as evidenced by XAS. Furthermore, the loading evidenced by TGA, XPS, and indirectly by XAS is somewhat low (4%) compared to previous work.[62] Therefore, a possible explanation could be a failure during the initial derivatization step, leaving few or no –COOH sites on the modified MWCNTs and thus yielding quite different results from those desired. However, substantially higher loading was obtained for treatment of derivatized *vs.* pristine MWCNTs with complex **2** (factor of 2–3), suggesting some species capable of binding complex **2** was, in fact, deposited. Another explanation is that the MWCNTs used in this study are less porous than those used in the previous study,[62] or that diffusion of the linker or complex **2** through the MWCNT is somehow hindered. These possibilities seem unlikely considering the smaller size of the molecular precursor used in this case and the fact that carbon nanotubes used in both studies were purchased from the same manufacturer with equivalent specifications. Further discussions of failure to generate intact, surface-bound Co_4O_4 sites are included in the conclusions below.

3.5 Immobilization of Complex 2 on Conducting, COOH-Functionalized Polymers Prepared by Electropolymerization

3.5.1 Introduction

Conducting polymers functionalized with carboxylate or carboxylic acid groups have been described based on thiophene and pyrrole monomers (Figure 9). COOH-functionalized polythiophenes are available commercially from Rieke Metals and can be synthesized by chemical[64,65] and electrochemical[66-69] means. For catalytic evaluation of anchored Co_4O_4 species, electropolymerization on a suitable electrode is most desirable, because it should allow facile electrochemistry after functionalization with the Co_4O_4 precursor. Electropolymerization to produce COOH-functionalized polypyrrole for electrochemical characterization of cytochrome *c*, whose redox activity requires the presence of COOH groups, has also been described.[70,71] The monomers used in this study include 3-thiopheneacetic acid,[66-69] 3-thiophenebutyric acid,[69] and 3-methyl-4-pyrrolylcarboxylic acid.[70,71]

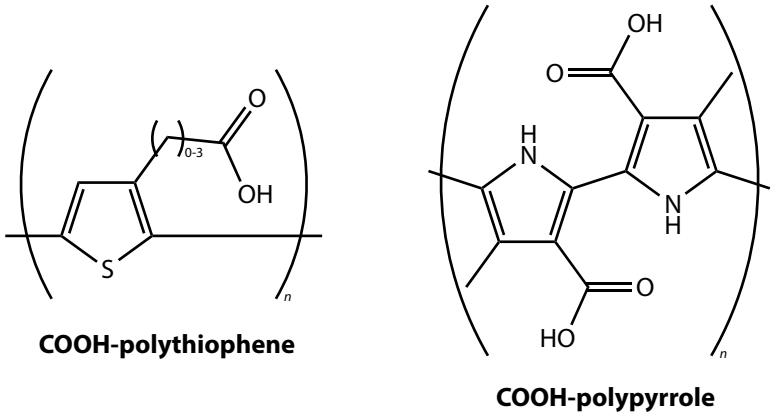

Figure 9. COOH-functionalized polymers for Co_4O_4 anchoring.

3.5.2 Electropolymerization of thiophene monomers

3-Thiopheneacetic acid and 3-thiophenebutyric acid were electropolymerized by repeated cyclic voltammetry cycles from 0 to 1.5 V *vs.* a $Ag/AgNO_3$ reference electrode in acetonitrile. Figure 10 shows the cyclic voltammogram for ten cycles, with increasing current on each cycle resulting from the redox wave of the deposited polymer. Initially, the substrate electrode used was FTO. Films deposited on this substrate were quite non-uniform, with some very dark areas and other areas having minimal deposited material. Cleaning the FTO using the procedure described in the TCO section above improved uniformity, as did repeated recrystallization of 3-thiopheneacetic acid,[68] but film quality remained low. Overall, film quality for the butyric acid monomer was better than for the acetic acid monomer.

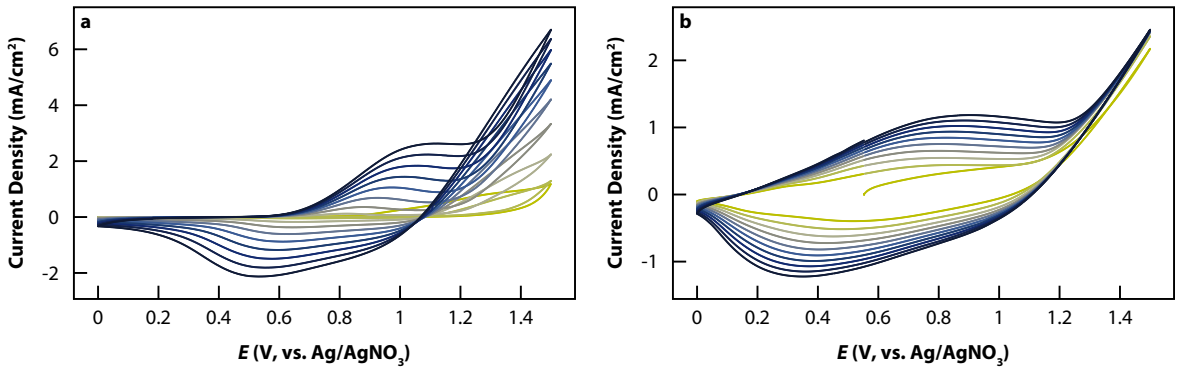

Figure 10. Cyclic voltammograms of thiophene electropolymerization on FTO, beginning at open circuit voltage and sweeping in the range E = 0–1.5 V for 10 cycles, showing growth of the redox wave corresponding to deposited (a) poly(3-thiopheneacetic acid) and (b) poly(3-thiophenebutyric acid). Reference electrode: $Ag/AgNO_3$; electrolyte: 100 mM NBu_4PF_6 in CH_3CN.

Improved film quality was obtained using Au films prepared on FTO by electron beam deposition. While still susceptible to damage if cleaned by sonication, films could be carefully soaked in solutions of complex **2** for anchoring and rinsed repeatedly. The improved quality can be rationalized by considering the known preference of sulfur donors for gold surfaces, *vs.* that of COOH donors for oxide surfaces. It is possible that a self-assembled monolayer of S-bound thiophene monomers forms, facilitating conformal film growth by favorably arranging the 2 and 5 positions of the thiophene ring.

3.5.3 Attempted synthesis and electropolymerization of a pyrrole monomer

Synthesis of 3-methyl-4-pyrrolylcarboxylic acid was pursued using the literature procedure[70-73] (Scheme 2), including enolate attack on aminoacetone followed by a cyclizing condensation, thermal decarboxylation, and ester cleavage. While this sequence of reactions, including performing the latter two steps separately, was reported[71] to limit formation of the undesired product (structures highlighted in red in Scheme 2), such selectivity was not observed. In fact, over several attempts, the yield of undesired 4-methyl-2-pyrrolylcarboxylic acid exceeded that of 3-methyl-4-pyrrolylcarboxylic acid. The low yield of this reaction sequence (8% for both isomers), while similar to that reported previously (4%),[71] complicated further purification. Attempts to use the impure monomer for electropolymerization resulted in very low currents that did not increase with successive scans as observed for thiophene polymerization, and no visual evidence of polymer deposition. The undesired isomer of the monomer thus appears to inhibit polymer deposition.

Scheme 2. Synthesis of 3-methyl-4-pyrrolylcarboxylic acid for electropolymerization. The undesired pathway leading to 4-methyl-2-pyrrolylcarboxylic acid is highlighted in red below the desired sequence.

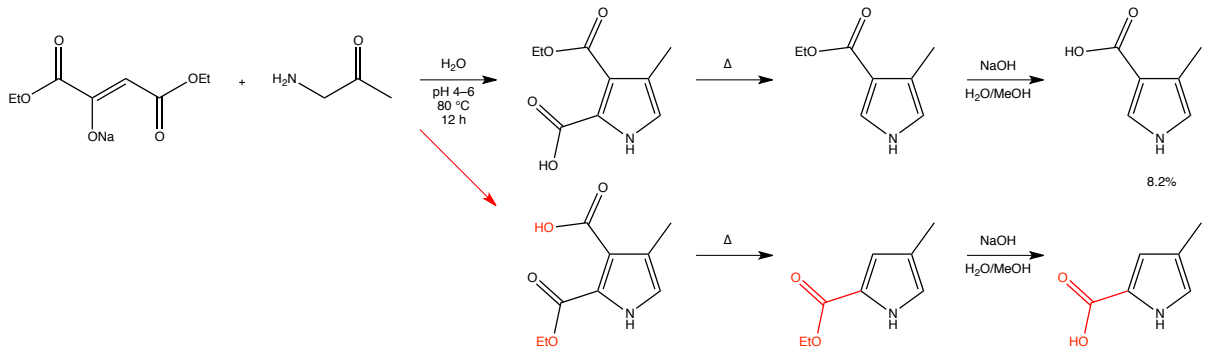

3.5.4 Characterization of anchored species

Since the best film quality was obtained for poly(3-thiophenebutyric acid) on gold, this candidate was characterized in the greatest detail. XPS revealed only a very weak Co signal on the surface of the polymer, suggesting loading is very low. It is also possible that

loading is lower at the surface (XPS probes approximately 10 nm), which in turn would suggest the film is unstable with respect to desorption of anchored Co.

XAS on the Co@COOH-polythiophene sample is consistent, as with results in previous sections, with decomposition of Co_4O_4 relative to complex **2** (Figure 11).

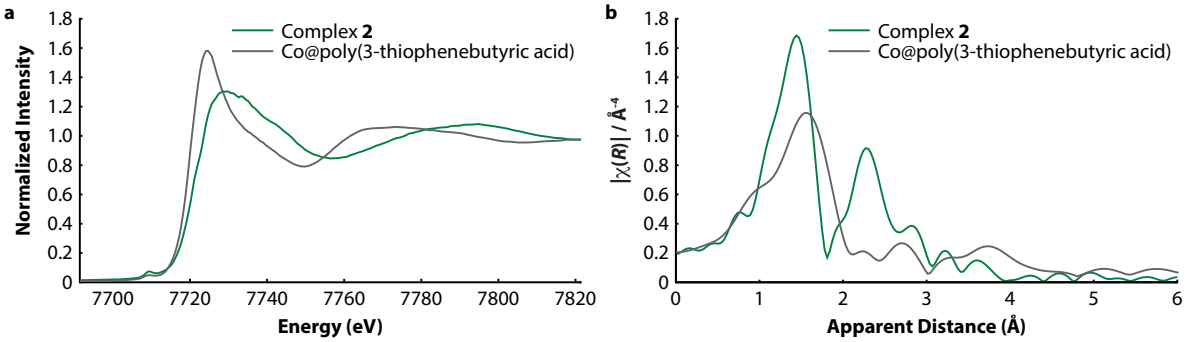

Figure 11. Co K-edge absorption spectra of Co@poly(3-thiophenebutyric acid) on Au samples (grey), showing clear decomposition of Co_4O_4 units relative to complex **2** (green): a) XANES and b) FT-EXAFS.

3.5.5 Discussion

Electropolymerization of functionalized monomers to generate a conductive, immobilization-ready film on an electrode remains an attractive strategy for generation of electrode-bound metal clusters. The reasons for poor binding, as revealed by XPS, of complex **2** on the polythiophene films described here are not clear, nor are the exact processes that might cause the surface species to exhibit different oxidation state and coordination environment than the precursor, as XAS reveals. One pitfall of this approach that was not confronted directly because of the negative anchoring results is the dependence of the conductivity of these polymers on their oxidation and protonation states. Under certain conditions, observation of the redox wave for a bound cluster might be difficult, making turnover determination difficult even if catalysis occurs when larger potentials (at which the polymer conducts) are applied.

3.6 Conclusions

Tracing the common themes in this work, including unpredictable surface functionalization with linkers and repeated XAS evidence of isolated Co(II), rather than $Co(III)_4O_4$ units, provides some insight to the approach overall and to future work. First, a key element that was not explored here is the protonation state of surface-bound ligands (or the pH at which aqueous anchoring methods are performed). It is possible that anchoring, for which the rate of reaction is of key significance, would proceed more quickly at surface-bound carboxylates than at carboxylic acids, for example. It might also be more conducive to

anchoring of intact Co_4O_4. Second, many new or adapted procedures were used, such as performing a MWCNT coupling with a diazonium salt containing a carboxylic acid, or anchoring silanes on FTO, that might be worthy of more thorough evaluation and, if successful, optimization on their own. Third, Co(II) impurities appear pervasive in the chemistry of complex **2** and related molecules. Clear evidence of Co(II) from XAS is hard to rationalize, since all previously described procedures for purifying complex **2** (column chromatography and EDTA treatment)[12] were carefully followed. It is possible that purified samples of complex **2** may decompose under the reaction conditions used for anchoring, thus generating Co(II) *in situ*. Mononuclear Co(II) is expected to be significantly more labile than complex **2**'s Co(III) centers, so it may saturate available binding sites before the desired linkage takes place. This possibility could be addressed by adding a chelating resin to the reaction mixture. Fourth, condensation of COOH groups may take place, especially in the TCO-linker films and electropolymers, eliminating binding sites for complex **2**. An approach that could address this problem is dilution of the functionalized linker or monomer with an unfunctionalized version. However, this proposal would require careful control of stoichiometry, as the various linkers/monomers would be likely to react at different rates.

While the efforts undertaken in this chapter did not yield a robust, electrode-bound M_4O_4 cubane structure for facile electrochemistry and catalysis, they did provide substantial lessons in the challenges of immobilization and materials characterization. These lessons were used in the development of coordination polymers containing Co_4O_4, which realize many of the goals that motivated this work. Those coordination polymers are the subject of the next chapter.

3.7 Acknowledgements

The author thanks Eitan Anzenberg, Walter Drisdell, and Junko Yano for assistance in performing XAS on the anchored samples, Wenjun Liu for preparing functionalized glassy carbon electrodes, Raffaella Buonsanti for providing *nano*ITO films, Alex Krawicz for advice on TCO surface preparation and characterization, and Francesca Toma for advice on functionalizing MWCNTs. This material is based upon work performed by the Joint Center for Artificial Photosynthesis, a DOE Energy Innovation Hub, supported through the Office of Science of the U.S. Department of Energy under Award Number DE-SC0004993. The author acknowledges support from a National Science Foundation Graduate Research Fellowship under Grant No. DGE-1106400. The Advanced Light Source is supported by the Director, Office of Science, Office of Basic Energy Sciences, of the U.S. Department of Energy under Contract No. DE-AC02-05CH11231.

3.8 Experimental Details

General procedures. Reagents were purchased from commercial sources in 95% or higher purity and used without further purification, except where noted. Sonication was performed using a VWR brand bath sonicator at or near room temperature. *Nano*ITO was

prepared as described previously.[23,24] Attempted synthesis of 3-methyl-4-pyrrolylcarboxylic acid followed the literature procedure.[71] Complex **1** was synthesized and purified as described in Chapter 1. Complex **2** was synthesized and purified (including column chromatography and a final treatment with EDTA) as previously described to remove Co(II) impurities.[12]

Glassy carbon functionalization. 4-Phosphonobenzenediazonium was generated and used *in situ* by adding 25 μL of aqueous $NaNO_2$ stock solution (1.0 M) into an aqueous solution of 4-aminophenylphosphoric acid (1.1 mM) and HCl (0.5 M) at 0 °C, and was not isolated as a solid. This acidic solution containing the corresponding diazonium salt, after being stirred at 0 °C for 10 minutes, was used directly as the electrolyte solution for the electrochemical functionalization of glassy carbon electrodes. Glassy carbon electrodes were prepared by polishing with 5 and 0.3 μm alumina and sonication in deionized water for 5 minutes. The surface modification of these bare electrodes was conducted by three potential cycles between 0.54 and –0.8 V (*vs.* Ag/AgCl) in the above-prepared acidic, diazonium-containing solution, at a scan rate of 100 mV/s. The modified glassy carbon electrodes were rinsed with deionized water, sonicated in deionized water for 5 minutes, and dried under a constant flow of nitrogen.

Anchoring of complex 1 on glassy carbon. Functionalized glassy carbon discs were soaked in a dry, degassed 5 mM hexane or acetonitrile solution of complex **1**. They were then rinsed thoroughly and stored in an inert atmosphere.

***Nano*ITO and FTO functionalization.** TCO substrates were cleaned by sonicating for 5 minutes and rinsing successively with acetone, isopropanol, and deionized water. They were then dried under a stream of nitrogen and placed in a Jelight UVO Cleaner Model 42 for 30 minutes. After cleaning, samples were immersed in linker solution or placed under vacuum within 10 minutes. Oxalic acid films were prepared by soaking *nano*ITO in a 1 M solution of the acid in acetonitrile for 20 minutes,[23,49] followed by rinsing, 5 minutes sonication, and further rinsing with acetonitrile. Sodium carboxyethylsilanetriol (CES) films were prepared by soaking FTO in a 0.5% aqueous solution of CES for 1 h, followed by rinsing, 5 minutes sonication, and rinsing with deionized water, and annealing in an oven at 110 °C for 2 h.[30,34] 2-(Carbomethoxy)ethyltrimethoxysilane (CMEMS) films were prepared by soaking FTO that had been dried under reduced pressure for 24 h in a 1 mM dry toluene solution of CMEMS.[47] The FTO was soaked at 65 °C for 24 h, then washed and sonicated with acetone, isopropanol, and water, at which point the samples were also exposed to air.

MWCNT functionalization. MWCNTs were purchased from Nanostructured & Amorphous Materials (1237YJS, 20–30 nm outer diameter, 0.5–2 μm length). MWCNTs (0.220 g, 20.8 mmol C) and 4-aminobenzoic acid (0.432 g, 3.15 mmol) were suspended in deionized water (220 mL) and sonicated for 30 min. Isopentyl nitrite (0.700 mL, 5.21 mmol) was added, and the mixture heated to 80 °C for 16 h. After cooling, the mixture was filtered and washed with water (100 mL). The filtrate was bright orange. The solid was sonicated for 30 min in methanol (50 mL) then filtered and washed with methanol (50 mL). This procedure was repeated three times, then three more times with dimethylformamide (methanol was added to speed drying after each DMF wash), and finally three more times

with methanol. The final wash was colorless. The solid collected by filtration was dried to a constant mass of 0.205 g.

Au@FTO film deposition. A 100 nm thick gold film was deposited on FTO using an Ångstrom Engineering Nexdep electron-beam deposition system at 2 Å/s.

Electropolymerization of 3-thiopheneacetic acid and 3-thiophenebutyric acid. 3-Thiopheneacetic acid was purchased from Sigma Aldrich and recrystallized twice from water before drying under reduced pressure.[68] 3-Thiophenebutyric acid was purchased from Rieke Metals. Electropolymerizations were performed in dry, degassed acetonitrile containing 100 mM NBu_4PF_6 and 1 M 3-thiopheneacetic acid or 100 mM 3-thiophenebutyric acid. Cyclic voltammetry scans were performed from 0 to 1.5 V (10 cycles at 100 mV/s) *vs.* an $Ag/AgNO_3$ reference electrode. The counter electrode was platinum mesh. Galvanostatic growth was performed at 3 mA/cm^2 until 100 mC/cm^2 of total charge had been reached, but this method yielded inferior films.

Anchoring of complex 2 on functionalized materials. Materials were soaked in a 20 mM dichloromethane solution of complex **2** for 24 h. Three or more cycles of 30 minutes sonication, rinsing, and filtering (in the case of MWCNTs) were used to remove as much physisorbed **2** as possible.

X-ray photoelectron spectroscopy. X-ray photoelectron spectra were collected using a Kratos Axis Ultra DLD system with a monochromatized Al Kα source (hν = 1486.6 eV), at power = 225 W. A pass energy for survey spectra of 160 eV and for elemental spectra of 20 eV was used. Spectra were fit using CasaXPS. Energy positions were corrected by shifting the C 1s core level position to 284.8 eV.

X-ray absorption spectroscopy. X-ray absorption spectra were taken at the Advanced Light Source (ALS) on Beamline 10.3.2. The radiation was monochromatized by a Si (111) double-crystal monochromator. The intensity of the incident X-ray (I_0) was monitored by an N_2-filled ionization chamber in front of the sample. The energy was calibrated using a glitch in I_0 relative to the absorption edge of an Mn or Co foil. All data were collected at room temperature using a quick XAS scan mode, and the data collection was carried out under the threshold of X-ray radiation damage, by monitoring with the XANES edge shift. Data reduction was performed using custom software (Matthew Markus, BL 10.3.2, ALS). Pre-edge and post-edge contributions were subtracted from the XAS spectra, and the result was normalized with respect to the edge jump.

FTIR. Grazing angle attenuated total reflection Fourier transform infrared spectroscopy (GATR-FTIR) was performed using a VariGATR accessory (Harrick Scientific) and a Bruker Vertex 70. Spectral collection used a nitrogen purge, GloBar MIR source, broadband KBr beamsplitter, and a liquid nitrogen cooled MCT detector. Background measurements were obtained from the bare Ge crystal.

Raman spectroscopy. Raman spectra were collected using a confocal Raman microscope spectrometer (LabRAM HR, Horiba Yvon Jobin) at 633 nm and laser power 0.19–3.70 mW at the objective. The spot size of the laser beam is approximately 1–2 μm. Total acquisition time per spectrum was 180 s. Using a 600 g/mm grating, the spectral

resolution is ~ 1 cm^{-1}. Spectral positions were calibrated using the 520.7 cm^{-1} band of a silicon wafer.

Preparation of TCO electrodes for non-aqueous electrochemistry. Several epoxy materials were tested to determine their resistance to acetonitrile for use as a sealant. Loctite Hysol E-30CL and E-120HP were found to be most effective. Both passed a durability test where a glass tube that had been sealed with cured epoxy was immersed in acetonitrile so that the epoxy was in direct contact with the solvent. The other side of the epoxy was then exposed to vacuum while the epoxy remained immersed for 7 days, after which there was no visible deformation of the cured epoxy for the two mentioned. E-120HP, which has a higher work life and is more viscous than E-30CL, was ultimately found most suitable because it appeared to wet the surfaces being sealed and fill gaps more readily. TCO electrodes were prepared by cutting a length of wire, affixing it to the TCO electrode using CircuitWorks CW2400 silver epoxy and allowing 45 minutes for the conductive epoxy to cure, inserting the wire into a glass tube, and applying E-120HP to completely seal the junction and glass tube opening. The sealant epoxy was allowed to cure for 24 h before use.

Cyclic voltammetry. Electrochemical characterization of anchored Co samples used a BioLogic SP-200 or SP-300 potentiostat. Solution resistance was measured before each CV scan and IR compensation set at 85% of measured value.

Thermogravimetric analysis. TGA on MWCNT samples was performed using a Thermal Analysis Q50 TGA unit under flowing nitrogen. MWCNTs were heated to 100 °C to remove solvent for one hour, then heated to 800 °C with a ramp rate of 10 °C/min. The mass fraction of COOH-MWCNT samples corresponding to the benzoic acid functional groups (FW = 121.11) was determined at 500 °C relative to a pristine MWCNT sample. Similarly, the mass fraction of Co@MWCNT samples resulting from replacement of the MWCNT-bound benzoic acid proton with $[Co_4O_4(OAc)_3(py)_4]^+$ (FW = 793.26) was determined by comparison at 500 °C to the COOH-MWCNT sample. TGA indicates 2.6–3.0% (210–250 μmol/g) loading of benzoic acid functional groups and 4.0 ± 0.4% (50 ± 5 μmol/g) loading of cobalt clusters, of which 35 ± 13% can be accounted for by physisorption of a cobalt complex or ligands derived from complex **2**.

3.9 References

(1) Fujdala, K. L.; Brutchey, R. L.; Tilley, T. D. In *Topics in Organometallic Chemistry*; Copéret, C., Chaudret, B., Eds.; Springer-Verlag: Berlin/Heidelberg, 2005; Vol. 16, pp 69–115.

(2) Brutchey, R. L.; Mork, B. V.; Sirbuly, D. J.; Yang, P.; Tilley, T. D. *J. Molec. Catal. A: Chem.* **2005**, *238*, 1–12.

(3) Brutchey, R. L.; Ruddy, D. A.; Andersen, L. K.; Tilley, T. D. *Langmuir* **2005**, *21*, 9576–9583.

(4) Ruddy, D. A.; Tilley, T. D. *Chem. Commun.* **2007**, 3350–3352.

(5) Raboin, L.; Yano, J.; Tilley, T. D. *J. Catal.* **2012**, *285*, 168–176.

(6) Rumberger, E. M. W.; Ahn, H. S.; Bell, A. T.; Tilley, T. D. *Dalton Trans.* **2013**,

42, 12238–12247.
(7) Ahn, H. S.; Yano, J.; Tilley, T. D. *ACS Catal.* **2015**, *5*, 2573–2576.
(8) McCrory, C. C. L.; Jung, S.; Ferrer, I. M.; Chatman, S. M.; Peters, J. C.; Jaramillo, T. F. *J. Am. Chem. Soc.* **2015**, *137*, 4347–4357.
(9) Chakrabarty, R.; Bora, S.; Das, B. K. *Inorg. Chem.* **2007**, *46*, 9450–9462.
(10) McCool, N. S.; Robinson, D. M.; Sheats, J. E.; Dismukes, G. C. *J. Am. Chem. Soc.* **2011**, *133*, 11446–11449.
(11) Ullman, A. M.; Liu, Y.; Huynh, M.; Bediako, D. K.; Wang, H.; Anderson, B. L.; Powers, D. C.; Breen, J. J.; Abruña, H. D.; Nocera, D. G. *J. Am. Chem. Soc.* **2014**, *136*, 17681–17688.
(12) Nguyen, A. I.; Ziegler, M. S.; Oña-Burgos, P.; Sturzbecher-Hohne, M.; Kim, W.; Bellone, D. E.; Tilley, T. D. *J. Am. Chem. Soc.* **2015**, *137*, 12865–12872.
(13) Hocking, R. K.; Brimblecombe, R.; Chang, L.-Y.; Singh, A.; Cheah, M. H.; Glover, C.; Casey, W. H.; Spiccia, L. *Nature Chem.* **2011**, *3*, 461–466.
(14) Delamar, M.; Hitmi, R.; Pinson, J.; Saveant, J. M. *J. Am. Chem. Soc.* **1992**, *114*, 5883–5884.
(15) Allongue, P.; Delamar, M.; Desbat, B. *J. Am. Chem. Soc.* **1997**, *119*, 201–207.
(16) Pinson, J.; Podvorica, F. *Chem. Soc. Rev.* **2005**, *34*, 429–439.
(17) Liu, W.; Tilley, T. D. *Langmuir* **2015**, *31*, 1189–1195.
(18) Bisht, H.; Eun, H. T.; Mehrtens, A.; Aegerter, M. A. *Thin Solid Films* **1999**, *351*, 109–114.
(19) Aouaj, M. A.; Diaz, R.; Belayachi, A.; Rueda, F.; Abd-Lefdil, M. *Mater. Res. Bull.* **2009**, *44*, 1458–1461.
(20) Lin, Y.; Kapadia, R.; Yang, J.; Zheng, M.; Chen, K.; Hettick, M.; Yin, X.; Battaglia, C.; Sharp, I. D.; Ager, J. W.; Javey, A. *J. Phys. Chem. C* **2015**, *119*, 2308–2313.
(21) Cooper, J. K.; Gul, S.; Toma, F. M.; Chen, L.; Liu, Y.-S.; Guo, J.; Ager, J. W.; Yano, J.; Sharp, I. D. *J. Phys. Chem. C* **2015**, *119*, 2969–2974.
(22) Lynch, J.; Giannini, C.; Cooper, J. K.; Loiudice, A.; Sharp, I. D.; Buonsanti, R. *J. Phys. Chem. C* **2015**, *119*, 7443–7452.
(23) Garcia, G.; Buonsanti, R.; Runnerstrom, E. L.; Mendelsberg, R. J.; Llordes, A.; Anders, A.; Richardson, T. J.; Milliron, D. J. *Nano Lett.* **2011**, *11*, 4415–4420.
(24) Milliron, D. J.; Buonsanti, R.; Llordes, A.; Helms, B. A. *Acc. Chem. Res.* **2014**, *47*, 236–246.
(25) Sheehan, S. W.; Thomsen, J. M.; Hintermair, U.; Crabtree, R. H.; Brudvig, G. W.; Schmuttenmaer, C. A. *Nat. Commun.* **2015**, *6*, 6469.
(26) Frens, G. *Nature (London), Phys. Sci.* **1973**, *241*, 20–22.
(27) Zhang, S.; Leem, G.; Srisombat, L.-O.; Lee, T. R. *J. Am. Chem. Soc.* **2008**, *130*, 113–120.
(28) Mudunkotuwa, I. A.; Grassian, V. H. *J. Am. Chem. Soc.* **2010**, *132*, 14986–14994.
(29) Bishop, L. M.; Yeager, J. C.; Chen, X.; Wheeler, J. N.; Torelli, M. D.; Benson, M. C.; Burke, S. D.; Pedersen, J. A.; Hamers, R. J. *Langmuir* **2011**, *28*, 1322–1329.
(30) Chen, Y.; Xu, P.; Liu, M.; Li, X. *Microelectron. Eng.* **2010**, *87*, 2468–2474.

(31) Jing, L.; Li, Y.; Ding, K.; Qiao, R.; Rogach, A. L.; Gao, M. *Nanotechnol.* **2011**, *22*, 505104.
(32) Liu, F.; Zhao, Q.; You, H.; Wang, Z. *Nanoscale* **2013**, *5*, 1047–1053.
(33) Sánchez-Salcedo, S.; Colilla, M.; Izquierdo-Barba, I.; Vallet-Regí, M. *J. Mater. Chem. B* **2013**, *1*, 1595–1606.
(34) González-Guerrero, A. B.; Alvarez, M.; García Castaño, A.; Domínguez, C.; Lechuga, L. M. *J. Colloid Interface Sci.* **2013**, *393*, 402–410.
(35) Schoenfeldt, N. J.; Korinda, A. W.; Notestein, J. M. *Chem. Commun.* **2010**, *46*, 1640–1642.
(36) Schoenfeldt, N. J.; Ni, Z.; Korinda, A. W.; Meyer, R. J.; Notestein, J. M. *J. Am. Chem. Soc.* **2011**, *133*, 18684–18695.
(37) Schoenfeldt, N. J.; Notestein, J. M. *ACS Catal.* **2011**, *1*, 1691–1701.
(38) Bjorkman, K. R.; Schoenfeldt, N. J.; Notestein, J. M.; Broadbelt, L. J. *J. Catal.* **2012**, *291*, 17–25.
(39) Bonitatibus, P. J.; Torres, A. S.; Kandapallil, B.; Lee, B. D.; Goddard, G. D.; Colborn, R. E.; Marino, M. E. *ACS Nano* **2012**, *6*, 6650–6658.
(40) Sarmah, P.; Chakrabarty, R.; Phukan, P.; Das, B. K. *J. Molec. Catal. A: Chem.* **2007**, *268*, 36–44.
(41) Chakrabarty, R.; Das, B. K.; Clark, J. H. *Green Chem.* **2007**, *9*, 845–848.
(42) Marciniec, B.; Foltynowicz, Z.; Urbaniak, W.; Perkowski, J. *Appl. Organomet. Chem.* **1987**, *1*, 267–273.
(43) Butterworth, A. J.; Clark, J. H.; Walton, P. H.; Barlow, S. J. *Chem. Commun.* **1996**, 1859–1860.
(44) Bagwe, R. P.; Hilliard, L. R.; Tan, W. *Langmuir* **2006**, *22*, 4357–4362.
(45) Yoon, Y.-S.; Lee, B.-I.; Lee, K. S.; Heo, H.; Lee, J. H.; Byeon, S.-H.; Lee, I. S. *Chem. Commun.* **2010**, *46*, 3654–3656.
(46) Fanizza, E.; Altomare, M.; Di Mauro, A. E.; Del Sole, T.; Corricelli, M.; Depalo, N.; Comparelli, R.; Agostiano, A.; Striccoli, M.; Curri, M. L. *Langmuir* **2012**, *28*, 5964–5974.
(47) Palomaki, P. K. B.; Krawicz, A.; Dinolfo, P. H. *Langmuir* **2011**, *27*, 4613–4622.
(48) Garcia, G.; Buonsanti, R.; Llordes, A.; Runnerstrom, E. L.; Bergerud, A.; Milliron, D. J. *Adv. Opt. Mater.* **2013**, *1*, 215–220.
(49) Tsai, T.-H.; Wu, Y.-F. *Microelectron. Eng.* **2006**, *83*, 536–541.
(50) Linford, M. R.; Chidsey, C. E. D. *J. Am. Chem. Soc.* **1993**, *115*, 12631–12632.
(51) Linford, M. R.; Fenter, P.; Eisenberger, P. M.; Chidsey, C. E. D. *J. Am. Chem. Soc.* **1995**, *117*, 3145–3155.
(52) Krawicz, A.; Yang, J.; Anzenberg, E.; Yano, J.; Sharp, I. D.; Moore, G. F. *J. Am. Chem. Soc.* **2013**, *135*, 11861–11868.
(53) Cedeno, D.; Krawicz, A.; Doak, P.; Yu, M.; Neaton, J. B.; Moore, G. F. *J. Phys. Chem. Lett.* **2014**, *5*, 3222–3226.
(54) Cedeno, D.; Krawicz, A.; Moore, G. F. *Interface Focus* **2015**, *5*, 20140085.
(55) Tasis, D.; Tagmatarchis, N.; Bianco, A.; Prato, M. *Chem. Rev.* **2006**, *106*, 1105–

1136.
(56) Bahr, J. L.; Tour, J. M. *J. Mater. Chem.* **2002**, *12*, 1952–1958.
(57) Kooi, S. E.; Schlecht, U.; Burghard, M.; Kern, K. *Angew. Chem. Int. Ed.* **2002**, *41*, 1353–1355.
(58) Strano, M. S.; Dyke, C. A.; Usrey, M. L.; Barone, P. W.; Allen, M. J.; Shan, H.; Kittrell, C.; Hauge, R. H.; Tour, J. M.; Smalley, R. E. *Science* **2003**, *301*, 1519–1522.
(59) Georgakilas, V.; Kordatos, K.; Prato, M. *J. Am. Chem. Soc.* **2002**, *124*, 760–761.
(60) Kamaras, K.; Itkis, M. E.; Hu, H.; Zhao, B.; Haddon, R. C. *Science* **2003**, *301*, 1501–1501.
(61) Pénicaud, A.; Poulin, P.; Derré, A.; Anglaret, E.; Petit, P. *J. Am. Chem. Soc.* **2005**, *127*, 8–9.
(62) Toma, F. M.; Sartorel, A.; Iurlo, M.; Carraro, M.; Pietro Parisse; Maccato, C.; Rapino, S.; Gonzalez, B. R.; Amenitsch, H.; Da Ros, T.; Casalis, L.; Goldoni, A.; Marcaccio, M.; Scorrano, G.; Scoles, G.; Paolucci, F.; Prato, M.; Bonchio, M. *Nature Chem.* **2010**, *2*, 826–831.
(63) Schmidt, G.; Gallon, S.; Esnouf, S.; Bourgoin, J. P.; Chenevier, P. *Chem. Eur. J.* **2009**, *15*, 2101–2110.
(64) Rasmussen, S. C.; Pickens, J. C.; Hutchison, J. E. *Macromolecules* **1998**, *31*, 933–936.
(65) Rasmussen, S. C.; Pickens, J. C. *Chem. Mater.* **1998**, *10*, 1990–1999.
(66) Bäuerle, P.; Gaudl, K. U.; Würthner, F.; Sariciftci, N. S.; Mehring, M.; Neugebauer, H.; Zhong, C.; Doblhofer, K. *Adv. Mater.* **1990**, *2*, 490–494.
(67) Li, F. B.; Albery, W. J. *Langmuir* **1992**, *8*, 1645–1653.
(68) Bartlett, P. N.; Dawson, D. H. *J. Mater. Chem.* **1994**, *4*, 1805–1810.
(69) Tóth, P. S.; Janáky, C.; Hiezl, Z.; Visy, C. *Electrochimica Acta* **2011**, *56*, 3447–3453.
(70) Cooper, J. M.; Morris, D. G.; Ryder, K. S. *J. Chem. Soc., Chem. Commun.* **1995**, 697–698.
(71) Ryder, K. S.; Morris, D. G.; Cooper, J. M. *Langmuir* **1996**, *12*, 5681–5688.
(72) Lancaster, R.; VanderWerf, C. *J. Org. Chem.* **1958**, *23*, 1208–1209.
(73) Bonnett, R.; Hamzetash, D.; Vallés, M. A. *J. Chem. Soc., Perkin Trans. 1* **1987**, 1383–1388.

Chapter 4

Tunable, Site-Isolated Co_4O_4 Oxygen-Evolution Catalysts Uniformly Dispersed Within Porous Frameworks[1]

4.1 Introduction

The modern lifestyle, with cheap, ubiquitous energy and goods supplied by petrochemical industry, requires transition metal-catalyzed chemical transformations at massive scale. With mounting evidence of this scheme's unsustainability, the need for efficient, durable, and low-cost catalysts has never been greater.

Heterogeneous catalyst materials, e.g. oxide thin films, uniquely satisfy the demanding requirements of systems for clean energy storage such as artificial photosynthesis, but the path to new and improved heterogeneous catalysts is scarcely clearer than it was fifty years ago. Since 1965, structural characterization tools (e.g. x-ray absorption and photoelectron spectroscopies (XAS and XPS), synchrotron light sources, electron paramagnetic resonance (EPR) spectroscopy) and deposition methods (e.g. sputtering, electron beam, electrochemical) have become widespread, even routine. Despite this progress, understanding of key topics, like the role of impurities in catalysis[2-8] and the evolution of molecular catalysts during water oxidation, has only recently emerged.[9-14] The most critical knowledge, namely how catalytic materials function and how they can be improved, remains elusive.

Much has been made of the insights that coordination complex models can provide in improving bulk catalyst materials. However, despite immense effort in this area, model complexes often bear limited resemblance to the materials on which they are based, even assuming (often rather boldly) that the important features of the latter are more or less known.

To proceed in light of these limitations, an extraordinary class of materials recommends itself: three-dimensional coordination polymers, more recently entitled metal-organic frameworks or MOFs.[15,16] The still-exploding scientific interest in these materials stems from their elegant union of molecular properties, such as a defined environment and straightforward tuning, with bulk material properties, such as durability. Moreover, the porous nature of many MOFs reduces or eliminates the significance of surface/bulk and active/passive distinctions in catalysis, because the metal sites are identical and accessible, throughout the material.

Cobalt-oxo cubane complexes, especially $Co_4O_4(py)_4(OAc)_4$ (**1**), are attractive building blocks for polymers, with two types of ligands for geometrical and electronic versatility. Recent studies on Co_4O_4 have already revealed detailed information on the criteria for efficient catalysis.[17] While an example of an OER catalyst appended onto the linker of a framework structure exists,[18] no example of a framework material with intrinsic OER activity has been reported; this latter structure would significantly higher catalyst loading by mass. Thus, the Co_4O_4 system is ideal for testing whether the reactivity and mechanism of molecular OER catalysts can be directly translated into heterogeneous materials.

This chapter describes a series of MOFs that we believe to be the first such structures to contain structurally characterized Co_4O_4 units. Thoroughgoing structural analysis informs conclusions about the relevance of the new materials to improved catalysis, despite the absence of long range crystallographic order that would ordinarily be used for MOF

materials. Results from XAS, EPR, XPS, and other methods are described. Finally, the MOF materials are shown to reproduce chemistry of discrete Co_4O_4 complexes, access new chemistry, and oxidize water both stoichiometrically and electrocatalytically.

4.2 Results and Discussion

4.2.1 Synthesis & physical properties of Co_4O_4 coordination polymers

All materials were synthesized in a single step by heating the parent cubane, $Co_4O_4(OAc)_4py_4$ (**1**), with an appropriate linker. The syntheses of Co_4O_4 coordination polymers bridged by carboxylate-based linkers were achieved (Scheme 1) by heating a solution of $Co_4O_4(OAc)_4py_4$ (**1**) with stoichiometric amounts of either 1,3,5-benzenetricarboxylic acid (H_3BTC) or 1,3,5-benzenetribenzoic acid (H_3BTB) at 60 °C in methanol. After stirring for 1.5 h, **Co_4-BTC** and **Co_4-BTB** were isolated by filtration as green powders. Analogously, syntheses of Co_4O_4 coordination polymers bridged by pyridyl-based linkers were achieved by heating a solution of **1** with stoichiometric amounts of either 2,4,6-tris(4-pyridyl)triazine (TPT), 2,4,6-tris(4-pyridyl)pyridine (TPP), or 2,4,6-tris(4-pyridyl)benzene (TPB) in benzonitrile at 90–100 °C. To provide a driving force for these reactions, active vacuum was applied to remove pyridine by distillation as it was released from **1**. The resulting solids **Co_4-TPT**, **Co_4-TPP**, and **Co_4-TPB** were isolated by filtration. The proposed structures for these solids are shown in Chart 1. **Co_4-TPT** is a dark-red solid, **Co_4-TPP** is red-brown, and **Co_4-TPB** is dark green. Diffuse-reflectance UV-visible absorbance spectra of these solids is dominated by two strong bands, similar to that of the molecular cubane, **1** (Figure 1A). The band at longer wavelength likely originates from the $^1A_1 \rightarrow {}^1T_1$ *d-d* transition of the low-spin, pseudo-O_h cobalt(III) centers.[19] This transition in **Co_4-TPB**, **Co_4-TPP**, and **Co_4-TPT** occurs at ~700 nm, 650 nm, and 600 nm, respectively. The blue-shifting of the band signifies an increasing t_{2g}-e_g gap correlated with the increasing π-acidity traversing from TPB to TPP to TPT. In **Co_4-BTC** and **Co_4-BTB**, this transition is blue-shifted relative to that of **1**; in this case the weaker σ-donation of the aryl-carboxylate ligands relative to that of acetate also results in a diminished t_{2g}-e_g gap. These color differences offer a first glimpse at the electronic tunability of these materials.

Scheme 1. Two routes for synthesis of cubane-derived MOFs

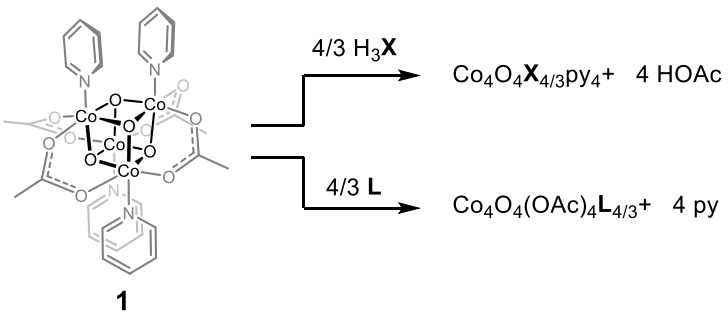

Chart 1. Proposed structures of (A) polymers synthesized by carboxylate exchange, and (B) polymers synthesized by pyridine exchange.

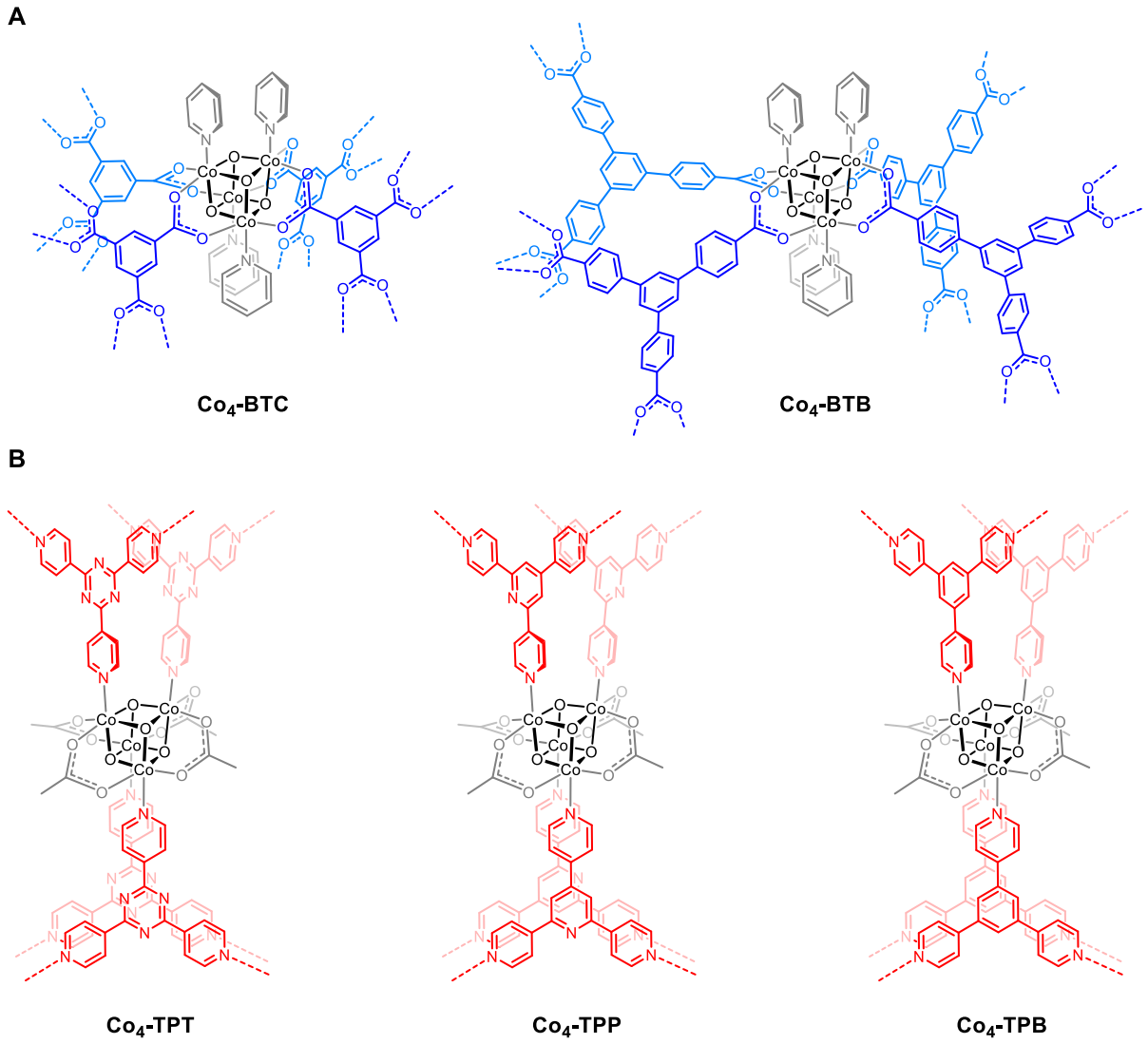

The polymers were further purified of any Co(II) formed during the synthesis by stirring in water with an Empore SPE chelating membrane (see experimental section). Elimination of Co(II) impurity is a crucial step for investigations into the inherent OER activity of any new Co OER catalyst.[5] The physical separation of the membrane from the coordination polymer avoids the modification of the polymer surface that would be possible with EDTA or a similar reagent, while still allowing the sequestration of any leached metal ions. Indeed, the Empore SPE membrane turned a strong pink color after stirring for 5 days in the presence of each polymer, indicating adsorption of leached Co(II) ions (see experimental section). This process was repeated until no pink color was observed on the chelating membrane, demonstrating that all soluble forms of Co(II) had been removed from

the polymer. This decrease in Co(II) capture over time also demonstrates that Co(II) does not originate from cubane degradation. An alternative purification method found to provide material of similar purity is Soxhlet extraction in methanol over 16 h. This method is significantly faster than the chelation method and also produces material that is free of Co(II), as evidenced by the absence of any pink color in an Empore membrane when the Soxhlet-treated solids were stirred for five days together with the membrane.

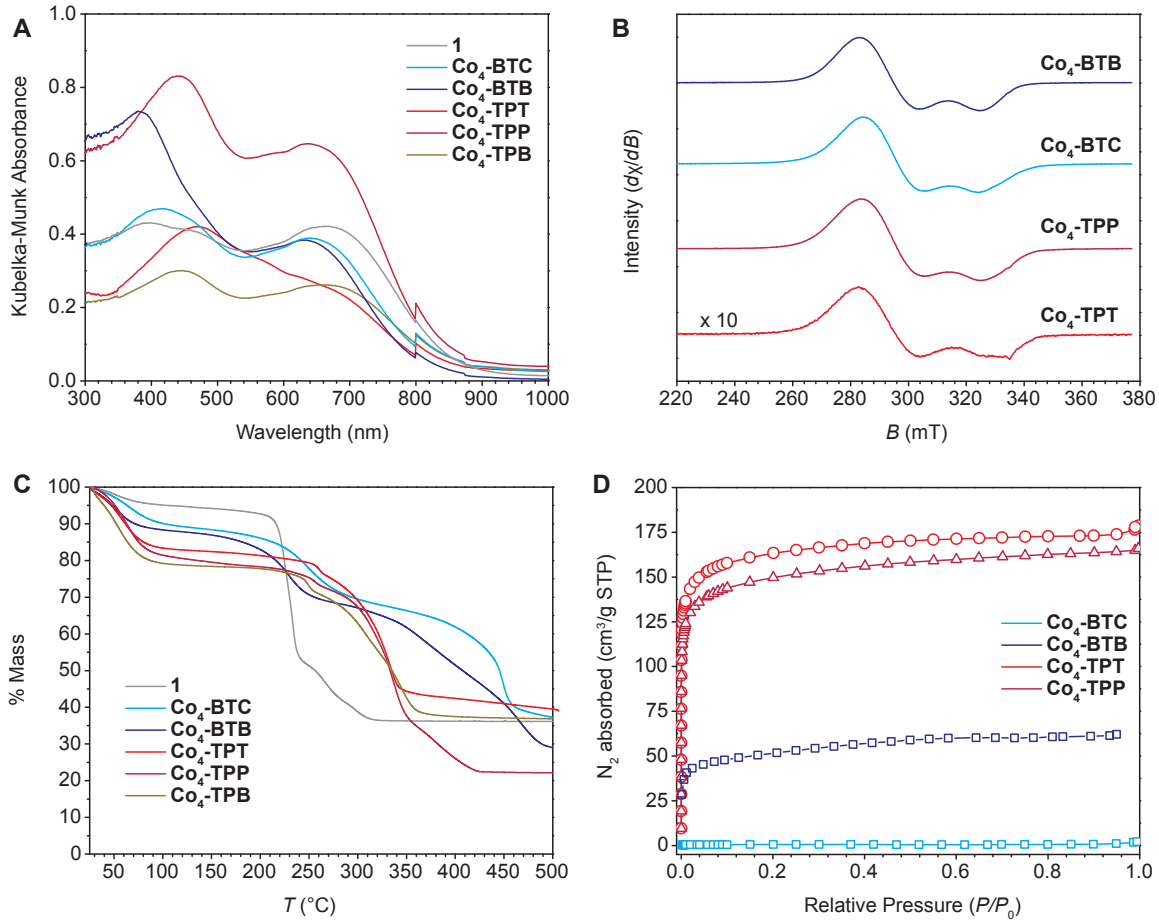

Figure 1. Characterization of Co_4O_4 polymers, with complex **1** for comparison: (A) diffuse reflectance ultraviolet/visible absorbance spectra, (B) electron paramagnetic resonance spectra (microwave frequency = 9.39 GHz, power = 1.19 mW, modulation amplitude = 4 G, modulation frequency = 100 kHz), (C) thermogravimetric analysis under flowing N_2 (heat rate = 10 °C/min), (D) nitrogen adsorption isotherms.

4.2.2 Structural characterization (molecular & macromolecular)

The empirical formulations of these materials were determined by a combination of ^{1}H NMR spectroscopy on acid-digested samples and combustion elemental analysis (EA).

The relative ratios of ligands were determined using the integrated intensities of their ^{1}H NMR signals, after digestion in 37% DCl in D_2O. For digested **Co_4-TPT**, **Co_4-TPP**, and **Co_4-TPB**, only the pyridyl-linker and acetic acid were observed in ^{1}H NMR spectra, indicating that all pyridine ligands of **1** were replaced in the synthesis. The molar ratios of the pyridyl-linkers to acetate gave empirical formulas of 1.89, 2.34, and 1.34, for **Co_4-TPT**, **Co_4-TPP**, and **Co_4-TPB**, respectively (see experimental section). These ratios are slightly higher than the ideal stoichiometric ratio of 1.33. Combustion EA of the materials also were consistent with the NMR integration of the respective digested samples. Trapped free ligand is an unlikely source of the observed stoichiometric excess, since the materials were purified by Soxhlet extraction with methanol, in which all linker ligands are soluble, prior to analysis. These observations suggest that the average domains of **Co_4-TPT**, **Co_4-TPP**, and **Co_4-TPB** must be small, and thus the edge sites, which are capped by extra-stoichiometric linker ligands, contribute significantly to the overall stoichiometry of these materials. For **Co_4-BTC** and **Co_4-BTB**, the BTC/py and BTB/py molar ratios were both 1.47, slightly larger than the ideal 1.33.

Retention of the reactivity and structure associated with the Co_4O_4 unit in the polymers was probed *via* chemical oxidation (Scheme 2). For reference, the molecular cubane **1** is reported to have a reversible $[Co_4O_4]^{4+}/[Co_4O_4]^{5+}$ redox event, [5,17] and the oxidized form, **1**$^+$, was synthesized by chemical oxidation using ceric ammonium nitrate and studied by EPR spectroscopy.[20] The polymers stirred with aqueous ceric ammonium nitrate for 1 h reproduced the signature EPR spectrum of **1**$^+$, providing preliminary evidence for the presence of Co_4O_4 units, and that the materials retained the redox chemistry of their molecular analogue (Figure 1B).

Scheme 2. Representative oxidation of the materials (e.g. **Co_4-TPP**) by Ce(IV).

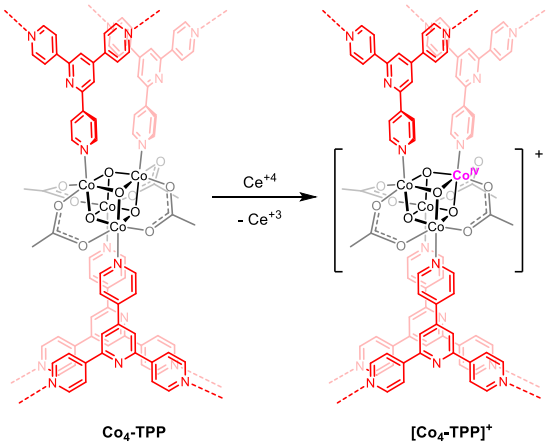

Porosity and surface area of the polymers were estimated by BET (Brunauer-Emmett-Teller) analysis of the N_2 adsorption isotherms of the solvent-free materials. These surface areas are measured for the solvent-free materials, which were prepared by heating under vacuum for 12 h. An ideal porous material will display *permanent* porosity, that is, no

collapse of the pores occurs upon solvent removal, but many porous materials demonstrate a lower-than-expected measured surface area due to partial or total framework collapse during this drying process.[21] While permanent porosity is necessary for applications such as gas separations, it is not required for chemistries in solution. Nonetheless, N_2 adsorption isotherms can provide a lower-bound estimate of pore structure and surface areas for these materials. To determine the ideal temperature for solvent removal, thermogravimetric analyses (TGA) were performed. TGA of all the solids showed a significant mass loss (12-22%) at low temperature (60-100˚C), consistent with a large amount of methanol solvent associated within the materials' pores as synthesized (4 to 9 mol MeOH per mol Co_4O_4, see experimental section) (Figure 1C). The magnitude of this mass loss is typical of what has been observed for many porous metal-organic frameworks.[22] After solvent removal, all solids appear stable up to 200–250˚C. **Co_4-BTC** is essentially nonporous with a low BET surface area of S_{BET} = 1.7 m^2/g. The replacement of BTC^{3-} with the isosymmetric, but larger BTB^{-3} linker (in **Co_4-BTB**) produced a type I adsorption isotherm, indicative of a microporous material. Correspondingly, the surface area increased dramatically to S_{BET} = 177 m^2/g. **Co_4-TPT** and **Co_4-TPP** exhibited microporosity and high surface areas of 480 m^2/g and 530 m^2/g, respectively. Interestingly, **Co_4-TPB**, which exhibits a thermogravimetric solvent loss similar to that of its isoreticular homologues, **Co_4-TPT** and **Co_4-TPP**, lacks permanent porosity, as demonstrated by a low surface area of S_{BET} = 11 m^2/g. This low surface area suggests that the pores collapse upon solvent removal.

These materials lack long-range periodicity, as demonstrated by the absence of Bragg diffraction peaks in the powder x-ray diffraction pattern. The lack of long-range order is also consistent with the small domains implicated by the empirical formula. Scanning electron microscopy (SEM) images (Figure 2) do not reveal crystalline facets, though interestingly, **Co_4-BTC** formed monodisperse ~3 μm diameter spheres (see experimental section). Synthetic efforts to improve crystallinity using higher temperatures, longer reaction times, different solvents, and slow diffusion of reactants were unsuccessful. The difficulty in obtaining crystalline material is attributed to low reversibility of the reaction arising from the sluggish ligand exchange kinetics inherent in the t_{2g}^6 electron configuration of Co(III) ions of the cubane.[23] Attempts to overcome the exchange kinetics with higher temperatures, longer reaction times, or acid led to reduction of Co(III) to Co(II) as evidenced by formation of purple or pink solids and solutions.

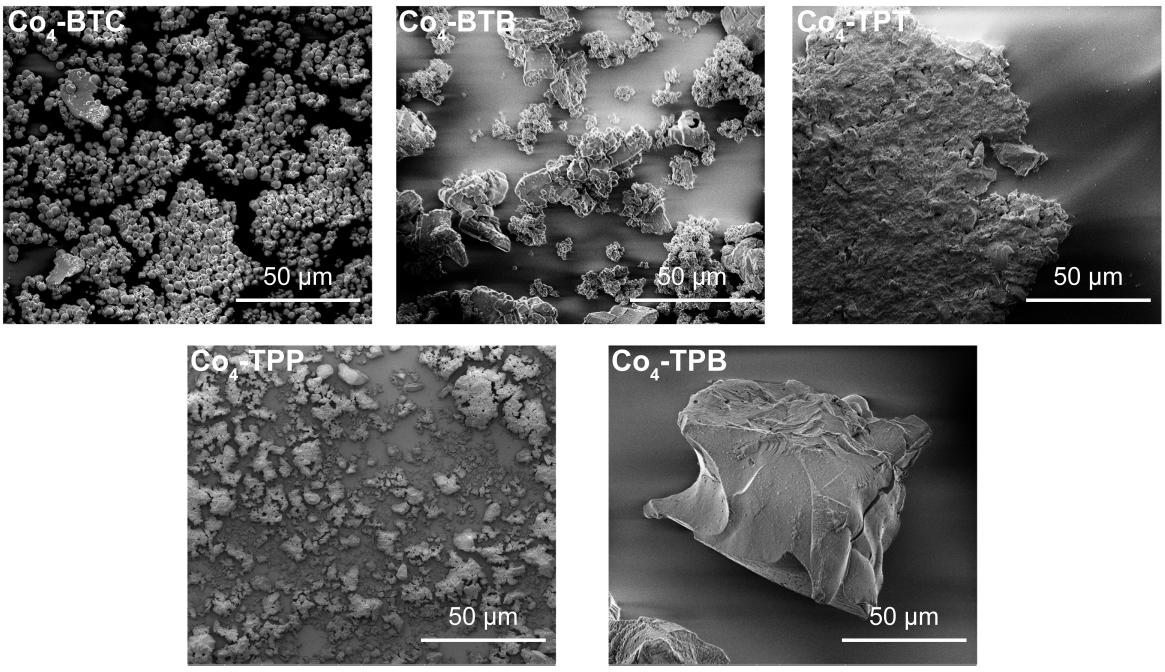

Figure 2. SEM images of materials obtained directly from synthesis.

While structures of most crystalline materials are easily modeled solely through the use of X-ray crystallography, structural solutions for less crystalline materials are achieved *via* refinement of a model against several measurements and observations. A structural solution of these materials must be consistent with all the following observables: (1) the stoichiometry, (2) the identity and structure of the individual building unit(s), and (3) the arrangement of these building units into an extended framework. Stoichiometry and identity of ligands have already been established by combustion EA and NMR spectroscopy. The next step in structural interrogation is direct observation of Co_4O_4 building units.

X-ray absorption spectroscopy (XAS) at the Co K-edge was used to identify intact Co_4O_4 units within the framework materials. This technique has been used previously for the Photosystem II active site,[24-29] the cobalt oxide water-oxidation catalyst,[30,31] and Mn-oxo cubanes.[32-35] The X-ray absorption near edge structure (XANES) part of each spectrum provides an element-specific probe of the oxidation state of the Co centers in the framework materials, while the extended X-ray absorption fine structure (EXAFS) part of the spectrum is sensitive to the local atomic structure within ~ 5 Å of the excited Co atoms. This makes XAS an ideal technique to probe the specific coordination of the Co centers in the framework materials and determine whether the Co_4O_4 units are intact. Results from XANES spectroscopy demonstrate that the oxidation state of Co(III) from $Co_4O_4(OAc)_4(py)_4$ (**1**) is preserved in the new materials (Figure 3A). Results from extended X-ray absorption fine structure (EXAFS) spectroscopy reveal that both the first (Co-O, Co-

N) and second (Co-Co, Co-C, etc.) nearest-neighbor peaks are similar in the molecular species and the materials (Figure 3B).

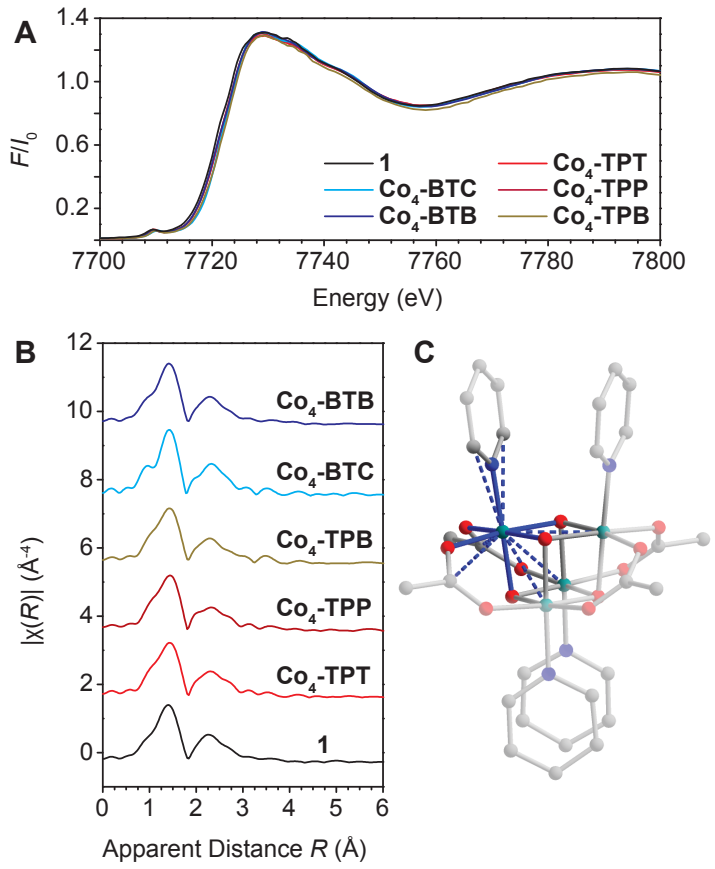

Figure 3. (A) Co K-edge absorption spectra, comparing polymers (colored) to complex **1** (black). (B) Fourier transformed EXAFS spectra. The spectra are vertically stacked for clarity, and thus the *y*-axis values are relative. (C) The XRD structure of 1 used as a model for EXAFS spectra fitting. The blue lines, solid and dashed, represent the Co-containing scattering paths used in the fit.

A description of these materials would be incomplete without information on their extended framework and pore structure. For materials without observable Bragg diffraction, analysis of diffuse X-ray scattering *via* its Fourier transform, the pair distribution function (PDF), provides substantial information on their metrical parameters.[36-38] Like EXAFS, PDF presents structural information as a histogram of interatomic distances. EXAFS does so with elemental specificity and provides highly local information. Conversely, PDF is not specific to a particular element and its local environment but probes *all* interatomic pairs, and thus it can be used to elucidate the extended structure.

Experimental data from X-ray scattering and PDF analysis must be compared to calculated data from a three-dimensional structural model, much like that used in X-ray crystallography. In this case, however, the models must be generated *a priori*, as the spherically averaged experimental PDF data does not contain sufficient information to "solve" the structure directly.

The three-dimensional models for correlation with PDF data were assembled as follows: atomic coordinates from the crystal structure of molecular analogue **1** were placed at appropriate sites of candidate framework structures, linker atoms were added, and the structures were optimized using density functional theory (DFT) with periodic boundary conditions. Candidate structures were determined by comparing cubane and linker symmetry to known framework structures in the Reticular Chemistry Structure Resource (RCSR).[39] Complex **1** has idealized D_{2d} site symmetry (neglecting acetate methyl groups), where κ^2-carboxylates cap four equatorial faces (~90˚ apart) and pyridine ligands cap the two remaining, opposite faces (180˚ apart) of the cubane. The BTC and BTB linkers have idealized D_{3h} symmetry, which is expected to reduce to D_3 in the **Co$_4$-BTC** and **Co$_4$-BTB** polymers because the cubane units cannot be arranged to maintain the mirror planes in D_{3h}. The structures compatible with these requirements are **pto**[40] and **tbo**[40] (see experimental section for details). These abbreviations refer to specific, known topologies from previously characterized solid-state materials (*e.g.* **pto** is derived from, and named for, the coordination network of crystalline Pt_3O_4). In the case of **tbo** (*Fm*-3*m*), the formal crystallographic symmetry of the net – *mmm* (D_{2h}) for four-coordinate sites and 3*m* (C_{3v}) for three-coordinate sites – is different from that expected for **Co$_4$-BTC** and **Co$_4$-BTB** and thus a "pseudo-**tbo**" structure that lacks some of the symmetry operations of *Fm*-3*m* was constructed. For **Co$_4$-TPT**, **Co$_4$-TPP**, and **Co$_4$-TPB**, the only vertex is the pyridyl linker, with idealized D_{3h} symmetry, and the edges with Co_4 cubanes have idealized D_{2d} symmetry. Searching the RCSR for structures with one three-coordinate vertex and one edge produces only the **srs**[41] net (and its interpenetrated analogues **srs-c**, **srs-c4**, and **srs-c8**). Site symmetry in **srs** (*I*4(1)32) – 32 (D_3) for vertices and 222 (D_2) for edges – is a subset of the idealized symmetry above and thus compatible. The structural models were refined by DFT in the Vienna *Ab initio* Simulation Package (VASP)[42-44] to improve the chemical soundness of their metrical parameters.

The PDF information obtained by analysis of diffuse X-ray scattering data is consistent with the structural models for all of the polymer materials. The experimental PDF results for the five materials are shown in Figure 4, including oscillations to at least 20 Å. **Co$_4$-TPT**, **Co$_4$-TPP**, and **Co$_4$-TPB** are consistent with the corresponding **srs** structural models. The calculated PDF's for **Co$_4$-TPT-srs** and **Co$_4$-TPT-srs-c** are quite similar and similarly consistent with the experimental data, but the N_2 adsorption isotherm data is more consistent with the microporous **srs-c** interpenetrated network than the mesoporous **srs** network. **Co$_4$-BTC** and **Co$_4$-BTB** experimental PDF data are consistent with pseudo-**tbo** structural models, however, the **pto** structure accessible for **Co$_4$-BTB** gives a better fit for that material. Detailed information on the PDF analysis, including structural refinements, isolation of cubane and linker contributions to the observed data, reduced structure function

data, and estimation of crystallite size, is included in the experimental section. Figure 5 shows an example of the agreement between a structural model and the experimental data for **Co_4-TPT**. Figure 6 depicts representative structures confirmed by PDF analysis.

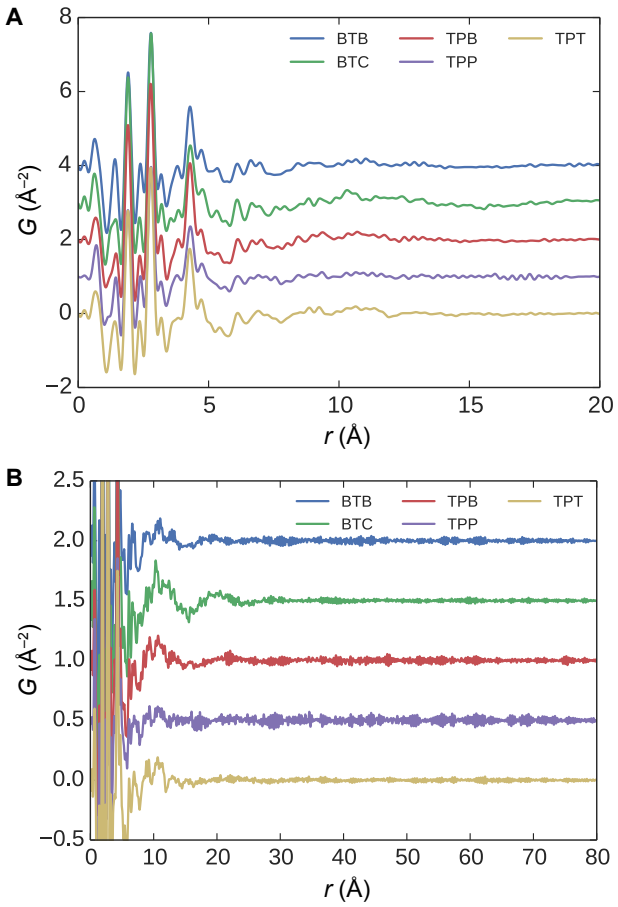

Figure 4. Experimental PDF from diffuse X-ray total scattering measurements for each of the Co polymer materials: (A) short (0–20 Å) pair range and (B) long (0–80 Å) pair range.

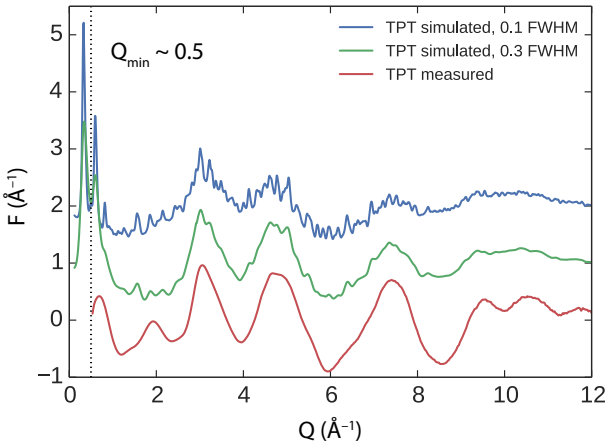

Figure 5. Comparison of experimental (red) and simulated (green, blue) structure factors for **Co_4-TPT** from diffuse X-ray total scattering measurements.

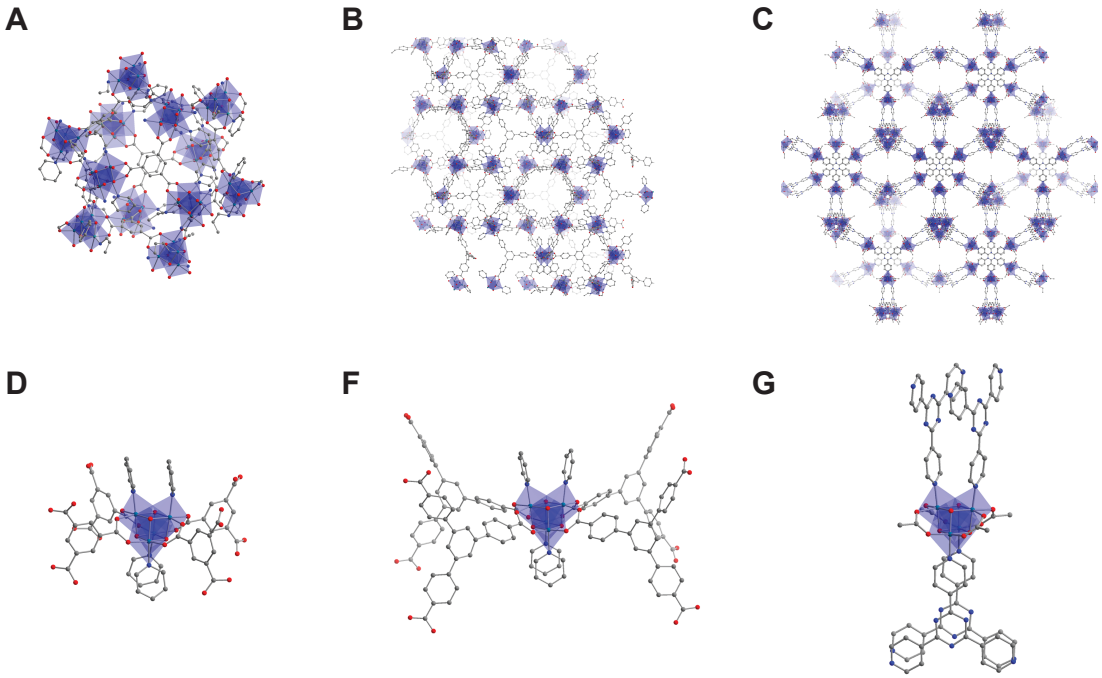

Figure 6. Representative segments of the extended structure of (A) **Co_4-BTC**, (B) **Co_4-BTB** (pseudo-**tbo** topology), and (C) **Co_4-TPT**. Building units of (D) **Co_4-BTC**, (E) **Co_4-BTB** (pseudo-**tbo** topology), and (F) **Co_4-TPT**.

Raman spectroscopy proved useful as a fingerprint identification method for the new materials. Decomposition of cubane units, when indicated by XAS, was accompanied by

substantial changes to Raman spectra. The latter was therefore used as a routine check for integrity after, for example, OER testing. Raman spectra were collected at λ = 633 nm (or 532 nm), in order to benefit from resonance with broad electronic absorption modes of **1** and all new materials. Detailed analysis, e.g. to identify common structural features of the polymers and complex **1**, was not performed with Raman spectra, as XAS and PDF analyses were found to be more suitable.

4.2.3 Stability to high pH conditions

The site-isolation of the cubane units within a rigid, porous framework results in chemical properties that are distinct from those of the molecular cubane **1**. On the basis of solution NMR studies, it has been shown that one acetate ligand of **1** is displaced by hydroxide ions at pH > 11, to generate a dicobalt *syn*-dihydroxide molecular complex (**2**).[17] Notably, this *syn*-dihydroxide motif is thought to correspond to the active site for OER as catalyzed by cobalt oxide materials.[45] However, molecular complexes **1** and **2** are unstable at higher pH, since the hydroxide ligands engage in condensation reactions that result in precipitation of CoO_x over the course of 1 h.

Spatial isolation of the cubane clusters in the rigid framework was expected to prevent unwanted Co_4O_4 aggregation, thereby stabilizing the desired, dicobalt *syn*-dihydroxide active site. Indeed, Co_4O_4 units of **Co_4-TPT**, **Co_4-TPP**, and **Co_4-TPB** remain intact after treatment at pH 14 for at least 5 h, as evidenced by XAS (Figure 7). ^{1}H NMR spectroscopy of D_2O solutions at pD 14 (1.0 M NaOD) containing suspensions of these materials showed the release of acetate ligands from the framework into solution over time, reaching 50-60% displacement after 5 h (see experimental section for details). Sodium was not detected by X-ray photoelectron spectroscopy (XPS) on the materials after the 5 h of soaking, signifying that on average, no more than four OH^- ligands bind to each Co_4O_4 site; otherwise, Na^+ would be required for charge balance. The XAS, NMR, and XPS data together suggest that each cubane unit has an approximate formulation, aside from the pyridyl linker, of $[Co_4O_4(OH)_2(H_2O)_2(OAc)_2]$ (Scheme 3). These materials are abbreviated hereafter as **Co_4O_4-TPT-OH**, **Co_4O_4-TPP-OH**, and **Co_4O_4-TPB-OH**.

Scheme 3. Reactions of polymers at pH 14.

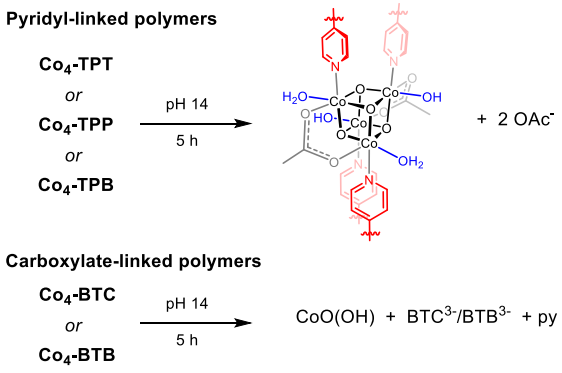

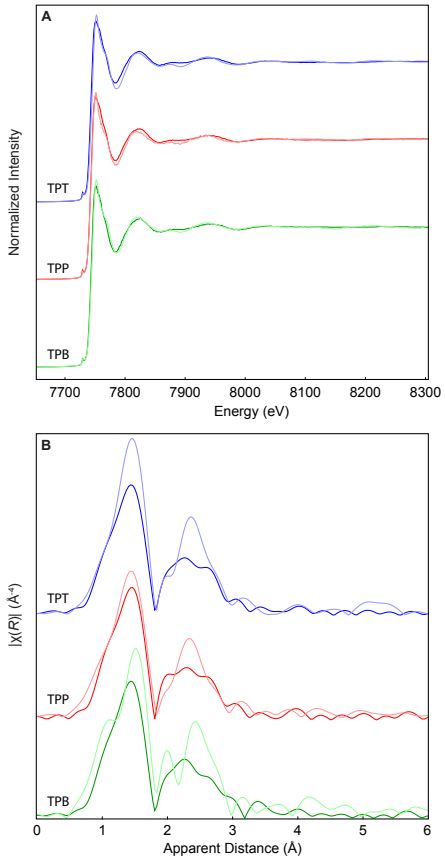

Figure 7. Comparison of **Co_4O_4-TPT**, **Co_4O_4-TPP**, and **Co_4O_4-TPB** (solid colors) to their hydroxide-exchanged analogues, **Co_4O_4-TPT-OH**, **Co_4O_4-TPP-OH**, and **Co_4O_4-TPB-OH** (light colors) by Co K-edge absorbance spectroscopy: (A) XANES and (B) FT-EXAFS.

Interestingly, the carboxylate-linked materials, **Co_4-BTC** and **Co_4-BTB**, are quite *unstable* in alkaline water (Scheme 4). **Co_4-BTC** immediately dissolves upon addition of pH 14 water, followed by precipitation of a brown solid after 1 h. For **Co_4-BTB**, EXAFS and Raman analyses confirm the absence of the Co_4O_4 cubane core, and formation of cobalt oxyhydroxide (CoOOH) after 5 h of stirring in pH 14 solution (Figure 7). These results are consistent with the previous observation that hydroxide ions displace the carboxylate ligands in preference to the pyridyl ligands of **1**,[17] which explains the rapid decomposition of frameworks built upon carboxylate linkages, **Co_4-BTC** and **Co_4-BTB**, at pH 14. The contrast in stability between the carboxylate-linked and pyridyl-linked classes showcases the power of well-defined, three-dimensional polymers, in which principles of molecular chemistry remain relevant even as favorable materials properties are achieved.

4.2.4 Stoichiometric OER by oxidized MOFs

The molecular cubane **1** has been demonstrated as a water oxidation catalyst at pH > 11, and key features of its mechanism have recently been elucidated.[17] As discussed in the previous section, **1** exhibits long-term instability at high pH due to intermolecular aggregation, but immobilization in a rigid framework greatly increases stability. Mechanistic studies on OER by **1** demonstrate that displacement of acetate by hydroxide forms the activated catalyst,[17] and therefore only the pyridyl-linked materials **Co_4-TPT**, **Co_4-TPP**, and **Co_4-TPB** can be activated by hydroxide without framework decomposition (*vide supra*). In the molecular species, OER catalysis is initiated by oxidation to **1^+** by an electrode or chemical oxidant. Analogously, **Co_4-TPT**, **Co_4-TPP**, and **Co_4-TPB** can be oxidized by ceric ammonium nitrate to form **[Co_4-TPT]$^+$**, **[Co_4-TPP]$^+$**, and **[Co_4-TPB]$^+$** (*vide supra*). Satisfyingly, addition of one equivalent of NaOH to **[Co_4-TPT]$^+$**, **[Co_4-TPP]$^+$**, and **[Co_4-TPB]$^+$** produced O_2, in 12%, 44%, and 30% yield with respect to the polymer (Figure 8A). Yields of O_2 lower than 100% and varying between the materials could result from

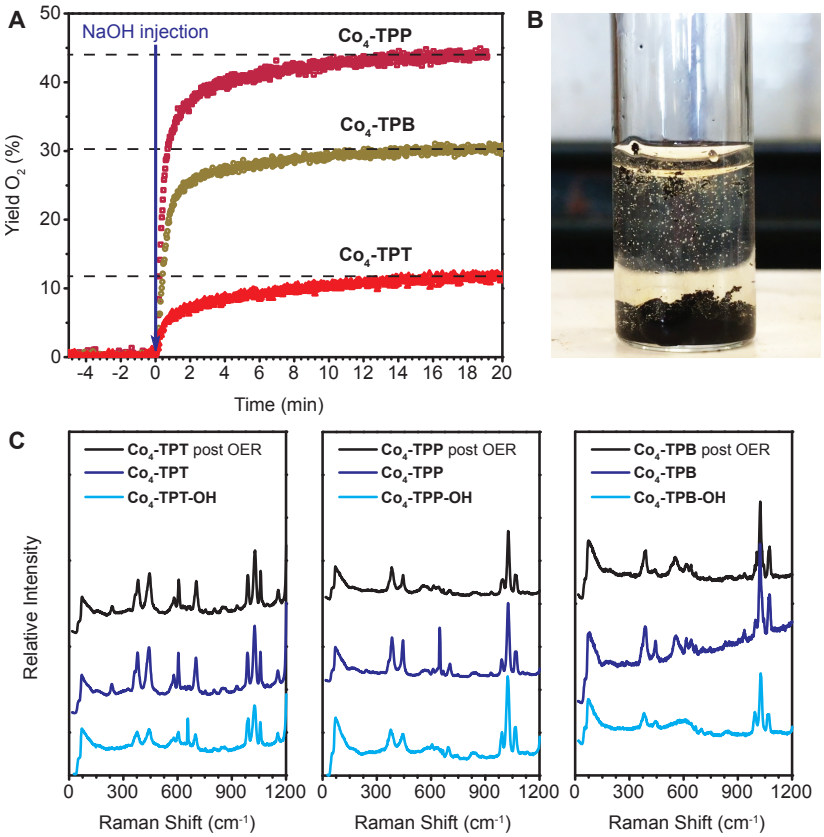

Figure 8. (A) Quantification of O_2 evolved from oxidized polymers upon addition of 1 M NaOH. (B) A photograph showing the bubbles of O_2 upon addition of 1 M NaOH to **[Co_4-TPP]$^+$**. (C) Raman spectra comparing the materials post OER to the starting polymers and the polymers treated at pH 14 for 5 h.

incomplete oxidation by Ce(IV), clogging of pores by residual Ce species (*vide infra*), or partial reduction of oxidized polymer during workup prior to hydroxide addition. Nonetheless, the stoichiometric OER experiment demonstrates the retention of molecular reactivity in heterogeneous, porous solids. Raman spectroscopy on each material after OER produced a spectrum identical to that of the starting material with some admixture of the hydroxide-exchanged material, indicating that the structure was not substantially changed by its oxidation (by Ce^{4+}) and subsequent reduction (by OH^-) (Figure 8C). The mechanism for OER is assumed to be similar to that determined for **1** (Scheme 5). The electron transfer steps would occur between oxidized cubane sites within the lattice, perhaps *via* a redox hopping mechanism. Surprisingly, attempts to reuse the material for OER proved unsuccessful. Evidence from XPS offers an explanation that may reconcile the evidence of intact **Co_4-TPT** from Raman with the reduction in activity: significant levels of cerium were detected at the surface. Clogging of porous catalysts by cerium ions or particles has been reported previously.[46,47] Even hydrated cerium (III), with a diameter of ~5 Å,[48] might be capable of blocking the average 6 Å pores of **Co_4-TPT** (*vide supra*). Moreover, at the high pH used for OER, decomposition of Ce ions to larger cerium oxide particles is likely. This result indicates that conditions that reduce or eliminate remaining chemical oxidant from the polymers before OER are needed, and therefore electrochemical OER with these materials is ultimately preferred. Nonetheless, the OER capability of **Co_4-TPT** demonstrates an unprecedented feat: OER by a porous polymeric material made from earth-abundant metals.

Scheme 5. Proposed OER mechanism by the polymers.

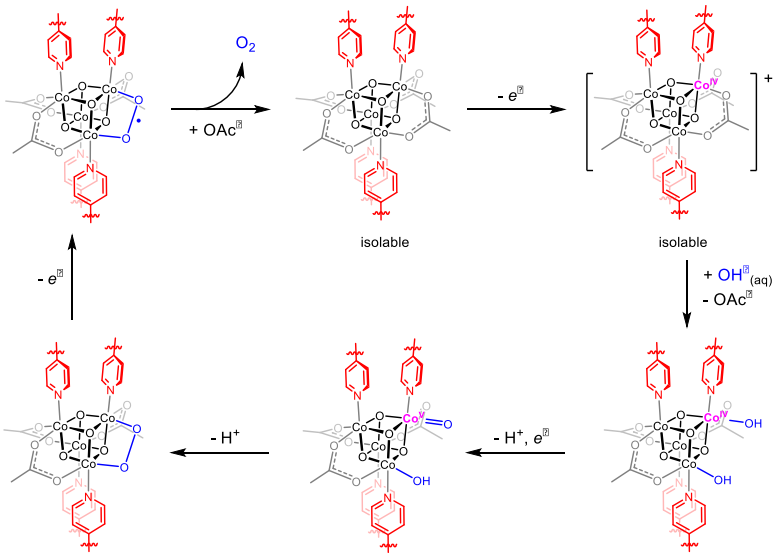

4.2.5 Electrocatalytic OER by MOFs

Electrochemistry of **Co_4-TPT**, **Co_4-TPP**, and **Co_4-TPB** revealed that both a reversible Co(III)/Co(IV) wave and electrocatalytic OER activity is preserved from complex **1**. A permanent colloid ink of each material was generated by sonication in ethanol or isopropanol. This ink was drop-cast onto a glassy carbon electrode. In our hands, **Co_4-BTC** and **Co_4-BTB** suspended poorly, and thus, no electrochemical data was obtained. Reversible Co(III)/Co(IV) waves were observed in acetonitrile with an [*n*Bu_4N]PF_6 electrolyte. The redox couples shifted towards more positive potentials moving from **Co_4-TPB** to **Co_4-TPP** to **Co_4-TPT**, following the trend of decreasing electron-donation of the pyridyl linker (Figure 9, Table 1). These redox waves displayed scan-rate dependent currents characteristic of diffusion-controlled electron-transfer (Randles-Sevcik equation);[49] this behavior is suggestive of an electron-hopping charge transport mechanism within the material under applied potential.[50] Consistent with low conductivity for these materials, the percentage of the polymer films accessed electrochemically during a CV sweep is small. At 100 mV/s, the electroactive fraction was 4.0% of **Co_4-TPT**, 5.7% of **Co_4-TPP**, and 3.2% of **Co_4-TPB** (see experimental section for calculation). This observation suggests that only the surface of the materials is electroactive on the timescale of cyclic voltammetry. In pH 7 (0.1 M KP_i buffer) aqueous solution clear redox waves were seen for **Co_4-TPP** and **Co_4-TPB** by CV (Figure 10), but peaks for **Co_4-TPT** were too broad to observe. The well-defined CVs of **Co_4-TPP** and **Co_4-TPB** with low current signal at 1300 mV vs Ag/AgCl are also consistent with pure material, free of Co(II)-impurities.[5] Again, the redox potential of **Co_4-TPP** was higher than that of **Co_4-TPB** due to TPP being more electron-withdrawing than TPB (Table 1). Increasing the pH to 11 and 12 led to an electrocatalytic OER current originating from the Co(III)/Co(IV) redox couple. The potential of this electrocatalytic wave is comparable to that of molecular cubane, **1**.[17] The onset overpotential is clearly lower for **Co_4-TPB** than for **Co_4-TPP**, reflecting the intrinsic electronic differences of these materials, and their ability to be precisely tuned *via* the choice of ancillary ligands.

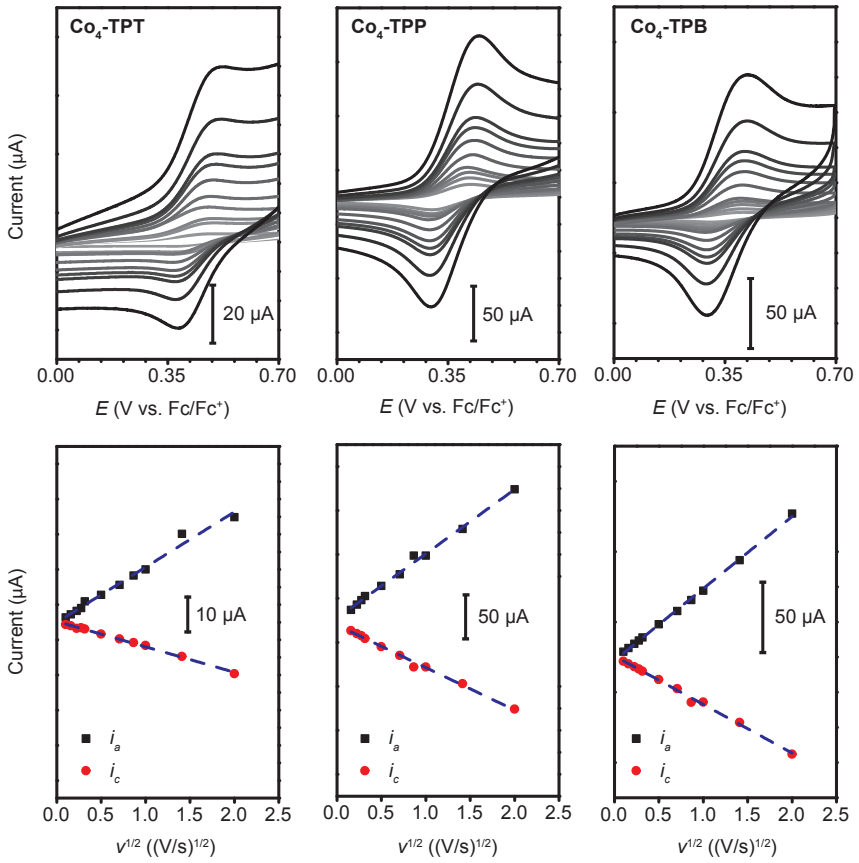

Figure 9. (Top panels) Cyclic voltammograms in acetonitrile with 0.1 M [*n*Bu$_4$N]PF$_6$ at varying scan rates. (Bottom panels) Plots of peak current versus the square root of scan rate showing linear correlations consistent with diffusion-controlled electron-transfer.

Table 1. Cyclic voltammetry data for **Co$_4$-TPT**, **Co$_4$-TPP**, and **Co$_4$-TPB**.

Compound	$E^{1/2}$ in MeCN (V vs. Fc/Fc$^+$)	$E^{1/2}$ in H$_2$O (V vs. Ag/AgCl)
1	0.280	1.008
Co$_4$-TPT	0.438	—
Co$_4$-TPP	0.351	1.052
Co$_4$-TPB	0.346	1.036

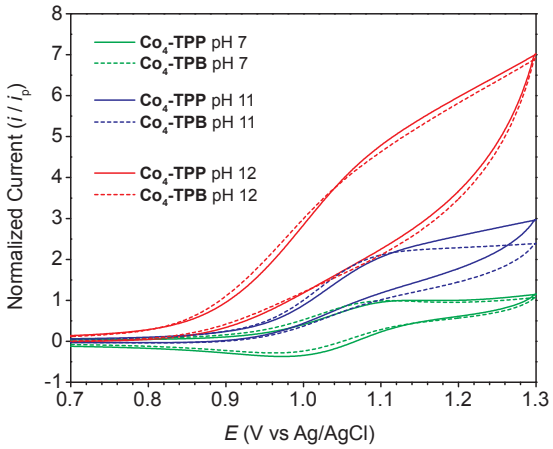

Figure 10. Cyclic voltammogram in 0.1 M KP_i (aq.) at pH = 7, 11, 12 and 100 mV/s scan rate.

4.3 **Conclusions**

A porous, solid-state material derived from a Co_4O_4 cubane, one of the most intriguing molecular structures capable of water oxidation, has been prepared. A suite of techniques, including UV-visible absorption, EPR, and X-ray absorption spectroscopies confirmed the preservation of Co_4O_4 units in the resulting coordination polymers. Nitrogen adsorption and PDF analysis provided experimental confirmation of the porous DFT-refined structural models for all materials, even though long-range crystallographic order was not observed. Favorable properties attained by the coordination polymers include high porosity, good thermal stability, and resistance to water oxidizing conditions that exceeds that of the parent cubane complex **1**. Most significantly, these new materials can be synthesized by a general, one-step method, and they retain a molecular level of electronic tunability. The simplicity of the synthesis should allow rapid development and screening of new derivatives. Stoichiometric oxidation with Ce(IV) provided evidence that the polymers operate *via* a well defined OER mechanism analogous to that by **1**,[17] and electrocatalysis experiments revealed activity trends among the polymer materials while demonstrating their suitability for practical heterogeneous catalysis. However, these materials are nonconductive and only small fractions of the materials are electrochemically active. Thus, new catalyst designs should incorporate features, such as redox-active linker ligands, that promote charge transport. The results presented in this work provide the basic design and synthesis of new metal-organic polymers for OER catalysis and underscore the potential of applying molecular design principles to heterogeneous catalysis.

4.4 Acknowledgements

I am grateful to Andy Nguyen, my lead collaborator in this project, for his enthusiasm and creativity in pursuing novel cubane chemistry. This material is based upon work performed by the Joint Center for Artificial Photosynthesis, a DOE Energy Innovation Hub, supported through the Office of Science of the U.S. Department of Energy under Award Number DE-SC0004993. The Advanced Light Source is supported by the Director, Office of Science, Office of Basic Energy Sciences, of the U.S. Department of Energy under Contract No. DE-AC02-05CH11231. Use of the Stanford Synchrotron Radiation Lightsource, SLAC National Accelerator Laboratory, is supported by the U.S. Department of Energy, Office of Science, Office of Basic Energy Sciences under Contract No. DE-AC02-76SF00515. DFT optimizations were performed using the resources of the National Energy Research Scientific Computing Center, a DOE Office of Science User Facility supported by the Office of Science of the U.S. Department of Energy under Contract No. DE-AC02-05CH11231.

4.5 Author Contributions[1]

Synthetic work in this chapter was a collaborative effort involving Andy I. Nguyen (for pyridyl-linked materials) and Kurt M. Van Allsburg (for carboxylate-linked materials). Both of these authors (A.I.N. and K.M.V.) also conducted spectroscopic and physical characterizations of the new materials. The structural models were constructed by K.M.V. and optimized by Michal Bajdich (Stanford University) using DFT. The X-ray scattering experiments and PDF analyses were performed by Maxwell W. Terban and Simon J. L. Billinge (Columbia University and Brookhaven National Lab). Porosimetry experiments were conducted by A.I.N., Julia Oktawiec and James P. Dombrowski (Berkeley). The stoichiometric and electrocatalytic OER experiments were contributed by A.I.N. and Micah S. Ziegler (Berkeley), and the EPR experiments were performed by K. V. Lakshmi (Rensselaer Polytechnic Institute). The XAS experiments were performed by K.M.V., A.I.N., and Walter S. Drisdell (Lawrence Berkeley National Lab), and the data analyzed by K.M.V., A.I.N., W.S.D., and Junko Yano (Lawrence Berkeley National Lab).

4.6 Experimental Details and Supplementary Information

4.6.1 General considerations

Materials. Cobalt(II) nitrate hexahydrate, pyridine, hydrogen peroxide (34-37% in water), ceric ammonium nitrate, benzene-1,3,5-tricarboxylic acid, and 1,3,5-tris(4-carboxyphenyl)benzene were purchased from Sigma-Aldrich and used without further purification. Sodium acetate trihydrate was purchased from EMD. Solvents were purchased from Fisher-Scientific and used without any further purification. Cubane **1**,[17,19] 1,3,5-tris(4-pyridyl)triazine,[51] 2,4,6-tris(4-pyridyl)pyridine,[52] 1,3,5-tris(4-pyridyl)benzene,[53] were

synthesized according to published procedures. MilliQ water was used in all experiments involving water.

Physical methods. Routine NMR spectra were recorded on Bruker AVB-400, AVQ-400 and AV-300 spectrometers at room temperature. DMSO-d_6 and 37% DCl in D_2O were purchased from Cambridge Isotopes. ^{1}H NMR spectra were referenced to residual protio-solvent peaks (δ 2.50 for DMSO-d_6, δ 4.79 for D_2O). Elemental analyses were carried out by the College of Chemistry Microanalytical Laboratory at the University of California, Berkeley. Inductively-coupled plasma (ICP) analysis were performed by Galbraith Laboratories. Electrochemical measurements were collected with three-electrode setup on a BASi Epsilon potentiostat. Thermogravimetric analysis were measured on a Seiko Instruments EXSTAR 6000. Scanning electron microscopy (SEM) images were collected using an FEI Quanta FEG 250 microscope at a working distance of 10 mm. A voltage of 1-5 kV was used to minimize sample annealing. The pH was measured with a Thermo Orion 2 Star bench top meter.

Raman spectroscopy. Raman spectra were collected using a confocal Raman microscope spectrometer (LabRAM HR, Horiba Yvon Jobin) at 633 nm and laser power 0.19–3.70 mW at the objective. The spot size of the laser beam is approximately 1–2 μm. Total acquisition time per spectrum was 180 s. Using a 600 g/mm grating, the spectral resolution is ~ 1 cm^{-1}. Spectral positions were calibrated using the 520.7 cm^{-1} band of a silicon wafer.

X-ray photoelectron spectroscopy. X-ray photoelectron spectra were collected using a Kratos Axis Ultra DLD system with a monochromatized Al Kα source (hν = 1486.6 eV), at power = 225 W. A pass energy for survey spectra of 160 eV and for elemental spectra of 20 eV was used. Spectra were fit using CasaXPS. Energy positions were corrected by shifting the C 1s core level position to 284.8 eV.

4.6.2 Synthetic procedures

$Co_4O_4(BTC)_{1.5}py_4$•4MeOH (Co_4-BTC). Cubane **1** (0.200 g, 0.234 mmol) and benzene-1,3,5-tricarboxylic acid (0.066 g, 0.312 mmol) were suspended in 10 mL of methanol in a scintillation vial. The capped vessel was heated to 60˚C for 2 h. The dark green solid was collected by filtration and washed 3 x 10 mL of methanol to yield 0.186 g (75%). Samples for elemental analysis were dried under vacuum at 70˚C for 12 h. Amount of methanol was determined by TGA mass loss (12%) at the first plateau region (160˚C). The solid was dissolved in a mixture of 37% DCl in D_2O and DMSO (1:1) to give a cyan solution. The solution was analyzed by ^{1}H NMR spectroscopy (Figure S1). The Raman spectrum (633 nm excitation) is shown in Figure S2. Anal calc'd for $(C_{20}H_{20}Co_4N_4O_4)(C_9H_3O_6)_{1.7}(H_2O)_9$: C, 41.47; H, 3.07; N, 5.48. Found: C, 41.08; H, 3.07; N, 5.08.

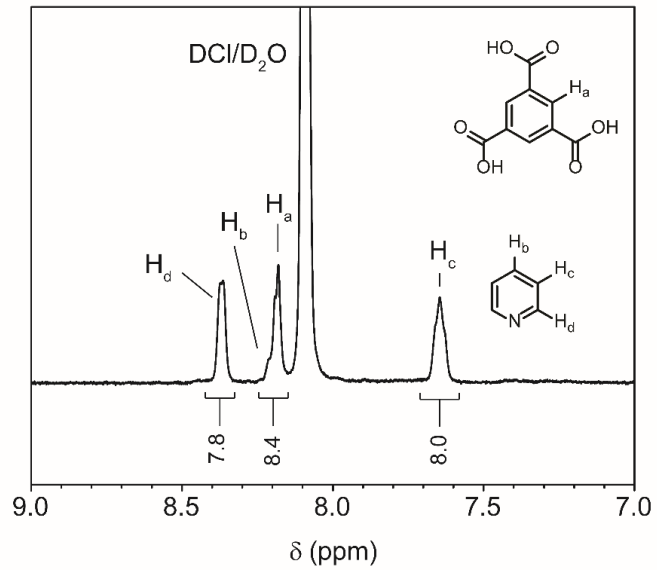

Figure S1. ^{1}H NMR (DMSO-d_6/D_2O) spectrum for **Co_4-BTC** after digestion in DCl/D_2O.

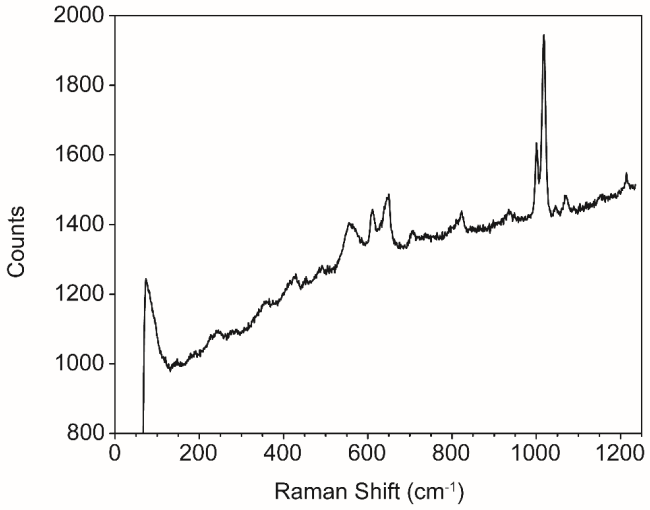

Figure S2. Raman spectrum for **Co_4-BTC**.

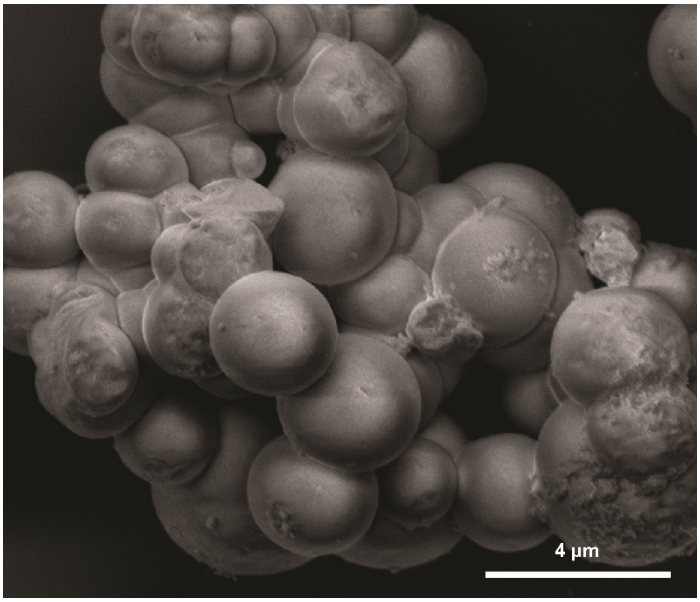

Figure S3. A higher magnification SEM image of as-synthesized **Co_4-BTC**.

$Co_4O_4(BTB)_{1.5}py_4$•5MeOH (Co_4-BTB). Cubane **1** (0.200 g, 0.234 mmol) and 1,3,5-tris(4-carboxyphenyl)benzene (0.137 g, 0.312 mmol) were suspended in 10 mL of methanol in a scintillation vial. The capped vessel was heated to 70˚C for 2 h. The dark green solid was collected by filtration and washed 3 x 10 mL of methanol to yield 0.247 g (72 %). Samples for elemental analysis were dried under vacuum at 70˚C for 12 h. Amount of methanol was determined by TGA mass loss (13%) at the first plateau region (160˚C). The solid was dissolved in a mixture of 37% DCl in D_2O and DMSO (1:1) to give a cyan solution. The solution was analyzed by ^1H NMR spectroscopy (Figure S4). The Raman spectrum (633 nm excitation) is shown in Figure S5.

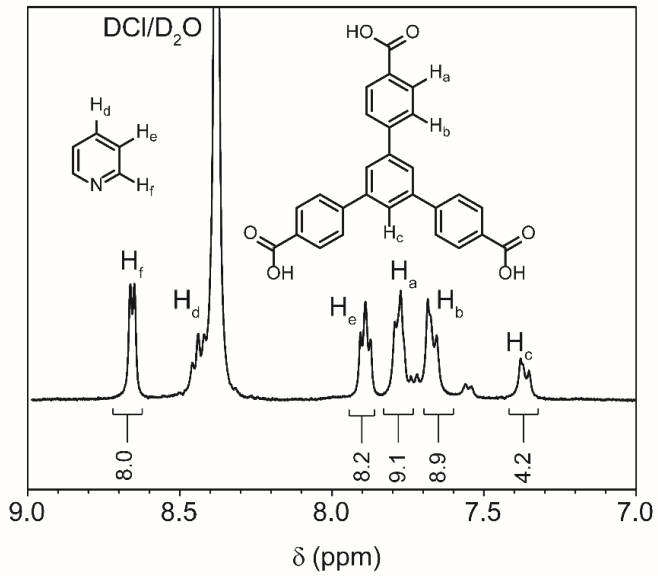

Figure S4. ^{1}H NMR (DMSO-d_6/D_2O) spectrum for **Co_4-BTB** after digestion in DCl/D_2O.

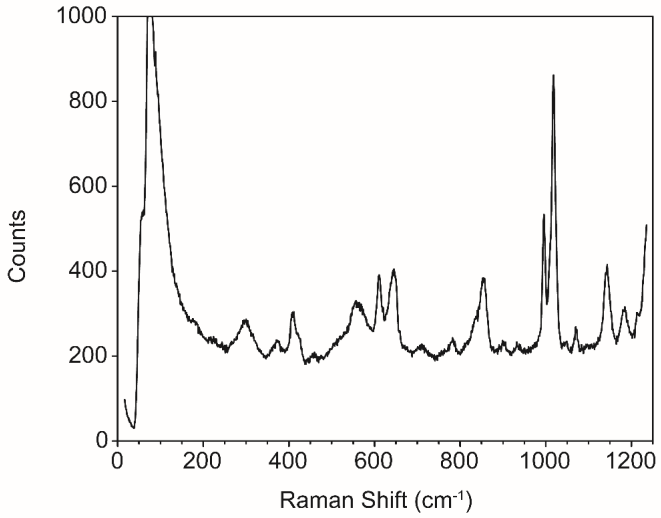

Figure S5. Raman spectrum for **Co_4-BTB**.

$Co_4O_4(OAc)_4(TPT)_{1.9}$•8MeOH ($Co_4$-TPT). Cubane **1** (0.050 g, 0.059 mmol) and 1,3,5-tris(4-pyridyl)triazine (0.025 g, 0.080 mmol) were suspended in 10 mL of benzonitrile in a Schlenk tube. An active vacuum was applied and the vessel was heated to 100˚C for 2 days. The dark red solid was collected by filtration and washed 3 x 20 mL of methanol. The solid was transferred to a Soxhlet apparatus, and extracted with methanol for 24 h to yield 0.047 g (58 %). Samples for elemental analysis were dried under vacuum at 70˚C for 12 h. Amount of methanol was determined by TGA mass loss (18%) at the first plateau region (160˚C). The solid was dissolved in a mixture of 37% DCl in D_2O to give a cyan solution. The solution was analyzed by ^{1}H NMR spectroscopy (Figure S6). The Raman spectrum (633

nm excitation) is shown in Figure S7. Anal calc'd for $(C_8H_{12}Co_4O_{12})(C_{18}N_{12}N_6)_{1.57}$: C, 42.41; H, 3.03; N, 12.87. Found: C, 42.63; H, 3.23; N, 12.67.

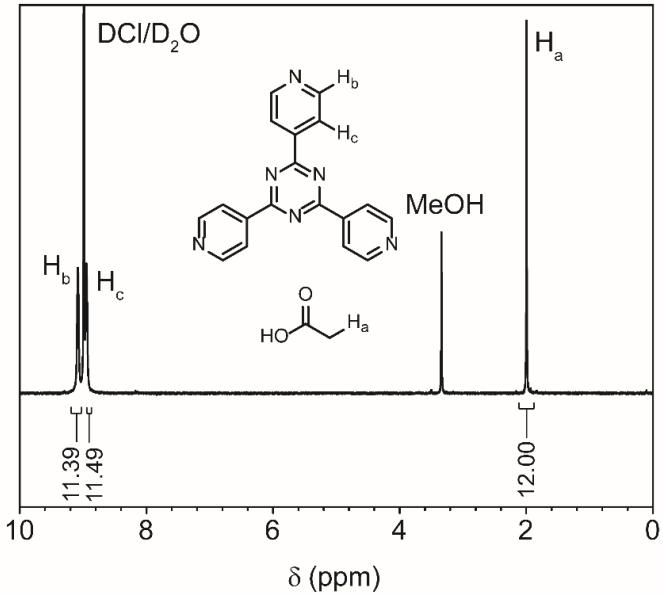

Figure S6. ^{1}H NMR (D_2O) spectrum for **Co_4-TPT** after digestion in DCl/D_2O.

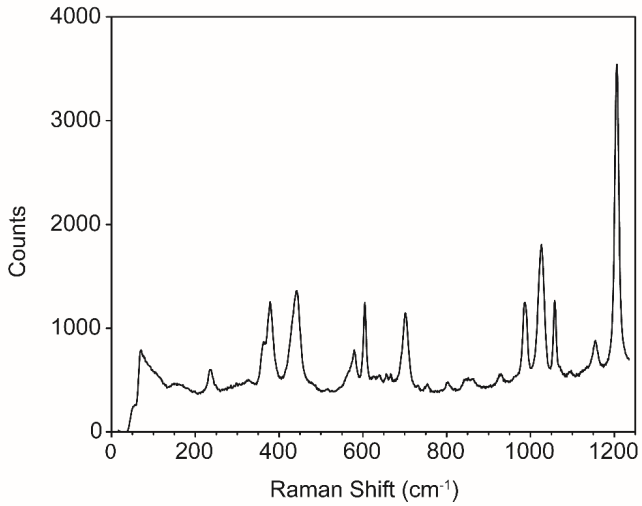

Figure S7. Raman spectrum for **Co_4-TPT**.

$Co_4O_4(OAc)_4(TPP)_{2.3}$•9MeOH ($Co_4$-TPP). Cubane **1** (0.500 g, 0.587 mmol) and 2,4,6-tris(4-pyridyl)pyridine (0.243 g, 0.782 mmol) were suspended in 30 mL of benzonitrile in a Schlenk tube. An active vacuum was applied and the vessel was heated to 90°C for 2 days. The dark solid was collected by filtration and washed 50 mL of methanol. The solid was transferred to a Soxhlet apparatus, and extracted with methanol for 24 h to yield 0.614 g (68 %). Samples for elemental analysis were dried under vacuum at 70°C for 12 h. Amount of

methanol was determined by TGA mass loss (20 %) at the first plateau region (160°C). The solid was dissolved in a mixture of 37% DCl in D_2O to give a cyan solution. The solution was analyzed by ^1H NMR spectroscopy (Figure S8). The Raman spectrum (633 nm excitation) is shown in Figure S9. Anal calc'd for $(C_8H_{12}Co_4O_{12})(C_{18}N_{12}N_6)_{1.48}$: C, 45.41; H, 3.32; N, 8.34. Found: C, 45.23; H, 3.17; N, 8.58.

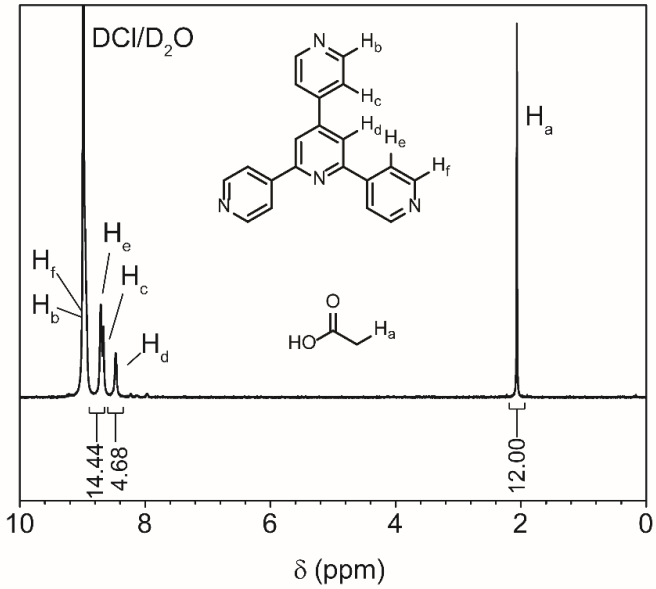

Figure S8. ^1H NMR (D_2O) spectrum for **Co_4-TPP** after digestion in DCl/D_2O.

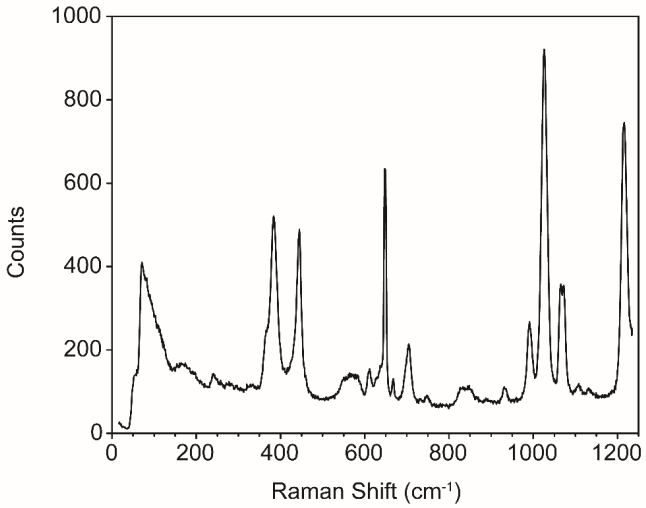

Figure S9. Raman spectrum for **Co_4-TPP**.

$Co_4O_4(OAc)_4(TPB)_{1.33}$•8MeOH ($Co_4$-TPB). Cubane **1** (0.500 g, 0.587 mmol) and 1,3,5-tris(4-pyridyl)benzene (0.242 g, 0.782 mmol) were suspended in 30 mL of benzonitrile in a Schlenk tube. An active vacuum was applied and the vessel was heated to 90°C for 2

days. The dark solid was collected by filtration and washed 50 mL of methanol. The solid was transferred to a Soxhlet apparatus, and extracted with methanol for 24 h to yield 0.578 g (82 %). Samples for elemental analysis were dried under vacuum at 70˚C for 12 h. Amount of methanol was determined by TGA mass loss (22 %) at the first plateau region (160˚C). The solid was dissolved in a mixture of 37% DCl in D_2O to give a cyan solution. The solution was analyzed by ^1H NMR spectroscopy (Figure S10). The Raman spectrum (633 nm excitation) is shown in Figure S11. Anal calc'd for $(C_8H_{12}Co_4O_{12})(C_{18}N_{12}N_6)_{1.33}(H_2O)_4$: C, 44.47; H, 3.59; N, 5.76. Found: C, 44.23; H, 3.43; N, 6.01.

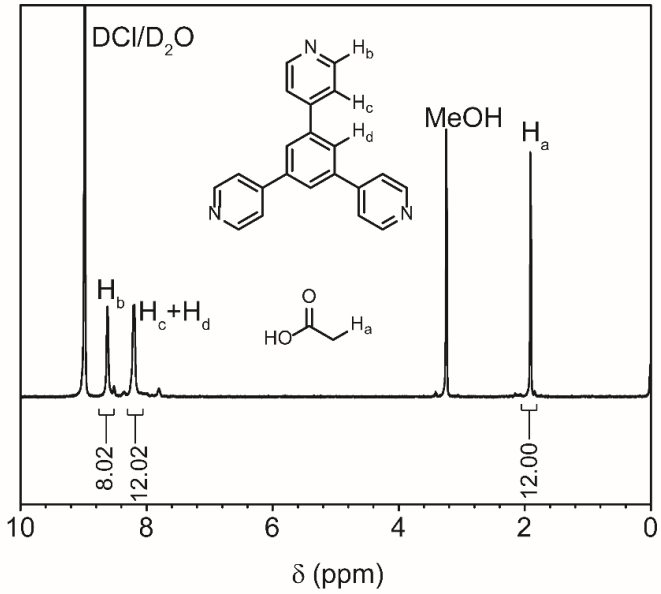

Figure S10. ^1H NMR (D_2O) spectrum for **Co_4-TPT** after digestion in DCl/D_2O.

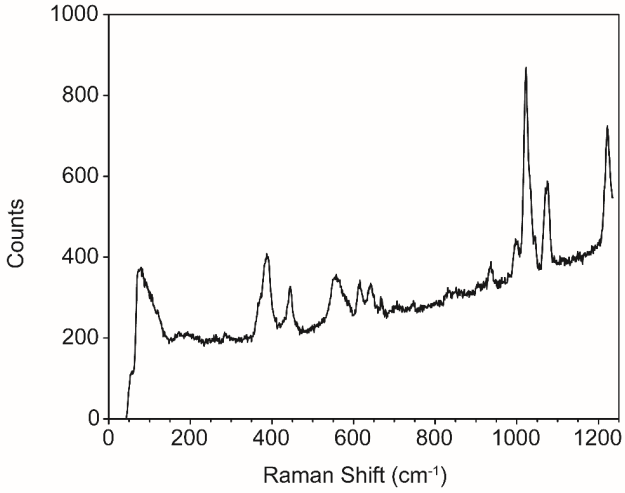

Figure S11. Raman spectrum for **Co_4-TPB**.

Removal of trace Co(II) impurities by chelation. The following procedure was used to allow stirring of polymer materials during chelation while ensuring that the chelating membrane was not mechanically degraded and could be separated from the polymer after chelation (Figure S12). Polymer samples were placed in a small (e.g. 100 mL) beaker equipped with a stir bar. A filter paper basket was folded over the edge of the beaker so that it hung down ~ 1 cm into the beaker. A section of Empore SPE chelating membrane was placed into the basket and the basket was filled partially with water. Then, water was carefully added to the lower compartment (below the filter paper basket, containing the polymer), until no air remained below the filter paper. The filter paper was then sealed to the outside of the beaker by wrapping with Teflon tape. The upper compartment was then filled with water and the entire assembly sealed carefully with Parafilm. The chelation experiments were stirred for 5 days at a time, after which the chelating membrane was checked for pink color. If color was observed, the procedure was repeated until no more color, indicative of the presence of Co(II), was observed. Samples required 1-5 treatments to reach this point.

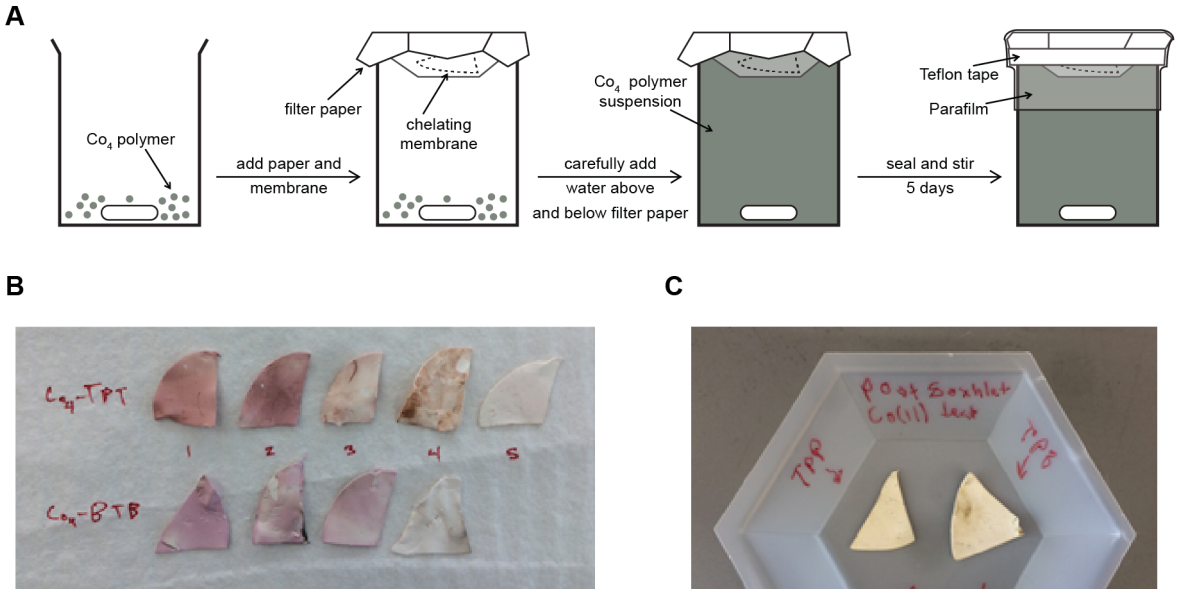

Figure S12. (A) Chelation procedure used to remove Co(II) impurities from polymer materials. (B) Empore SPE chelating membranes after successive chelation experiments with selected polymer samples, showing the decrease in pink color with successive treatments.

Replacement of carboxylate ligands in polymers by NaOH exchange. Each sample (0.1 g) was suspended in 1 M NaOH solution (10 mL) and stirred gently for 5 h. The solids were collected by filtration and washed with water (3 x 10 mL), then soaked in water (5 mL) for 12 h with stirring. The pH of the aqueous solution after soaking was observed to be near neutral (7–8). The solids were then filtered and washed with water (3 x 10 mL). The Raman spectra for the products from the reaction of NaOH with the polymers are shown in Figure S13.

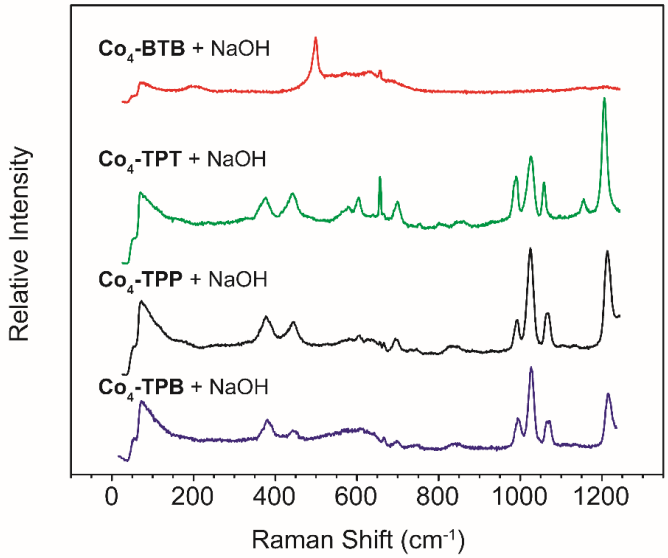

Figure S13. Raman spectra for the products from the reaction of NaOH with the polymers.

4.6.3 Physical and chemical characterization of polymer materials

Thermogravimetric analysis. Samples (3-5 mg) were analyzed under N_2 flow, at a ramp rate of 10˚C/min, from room temperature to 500˚C.

Gas sorption measurements. Nitrogen adsorption isotherms for pressures in the range 0–1.2 bar were measured using a volumetric method using either a Micromeritics ASAP2020 or ASAP2420 instrument. Samples were transferred into preweighed analysis tubes, then capped with a Transeal. Samples were first activated under vacuum with applied heat in a gas sorption tube (70˚C for **Co₄-BTC** and **Co₄-BTB**, 100˚C for **Co₄-TPT**, **Co₄-TPP**, and **Co₄-TPB**) for 12 h to remove solvent (until the outgas rate was <1 μbar/min), at which point the tube was weighed to determine the mass of the activated sample. The tube was transferred to the analysis port of the instrument and the outgas rate was again checked to ensure that it was <1 μbar/min. UHP-grade (99.999% purity) N_2 and He were used for all adsorption measurements. For all isotherms, warm and cold free spaces were measured using He; N_2 at 77 were measured in liquid nitrogen. BET surface areas were calculated from the linear region of the N_2 isotherms at 77 K were determined using Micromeritics software.

Oxidation of polymers. The samples (0.075 g) were stirred gently in 5 mL of 0.2 M $Ce(NO_3)_6(NH_4)_2$ for 1 h. The solids were collected by filtration and washed with water (3 x 5 mL), then soaked in water (5 mL) for 15 min with stirring. The washed solids were collected by filtration, washed with water (3 x 5 mL), and used immediately for EPR measurements or stoichiometric water oxidation. Note that the oxidized samples decomposed over the course of hours at room temperature, as observed by changes in their EPR spectra.

EPR Spectroscopy. X-band EPR spectroscopy was carried out using a Bruker Instruments (Billerica, MA) Elexsys EPR spectrometer equipped with a dual mode cavity.

Temperature was controlled with an Oxford Instruments liquid helium cryostat. Samples were finely ground and placed into 4 mm quartz tubes for measurement.

4.6.4 Structural characterization of polymer materials

X-ray absorption spectroscopy. X-ray absorption spectra were taken at the Advanced Light Source (ALS) on Beamline 10.3.2. The radiation was monochromatized by a Si (111) double-crystal monochromator. The intensity of the incident X-ray (I_0) was monitored by an N_2-filled ionization chamber in front of the sample. The energy was calibrated using a glitch in I_0 relative to the absorption edge of a Co foil. Samples were cooled to –20 ˚C using a Peltier cooling stage. All data were collected using a quick XAS scan mode, and the data collection was carried out under the threshold of X-ray radiation damage, by monitoring with the XANES edge shift. Data reduction was performed using custom software (Matthew Markus, BL 10.3.2, ALS). Pre-edge and post-edge contributions were subtracted from the XAS spectra, and the result was normalized with respect to the edge jump.

Construction of structural models. Complex **1** has idealized D_{2d} site symmetry (neglecting acetate methyl groups), where κ^2-carboxylates cap four equatorial faces (~90˚ apart) and pyridine ligands cap the two remaining, opposite faces (180˚ apart) of the cubane. The BTC and BTB linkers have idealized D_{3h} symmetry, which is expected to reduce to D_3 in the **Co$_4$-BTC** and **Co$_4$-BTB** polymers because the cubane units cannot be arranged to maintain the mirror planes in D_{3h}. Searching the RCSR for known framework structures with one four-coordinate vertex, one three-coordinate vertex, and one edge type yields eight candidates – **bor**, **bor-c**, **bor-c***, **ctn**, b, **mhq-z**, **pto**, and **tbo** – of which **bor**, **ctn**, **mhq-z**, **pto**, and **tbo** are unique. The remaining three are interpenetrated versions of these structures. Two of the five candidates – **bor** and **ctn** – were discarded because their four-coordinate vertices, while having D_{2d} site symmetry or a subset thereof, are tetrahedrally coordinated and therefore incompatible with the tetragonal arrangement of carboxylate edge sites around the cube. A third, **mhq-z**, was eliminated because its topological density appears too high for the axial pyridine ligands to fit in the structure. The remaining structures – **pto** and **tbo** – differ in the dihedral angle between the threefold axis and the rotation axis of the S_4 operation. In **tbo** it is 90˚, while in **pto** it is smaller (e.g. 55˚ for MOF-143). Both structures were used to construct models. In the case of **pto** (*Pm*-3*m*), the symmetry of the four-coordinate vertices, -42*m* (D_{2d}), matches the cubane and that of the three-coordinate vertices, 32 (D_3), matches BTC/BTB. In the case of **tbo** (*Fm*-3*m*), the formal crystallographic symmetry of the net – *mmm* (D_{2h}) for four-coordinate sites and 3*m* (C_{3v}) for three-coordinate sites – is different from that expected for **Co$_4$-BTC** and **Co$_4$-BTB** and thus a "pseudo-**tbo**" structure that lacks some of the symmetry operations of *Fm*-3*m* was constructed.

For **Co$_4$-TPT**, **Co$_4$-TPP**, and **Co$_4$-TPB**, the only vertex is the pyridyl linker, with idealized D_{3h} symmetry, and the edges with Co_4 cubanes have idealized D_{2d} symmetry. Searching the RCSR for structures with one three-coordinate vertex and one edge produces only the **srs** net (and its interpenetrated analogues **srs-c**, **srs-c4**, and **srs-c8**). Site symmetry in

srs (*I*4(1)32) – 32 (D_3) for vertices and 222 (D_2) for edges – is a subset of the idealized symmetry above and thus compatible.

For each of the candidate structures, the unit cell was sized by applying an estimate of the edge length, from atomic coordinates in **1** and linker molecules, to the fractional edge length defined by the space group. Atomic coordinates from the molecular complex **1** were then transformed to be correctly sized, oriented, and positioned on the appropriate Wyckoff positions. Finally, linker molecules were constructed along edge sites, using previously published structural parameters (e.g. from HKUST-1[54] and MOF-143[55]) where needed.

DFT optimization of structural models. The structural models were relaxed by density functional theory (DFT+U) calculations within the Vienna *Ab-initio* Simulation Package (VASP).[42-44] Structures with centered unit cells (**tbo** and **srs**) were reduced to primitive cells to minimize computational burden. To meet the requirements of VASP, all crystallographically related atoms were treated independently (*i.e.* all structures were converted to *P*1). As with other studies of Co^{III}-oxides,[56-58] the Perdew-Burke-Ernzerhof (PBE)[59] exchange-correlation functional was employed with the Hubbard-U correction[60] and a value of U = 3.32 eV[61,62] for Co atoms. Next, all the atomic positions, cell shape and volume of all the systems were optimized using high energy cutoff of 600 eV to reach a maximum force threshold of 0.05 eV/Å and stress below 0.01 kBar.

X-ray total scattering and pair distribution function. The experiments were carried out at Beamline 28-ID-1 at NSLS-II at Brookhaven National Laboratory using the rapid acquisition PDF method (RAPDF).[63] A 2D Perkin Elmer detector was placed 218.7025 mm behind the samples which were loaded in 1 mm ID Kapton capillaries. The incident wavelength of the X-rays was λ = 0.1827 Å. Calibration of the experimental setup was done using a Ni standard as a calibrant.

Datasets were collected at 100 K using a flowing nitrogen cryostream cooler. The detector exposure time was adjusted for each sample to avoid detector saturation, and the number of frames taken for each sample was adjusted to obtain sufficient counting statistics on the data.

Raw data were summed and corrected for polarization effects before being integrated along arcs of constant angle to produce 1D powder diffraction patterns using the program fit2D.[64] Corrections were then made to the data and normalizations carried out to obtain the total scattering structure function, $F(Q)$, which was Fourier transformed to obtain the PDF using PDFgetX3[65] within xPDFsuite.[66] The maximum range of data used in the Fourier transform (Q_{max}, where $Q = (4\pi \sin\theta)/\lambda$ is the magnitude of the momentum transfer on scattering) was varied depending on the quality of the data. Figure S14 shows the data in various stages of the analysis, from raw intensity at the top, through $F(Q)$ in the middle, to $G(r)$ at the bottom.

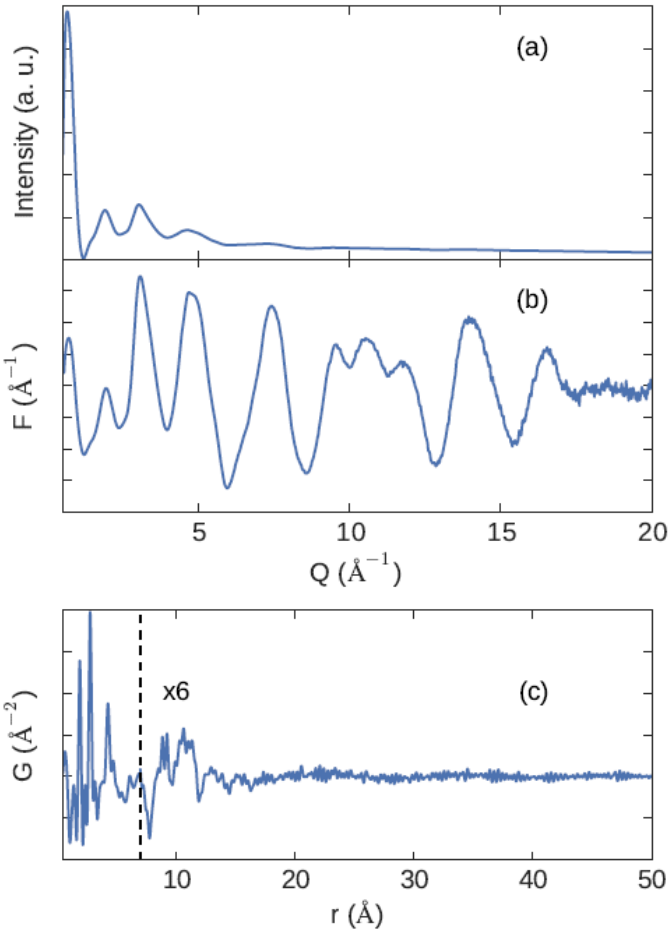

Figure S14. Representative raw intensities (background subtracted) (a), *F*(*Q*) (b) and *G*(*r*) (c) curves from **Co_4-TPT** sample. Note that after processing a clear signal at high-Q is evident in *F*(*Q*) that is not so clear in the raw data.

4.6.5 OER experiments

General procedure for stoichiometric OER. Oxygen was detected using an Ocean Optics Multi-Frequency Phase Fluorimeter (MFPF-100) with a FOSPOR-R probe inserted in the headspace of a sealed flask. The probe was calibrated at a single temperature by fitting a second order polynomial to eight O_2 concentrations between 0.0 and 10.6%, which were produced using pair of mass-flow controllers. Henry's Law was used to account for oxygen that remained dissolved in solution.

Baseline O_2: A 10 mL round bottom flask was equipped with a stir bar. The flask was stoppered with a rubber septum holding the Ocean Optics O_2 sensor probe. Silicone grease was used to seal around the probe. The flask was then purged with N_2 (*via* an inlet needle and an exit needle) for 10 minutes. The purging needle was removed and the O_2 was measured for ~10 minutes, at which point, a 1.0 mL solution of 1 M NaOH was added. The O_2 measurement was continued for 25 min.

With [Co_4-TPT]$^+$: A 10 mL round bottom flask was filled with solid **[Co_4-TPT]$^+$** (*vide supra*, 0.058 g). The flask was stoppered with a rubber septum holding the Ocean Optics O_2 sensor probe. Silicone grease was used to seal around the probe. The flask was then purged with N_2 (*via* an inlet needle and an exit needle) for 10 minutes. The purging needle was removed and the O_2 was measured for ~5 minutes, at which point, a 1.0 mL solution of 1 M NaOH was added. The O_2 measurement was continued for ~25 min.

With [Co_4-TPP]$^+$: A 10 mL round bottom flask was filled with solid **[Co_4-TPP]$^+$** (*vide supra*, 0.100 g). The flask was stoppered with a rubber septum holding the Ocean Optics O_2 sensor probe. Silicone grease was used to seal around the probe. The flask was then purged with N_2 (*via* an inlet needle and an exit needle) for 10 minutes. The purging needle was removed and the O_2 was measured for ~5 minutes, at which point, a 1.0 mL solution of 1 M NaOH was added. The O_2 measurement was continued for ~25 min.

With [Co_4-TPB]$^+$: A 10 mL round bottom flask was filled with solid **[Co_4-TPB]$^+$** (*vide supra*, 0.100 g). The flask was stoppered with a rubber septum holding the Ocean Optics O_2 sensor probe. Silicone grease was used to seal around the probe. The flask was then purged with N_2 (*via* an inlet needle and an exit needle) for 10 minutes. The purging needle was removed and the O_2 was measured for ~5 minutes, at which point, a 1.0 mL solution of 1 M NaOH was added. The O_2 measurement was continued for ~25 min.

Recycling experiment. After the stoichiometric OER experiment ended, **Co_4-TPT** was collected by filtration and washed with water (~50 mL). The solid was collected and oxidized again by the procedure described above, and the stoichiometric OER reaction was repeated.

Electrochemistry. Samples analyzed by electrochemistry were first suspended in solution by the following procedure. A small amount of solid (~1-2 mg) is ground by mortar and pestle in 0.5 mL ethanol (for **Co_4-BTC**, **Co_4-BTB**, **Co_4-TPP**, and **Co_4-TPB**) or isopropanol (**Co_4-TPT**). These solvent choices gave the best suspension in our hands. The slurry is transferred to a polypropylene tube, diluted to 2 mL with the same solvent, and then sonicated for 1 h. The suspension was allowed to settle for 24 h, and the colored colloidal solution was decanted for use. Only **Co_4-TPP**, **Co_4-TPB**, and **Co_4-TPT** had colored solutions indicative of colloids. The cobalt concentrations were determined by ICP analysis, and the results are listed in Table S1.

Table S1. Concentration of polymer in suspended solutions by ICP analysis.

Polymer	Solvent	[Co] (mM)	[Co_4O_4] (mM)
Co_4-TPT	*i*PrOH	0.271	0.0678
Co_4-TPP	EtOH	0.680	0.170
Co_4-TPB	EtOH	0.477	0.119

To prepare the electrodes, two drops (22.8 ± 0.28 μL for EtOH, 20.2 ± 0.66 μL for *i*PrOH) of the solution were drop-cast onto a glassy carbon disk electrode ($A_{electrode}$ = 0.0707 cm^2) surrounded by a Teflon casing (A_{total} = 0.322 cm^2). The solution was evaporated at room temperature to give a film. The loading of Co_4O_4 on the glassy carbon disk was calculated by

the method below and listed in Table S2. SEM images of the drop-cast films are shown in Figure S15, demonstrating particle sizes on the order of a micron.

Calculation of electrode loading:
Loading = *volume suspension* (L) x [Co_4O_4] (mol/L) x $A_{electrode}/A_{total}$

Table S2. Calculated loadings of polymer on electrode

Polymer	Co_4O_4/Area (mol/cm^2)	Loading on electrode (mol)
Co_4-TPT	4.24 x 10^{-9}	2.99 x 10^{-10}
Co_4-TPP	1.20 x 10^{-8}	8.55 x 10^{-10}
Co_4-TPB	8.46 x 10^{-9}	5.98 x 10^{-10}

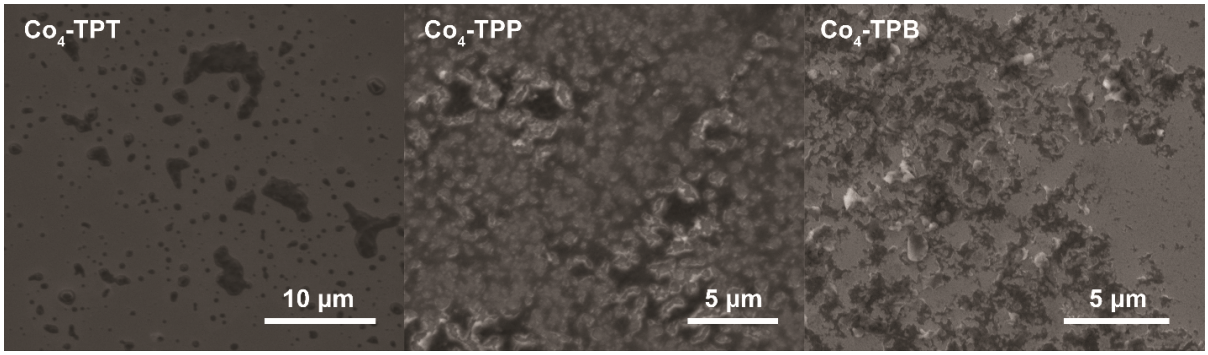

Figure S15. SEM images of drop-cast polymers on silicon wafer.

Nonaqueous CV. Cyclic voltammograms were collected in 0.1 M ^{n}Bu$_4$NPF$_6$ electrolyte in MeCN at room temperature with *iR* compensation. Ag wire was used as a floating reference, and Pt wire was used as the counter electrode. Ferrocene was added as an internal standard. The scan rate was varied from 10 mV/s to 4000 mV/s. The integrated peak areas are show in Figure S16 and listed in Table S3.

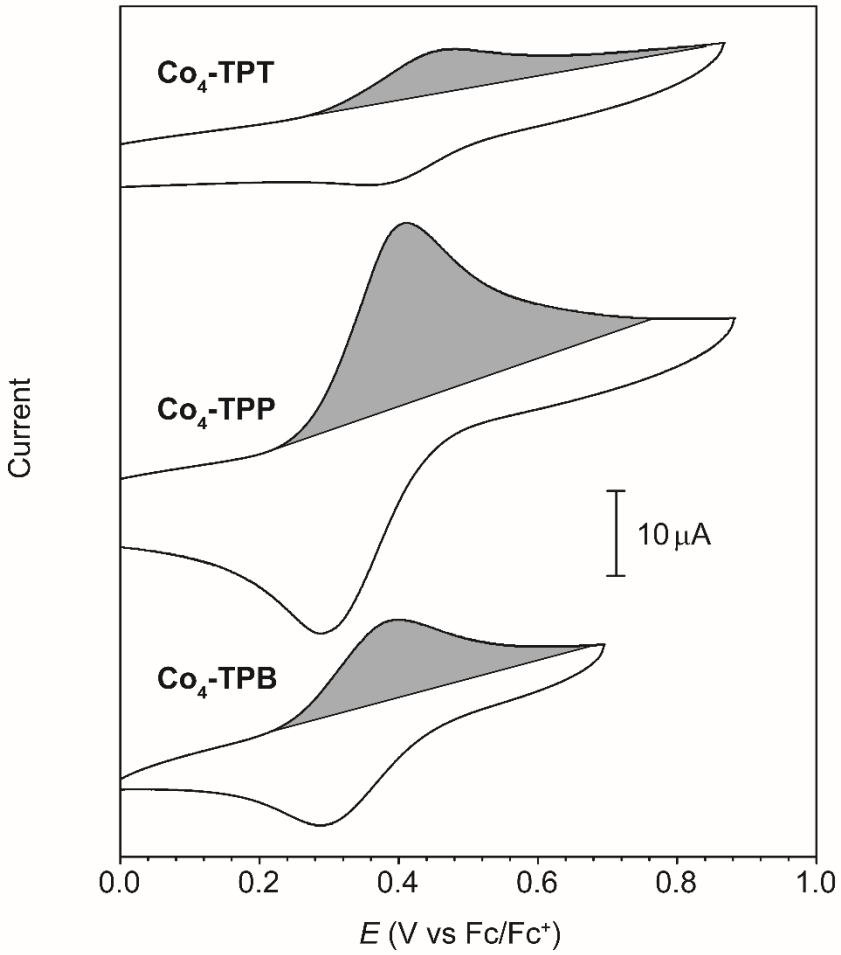

Figure S16. Integration of anodic peaks for CVs in MeCN at 100 mV/s.

Table S3. Integrated areas of anodic peaks.

Polymer	Anodic peak area (coulombs)	mol e^-/mol Co_4O_4 (%)
Co_4-TPT	1.15 x 10^{-6}	4.0%
Co_4-TPP	4.72 x 10^{-6}	5.7%
Co_4-TPB	1.82 x 10^{-6}	3.2%

Aqueous CV. Aqueous electrochemical data were collected in 0.1 M KPi buffer at pH 7, 11, and 12. The pH was adjusted by addition of 1.0 M NaOH and measured by a pH meter. No *iR* compensation was applied since solution resistance was assumed to be negligible. Note that the application of *iR* compensation occasionally lead to deleterious potentiostat oscillations and damaging of the electrode.

4.7 References

(1) This chapter is based upon a manuscript that is being prepared for future publication: Nguyen, A. I.;* Van Allsburg, K. M.*, Terban, M. W.; Bajdich, M.; Oktawiec, J.; Ziegler, M. S.; Dombrowski, J. P.; Lakshmi, K. V.; Drisdell, W. S.; Yano, J.; Billinge, S. J. L.; Tilley, T. D. *in preparation*. *Denotes equal contribution. It is included here with the permission of all authors.

(2) Crabtree, R. H. *Chem. Rev.* **2011**, *112*, 1536–1554.

(3) Crabtree, R. H. *Chem. Rev.* **2015**, *115*, 127–150.

(4) Wuttig, A.; Surendranath, Y. *ACS Catal.* **2015**, *5*, 4479–4484.

(5) Ullman, A. M.; Liu, Y.; Huynh, M.; Bediako, D. K.; Wang, H.; Anderson, B. L.; Powers, D. C.; Breen, J. J.; Abruña, H. D.; Nocera, D. G. *J. Am. Chem. Soc.* **2014**, *136*, 17681–17688.

(6) Trotochaud, L.; Young, S. L.; Ranney, J. K.; Boettcher, S. W. *J. Am. Chem. Soc.* **2014**, *136*, 6744–6753.

(7) Roger, I.; Symes, M. D. *J. Am. Chem. Soc.* **2015**, *137*, 13980–13988.

(8) Baricuatro, J. H.; Saadi, F. H.; Carim, A. I.; Velazquez, J. M.; Kim, Y.-G.; Soriaga, M. P. *J. Phys. Chem. C* **2015**, DOI: 10.1021/acs.jpcc.5b07028.

(9) Grotjahn, D. B.; Brown, D. B.; Martin, J. K.; Marelius, D. C.; Abadjian, M.-C.; Tran, H. N.; Kalyuzhny, G.; Vecchio, K. S.; Specht, Z. G.; Cortes-Llamas, S. A.; Miranda-Soto, V.; van Niekerk, C.; Moore, C. E.; Rheingold, A. L. *J. Am. Chem. Soc.* **2011**, *133*, 19024–19027.

(10) Hocking, R. K.; Brimblecombe, R.; Chang, L.-Y.; Singh, A.; Cheah, M. H.; Glover, C.; Casey, W. H.; Spiccia, L. *Nature Chem.* **2011**, *3*, 461–466.

(11) Stracke, J. J.; Finke, R. G. *J. Am. Chem. Soc.* **2011**, *133*, 14872–14875.

(12) Stracke, J. J.; Finke, R. G. *ACS Catal.* **2013**, *3*, 1209–1219.

(13) Stracke, J. J.; Finke, R. G. *ACS Catal.* **2014**, *4*, 909–933.

(14) Goberna Ferrón, S.; Soriano López, J.; Galán Mascarós, J. R.; Nyman, M. *Eur. J. Inorg. Chem.* **2015**, 2833–2840.

(15) Batten, S. R.; Champness, N. R.; Chen, X.-M.; Garcia-Martinez, J.; Kitagawa, S.; Öhrström, L.; O'Keeffe, M.; Suh, M. P.; Reedijk, J. *CrystEngComm* **2012**, *14*, 3001–3004.

(16) Zhou, H.-C.; Long, J. R.; Yaghi, O. M. *Chem. Rev.* **2012**, *112*, 673–674.

(17) Nguyen, A. I.; Ziegler, M. S.; Oña-Burgos, P.; Sturzbecher-Hohne, M.; Kim, W.; Bellone, D. E.; Tilley, T. D. *J. Am. Chem. Soc.* **2015**, *137*, 12865–12872.

(18) Wang, C.; Wang, J.-L.; Lin, W. *J. Am. Chem. Soc.* **2012**, *134*, 19895–19908.

(19) Chakrabarty, R.; Bora, S.; Das, B. K. *Inorg. Chem.* **2007**, *46*, 9450–9462.

(20) McAlpin, J. G.; Stich, T. A.; Ohlin, C. A.; Surendranath, Y.; Nocera, D. G.; Casey, W. H.; Britt, R. D. *J. Am. Chem. Soc.* **2011**, *133*, 15444–15452.

(21) Feldblyum, J. I.; Liu, M.; Gidley, D. W.; Matzger, A. J. *J. Am. Chem. Soc.* **2011**, *133*, 18257–18263.

(22) McDonald, T. M.; Bloch, E. D.; Long, J. R. *Chem. Commun.* **2015**, *51*, 4985–4988.

(23) Langford, C. H.; Gray, H. B. *Ligand Substitution Processes*; W. A. Benjamin, Inc.: New York, New York, 1966.
(24) Ono, T.-A.; Noguchi, T.; Inoue, Y.; Kusunoki, M.; Matsushita, T.; Oyanagi, H. *Science* **1992**, *258*, 1335–1337.
(25) Yachandra, V. K.; Sauer, K.; Klein, M. P. *Chem. Rev.* **1996**, *96*, 2927–2950.
(26) Iuzzolino, L.; Dittmer, J.; Dörner, W.; Meyer-Klaucke, W.; Dau, H. *Biochemistry* **1998**, *37*, 17112–17119.
(27) Messinger, J.; Robblee, J. H.; Bergmann, U. *J. Am. Chem. Soc.* **2001**, *123*, 7804–7820.
(28) Yano, J.; Yachandra, V. K. *Photosynth. Res.* **2007**, *92*, 289–303.
(29) Brena, B.; Siegbahn, P. E. M.; Ågren, H. *J. Am. Chem. Soc.* **2012**, *134*, 121003072852009.
(30) Risch, M.; Khare, V.; Zaharieva, I.; Gerencser, L.; Chernev, P.; Dau, H. *J. Am. Chem. Soc.* **2009**, *131*, 6936–6937.
(31) Kanan, M. W.; Yano, J.; Surendranath, Y.; Dincă, M.; Yachandra, V. K.; Nocera, D. G. *J. Am. Chem. Soc.* **2010**, *132*, 13692–13701.
(32) Kanady, J. S.; Tran, R.; Stull, J. A.; Lu, L.; Stich, T. A.; Day, M. W.; Yano, J.; Britt, R. D.; Agapie, T. *Chem. Sci.* **2013**, *4*, 3986–3996.
(33) Tsui, E. Y.; Tran, R.; Yano, J.; Agapie, T. *Nature Chem.* **2013**, *5*, 293–299.
(34) Suseno, S.; McCrory, C. C. L.; Tran, R.; Gul, S.; Yano, J.; Agapie, T. *Chem. Eur. J.* **2015**, *21*, 13420–13430.
(35) Van Allsburg, K. M.; Anzenberg, E.; Drisdell, W. S.; Yano, J.; Tilley, T. D. *Chem. Eur. J.* **2015**, *21*, 4646–4654.
(36) Egami, T.; Billinge, S. J. L. *Underneath the Bragg Peaks*, 2nd ed.; Elsevier: Amsterdam, 2012.
(37) Billinge, S. J. L.; Kanatzidis, M. G. *Chem. Commun.* **2004**, 749–760.
(38) Billinge, S. J. L. *J. Solid State Chem.* **2008**, *181*, 1695–1700.
(39) O'Keeffe, M.; Peskov, M. A.; Ramsden, S. J.; Yaghi, O. M. **2008**.
(40) Delgado-Friedrichs, O.; O'Keeffe, M.; Yaghi, O. M. *Acta Crystallogr., Sect. A: Found. Crystallogr.* **2006**, *62*, 350–355.
(41) Delgado-Friedrichs, O.; O'Keeffe, M.; Yaghi, O. M. *Acta Crystallogr., Sect. A: Found. Crystallogr.* **2003**, *59*, 22–27.
(42) Kresse, G.; Hafner, J. *Phys. Rev. B* **1993**, *47*, 558–561.
(43) Kresse, G.; Furthmüller, J. *Computational Materials Science* **1996**, *6*, 15–50.
(44) Kresse, G.; Joubert, D. *Phys. Rev. B* **1999**, *59*, 1758–1775.
(45) Ullman, A. M.; Brodsky, C. N.; Li, N.; Zheng, S.-L.; Nocera, D. G. *J. Am. Chem. Soc.* **2016**, *138*, 4229–4236.
(46) Hansen, R. E.; Das, S. *Energy Environ. Sci.* **2014**, *7*, 317–322.
(47) Meyer, K.; Ranocchiari, M.; van Bokhoven, J. A. *Energy Environ. Sci.* **2015**, *8*, 1923–1937.
(48) Persson, I.; D'Angelo, P.; De Panfilis, S.; Sandström, M.; Eriksson, L. *Chem. Eur. J.* **2008**, *14*, 3056–3066.

(49) Bard, A. J.; Faulkner, L. R. *Electrochemical Methods: Fundamentals and Applications*, 2nd ed.; John Wiley & Sons, 2001.
(50) Ahrenholtz, S. R.; Epley, C. C.; Morris, A. J. *J. Am. Chem. Soc.* **2014**, *136*, 2464–2472.
(51) Anderson, H. L.; Anderson, S.; Sanders, J. K. M. *J. Chem. Soc., Perkin Trans. 1* **1995**, 2231–2245.
(52) Constable, E. C.; Zhang, G.; Housecroft, C. E.; Zampese, J. A. *CrystEngComm* **2011**, *13*, 6864–6870.
(53) Schmittel, M.; He, B.; Mal, P. *Org. Lett.* **2008**, *10*, 2513–2516.
(54) Chui, S.; Lo, S.; Charmant, J.; Orpen, A.; Williams, I. *Science* **1999**, *283*, 1148–1150.
(55) Furukawa, H.; Go, Y. B.; Ko, N.; Park, Y. K.; Uribe-Romo, F. J.; Kim, J.; O'Keeffe, M.; Yaghi, O. M. *Inorg. Chem.* **2011**, *50*, 9147–9152.
(56) Friebel, D.; Bajdich, M.; Yeo, B. S.; Louie, M. W.; Miller, D. J.; Casalongue, H. S.; Mbuga, F.; Weng, T.-C.; Nordlund, D.; Sokaras, D.; Alonso-Mori, R.; Bell, A. T.; Nilsson, A. *Phys. Chem. Chem. Phys.* **2013**, *15*, 17460–17467.
(57) Zhou, M.; Cai, L.; Bajdich, M.; García-Melchor, M.; Li, H.; He, J.; Wilcox, J.; Wu, W.; Vojvodic, A.; Zheng, X. *ACS Catal.* **2015**, *5*, 4485–4491.
(58) Zhang, B.; Zheng, X.; Voznyy, O.; Comin, R.; Bajdich, M.; Garcia-Melchor, M.; Han, L.; Xu, J.; Liu, M.; Zheng, L.; Garcia de Arquer, F. P.; Dinh, C. T.; Fan, F.; Yuan, M.; Yassitepe, E.; Chen, N.; Regier, T.; Liu, P.; Li, Y.; De Luna, P.; Janmohamed, A.; Xin, H. L.; Yang, H.; Vojvodic, A.; Sargent, E. H. *Science* **2016**, *352*, 333–337.
(59) Perdew, J. P.; Burke, K.; Ernzerhof, M. *Phys. Rev. Lett.* **1996**, *77*, 3865–3868.
(60) Dudarev, S. L.; Botton, G. A.; Savrasov, S. Y.; Humphreys, C. J.; Sutton, A. P. *Phys. Rev. B* **1998**, *57*, 1505–1509.
(61) Wang, L.; Maxisch, T.; Ceder, G. *Phys. Rev. B* **2006**, *73*, 195107.
(62) Jain, A.; Ong, S. P.; Hautier, G.; Chen, W.; Richards, W. D.; Dacek, S.; Cholia, S.; Gunter, D.; Skinner, D.; Ceder, G.; Persson, K. A. *APL Mater.* **2013**, *1*, 011002.
(63) Chupas, P. J.; Qiu, X.; Hanson, J. C.; Lee, P. L.; Grey, C. P.; Billinge, S. J. L. *J. Appl. Crystallogr.* **2003**, *36*, 1342–1347.
(64) Hammersley, A. P.; Svensson, S. O.; Hanfland, M.; Fitch, A. N.; Hausermann, D. *High Pressure Res.* **2006**, *14*, 235–248.
(65) Juhás, P.; Davis, T.; Farrow, C. L.; Billinge, S. J. L. *J. Appl. Crystallogr.* **2013**, *46*, 560–566.
(66) Yang, X.; Juhas, P.; Farrow, C. L.; Billinge, S. J. L. *J. Appl. Crystallogr.* **2014**, 1402.3163.